

2008

Computed tomography imaging to quantify iodine distribution in iododeoxyuridine-labeled DNA

Christopher Erik Welch

Louisiana State University and Agricultural and Mechanical College

Follow this and additional works at: https://digitalcommons.lsu.edu/gradschool_theses



Part of the [Physical Sciences and Mathematics Commons](#)

Recommended Citation

Welch, Christopher Erik, "Computed tomography imaging to quantify iodine distribution in iododeoxyuridine-labeled DNA" (2008). *LSU Master's Theses*. 1948.

https://digitalcommons.lsu.edu/gradschool_theses/1948

This Thesis is brought to you for free and open access by the Graduate School at LSU Digital Commons. It has been accepted for inclusion in LSU Master's Theses by an authorized graduate school editor of LSU Digital Commons. For more information, please contact gradetd@lsu.edu.

**COMPUTED TOMOGRAPHY IMAGING TO QUANTIFY IODINE
DISTRIBUTION IN IODODEOXYURIDINE-LABELED DNA**

A Thesis

Submitted to the Graduate Faculty of the
Louisiana State University and
Agricultural and Mechanical College
in partial fulfillment of the
requirements for the Degree of
Master of Science

in

The Department of Physics & Astronomy

by
Christopher Erik Welch
B.S. Louisiana State University, 2005
December, 2008

Acknowledgments

I dedicate this work to my uncle Scott whose thirst for knowledge and positive attitude despite all odds was inspirational and I dedicate this to my beautiful wife Christina who somehow put up with me through all of this while she obtained her own degree from the LSU School of law. How she kept from doing me great physical harm I'll never know.

I offer my heartfelt thanks to the cast and crew of LSU's Department of Physics and Astronomy, Mary Bird Perkins Cancer Center, and LSU's Center for Advanced Microstructures and Devices. I, quite literally, couldn't have done it without you.

Thank you all.

Table of Contents

Acknowledgments.....	ii
List of Tables	v
List of Figures.....	vi
Abstract.....	xi
Chapter 1. Introduction.....	1
1.1 X-ray Activated Auger Electron Radiotherapy	1
1.2 Monochromatic X-ray Sources.....	7
1.3 Computed Tomography.....	10
1.4 Previous Synchrotron Based Iodine Imaging Studies.....	19
1.5 Hypothesis and Specific Aims.....	22
Chapter 2. Aim 1, Polychromatic CT Sensitivity Measurements.....	24
2.1 Goals.....	24
2.2 Analytical Approach.....	24
2.3 Materials and Methods.....	24
2.3.1 Microtomography System	24
2.3.2 Image Acquisition	26
2.3.3 Phantom Construction	30
2.3.4 Image Reconstruction.....	32
2.3.5 Concentration Measurements.....	32
2.3.6 Resolution Measurements	35
2.4 Results.....	38
2.4.1 Concentration Measurements.....	38
2.4.2 Resolution Measurements	40
2.5 Discussion.....	40
2.5.1 Concentration Measurements.....	40
2.5.2 Resolution Measurements	41
Chapter 3. Aim 2, Monochromatic CT Sensitivity Measurements.....	43
3.1 Goals.....	43
3.2 Analytical Approach.....	43
3.3 Materials and Methods.....	43
3.3.1 CAMD Synchrotron Facility	43
3.3.2 Tomography Apparatus.....	45
3.3.3 Image Acquisition	48
3.3.4 Phantom Construction	49
3.3.5 Image Reconstruction.....	52
3.3.6 X-ray Scatter Measurement.....	54
3.3.7 Concentration Measurements.....	55
3.3.8 K-edge Subtraction Implementation.....	56
3.3.9 Resolution Measurements	56

3.4 Results.....	57
3.4.1 Beam Energy Measurements.....	57
3.4.2 Reconstruction Algorithm Comparison.....	57
3.4.3 X-ray Scatter Measurement.....	59
3.4.4 Concentration Measurements.....	61
3.4.5 K-edge Subtraction.....	65
3.4.6 Resolution Measurements.....	67
3.5 Discussion.....	67
3.5.1 Energy Measurements.....	67
3.5.2 Reconstruction Algorithm Comparison.....	68
3.5.3 X-ray Scatter Measurement.....	69
3.5.4 Concentration Measurements.....	69
3.5.5 K-edge Subtraction.....	70
3.5.6 Resolution Measurements.....	70
Chapter 4. Aim 3, In Vitro Imaging Study.....	71
4.1 Goal.....	71
4.2 Analytical Approach.....	71
4.3 Materials and Methods.....	71
4.3.1 Chinese Hamster Ovary Cells.....	71
4.3.2 Cell Culturing and Preparation.....	71
4.3.3 Phantom.....	74
4.3.4 Surface Dose Estimate.....	74
4.4 Results.....	76
4.4.1 Cell Density Assay.....	76
4.4.2 IUdR Uptake Assay.....	77
4.4.3 IUdR Replacement Measurements.....	77
4.5 Discussion.....	78
4.5.1 Cell Density Assay.....	78
4.5.2 IUdR Uptake Assay.....	79
4.5.3 IUdR Replacement Measurements.....	79
Chapter 5. Conclusions and Recommendations.....	80
5.1 Summary of Results.....	80
5.2 Conclusions.....	81
5.3 Recommendations for Future Studies.....	82
References.....	83
Appendix	
A. K-edge Subtraction.....	87
A.1 K-edge Subtraction Theory.....	87
B. CAMD Tomography Beamline Energy Measurement.....	89
B.1 X-ray Powder Diffraction Theory.....	89
B.2 X-ray Powder Diffraction Energy Measurements.....	95
Vita.....	97

List of Tables

Table 1: Comparison of in vivo studies of continuous intravenous infusions (Cook et al 1992) and perorally administered (Kinsella et al 1994) IUdR incorporation into DNA. ^{7,8}	7
Table 2: Skyscan-1074 acquisition parameters.....	30
Table 3: Results from the Skyscan-1074 measurements at 40 kVp.....	40
Table 4: Results from CAMD measurements at a monochromator setting of 32.5. Empty spaces indicate missing or corrupted data.	64
Table 5: Results from CAMD measurements at a monochromator setting of 33.5. Empty spaces indicate missing or corrupted data.	64
Table 6: Results from the CAMD KES.	66
Table 7: Results from hemocytometry measurements of cell density. Each cell per grid square corresponds to 10^6 cells per ml in suspension. Three squares were added to obtain the cell count.	77
Table 8: For Si640c, the three brightest Debye-Scherrer cones correspond to the first three lattice spacings d . The lattice spacing is determined by dividing the lattice parameter a by the RSS of the Miller indices; H, K, and L. ³⁷	91
Table 9: Monochromator setting and results from the X-ray powder diffraction measurements with the measurement error.....	96

List of Figures

Figure 1: Molecular structure of thymidine and iododeoxyuridine.....	2
Figure 2: Auger electron production following a photoelectric event.....	3
Figure 3: V-79 Chinese hamster cell survival curves plotted as a function of dose. (Δ) IUdR-labeled cells irradiated at 33.4 keV, (◇) IUdR-labeled cells irradiated at 32.9 keV, and (○) control cells irradiated at 32.9 keV. ⁵	5
Figure 4: Dose enhancement as a function of photon energy for x-ray activated Auger electron radiotherapy. Each curve represents a different percentage of thymidine molecules in DNA replaced by IUdR. ⁶	6
Figure 5: (Top curve) X-ray flux from National Synchrotron Light Source at 250 mA ring current compared to (bottom curve) the flux from a 100 kW x-ray tube at 110 kVp measured 1 meter from the source. ¹²	8
Figure 6: Inverse Compton scattering process. ⁹ High energy electron beam collides with focused intense infrared beam to produce x-rays.	9
Figure 7: Illustration of the role of x-rays in image formation. Uncollided X-rays reaching the detector plane carry information about the subject. X-rays which interact with the subject are removed entirely from the resulting image or they contribute to noise or blurring.....	12
Figure 8: A simulated object (left) and its sinogram (right). Sinogram consists of projections acquired over 180° with 1° step size.....	13
Figure 9: Typical filter functions used in CT.....	14
Figure 10: Beam hardening effect illustrated by comparing filtered x-ray spectrum to the same beam after traversing 6 cm of tissue (Dilmanian et al. 1992). ¹²	15
Figure 11: Mass energy absorption coefficients [μ_{en}/ρ] as a function of photon energy (MeV). ¹⁷	16
Figure 12: Example of K-edge subtraction (KES) results in thorax using xenon gas (K-edge of 34.56 keV) from Suhonen et al (2008). ²³	18
Figure 13: Example of temporal subtraction results from Suhonen et al (2008). ²³	19
Figure 14: Results from Suhonen et al (2008) comparing KES and TS techniques. ²³ The left two images show the concentration quantification comparison of KES and TS using iodine (top) and xenon (bottom). The above right image shows concentration histograms in part of a rabbit's lung for KES and TS using iodine and xenon.....	22

Figure 15: Skyscan-1074 Portable X-ray Microtomograph system (right) connected with a desktop computer for image acquisition.	25
Figure 16: Skyscan-1074 imaging compartment. Samples are placed on the stage (pedestal in image center) which rotates. The x-ray tube (not shown) produces a “cone” of x-rays which travel from right to left. The scintillator is located behind the circular mylar-covered window at left.	25
Figure 17: Schematic of X-ray source, object rotation center, and detector array center (top view). The dashed line shows the expected collinear arrangement of the source, object center, and detector center used for reconstruction. The dashed-dotted line shows the results of an alignment correction.	26
Figure 18: Skyscan-1074 open field. The pixel values representing photon counts are displayed in grayscale. Tube settings were 40 kVp, 1000 μ A, 420 ms exposure time, 100% gain. This open field image is an average of five acquisitions.	28
Figure 19: Reconstruction of the central slice of a blank acrylic phantom acquired on Skyscan-1074. The left image was reconstructed using only the 0° to 180° projections. The right image was reconstructed using the 0° to 360° projections. The 0° to 180° projections for both images are the same.	29
Figure 20: Skyscan-1074 PMMA phantom. Each of the 5 sample holes were 1.5 cm deep.	31
Figure 21: Reconstructed image of Skyscan phantom with iodine solutions from NRecon® software. The central hole contained air while the remaining 4 holes contained a water solution having 0.0, 2.5, 5.0, 25.0 mg cm ⁻³ of iodine (CCW from the top left). The image was acquired with the acquisition parameters listed in Table 2.	31
Figure 22: Flow chart showing the process for obtaining the modulation transfer function from a raw image of the MTF test phantom.	36
Figure 23: Simulated data to test proper function of the MTF calculation routine. On the left is a circle 337 pixels in diameter to approximate the MTF test phantom. The image on the right is the left image convolved with a 2D Gaussian filter with σ of 9 pixels.	37
Figure 24: PSF obtained from the simulated MTF image is displayed in black. Displayed in red is the one dimensional representation of the Gaussian filter ($\sigma = 9$) that generated the simulated image. The calculated PSF agreed closely with the true Gaussian PSF.	37
Figure 25: Skyscan results plotted in CT number vs. iodine concentration up to 1 mg ml ⁻¹ for CT acquisition at 40 kVp. The solid black line represents a linear fit constrained to go through the origin ($\chi^2 = 55.2$). The solid red and dashed black	

lines represent the 95% confidence and prediction bands. Error bars represent the standard deviation.	38
Figure 26: Skyscan results plotted in CT number vs. iodine concentration up to 10 mg ml ⁻¹ for CT acquisition at 40 kVp. A linear fit of the data with $\chi^2 = 51.1$ (black line), and 95% prediction interval (dashed lines) are shown. The individual data points have been plotted to illustrate the spread of the measurements at each concentration.....	39
Figure 27: The composite edge profile is shown in the top left which is smoothed to obtain the ERF (top right). The analytical derivative of the ERF is used smoothed to produce the PSF (bottom left). The Fourier transform of the PSF is the MTF (bottom right) measured for the Skyscan-1074 system. The spatial frequency of the MTF measured at 10% of the maximum was found to be 5.5 lp mm ⁻¹	41
Figure 28: Plot of photon absorption measurements as a function of energy showing the K-edges of several target materials used to calibrate the monochromator on the CAMD tomography beamline (http://tomo.camd.lsu.edu).	45
Figure 29: Top and side view of the CAMD tomography apparatus within the experimental hutch. (Drawing not to scale.).....	46
Figure 30: Images of the CAMD x-ray beam acquired with radiochromic film. (Left) Image of the uncollimated beam, showing the primary beam (red arrow) surrounded by secondary radiation coming from the monochromator and other surfaces. (Right) Image of the collimated and filtered beam used for CT imaging.	47
Figure 31: Top and side views of the polypropylene (left) and HDPE (right) tubes arranged in the PMMA base for imaging.	51
Figure 32: Cross-sectional slice of the HDPE tubes with iodine concentrations surrounding a PP tube.	51
Figure 33: Diagram (top view) illustrating the X-ray scatter contribution measurement. The dashed lines represent X-rays. At the detector, there should be a photon deficiency due to the lead block. Any scattered photons reaching this region would contribute to an increased signal.....	55
Figure 34: Illustration of the CAMD MTF test phantom used to measure the resolution of the CAMD tomography system.	57
Figure 35: An unprocessed projection image of 10 HDPE tubes arranged in a rough circle around a PP tube. The white spots and wavy background structure are attributable to impurities in the scintillator and beam inhomogeneities.	58
Figure 36: Displayed is the projection image data from Figure 35 after being corrected for the white and dark field effects. The projection image has been converted into total attenuation per pixel.....	58

Figure 37: Results from FBP comparison between MATLAB’s reconstruction using a Shepp-Logan filter (Δ) and the in house routine written in IDL using Shepp-Logan (+) and Ramp-Hann filters (\diamond). 59

Figure 38: Corrected projection image of scatter phantom with 1 mm wide by 2 mm thick lead beam block. 60

Figure 39: Average profile of scatter phantom and lead beam block. The scatter to primary ratio was calculated to be 0.0276. 60

Figure 40: CAMD results plotted in CT number vs. iodine concentration up to 1 mg ml⁻¹ for CT acquisition at 32.5 keV. The linear fit (solid black) is constrained to go through the origin ($\chi_v^2 = 0.75$). The solid red and dashed black lines represent the 95% confidence and prediction bands. Error bars represent the standard deviation. 61

Figure 41: CAMD results plotted in CT number vs. iodine concentration up to 10 mg ml⁻¹ for CT acquisition at 32.5 keV. A linear fit of the data with $\chi_v^2 = 1.20$ (black line), and 95% prediction interval (dashed lines) are shown. The individual data points have been plotted to illustrate the spread in the measurements. 62

Figure 42: CAMD results plotted in CT number vs. iodine concentration up to 1 mg ml⁻¹ for CT acquisition at 33.5 keV. The linear fit (solid black) is constrained to go through the origin ($\chi_v^2 = 1.97$). The solid red and dashed black lines represent the 95% confidence and prediction bands. Error bars represent the standard deviation. 62

Figure 43: CAMD results plotted in CT number vs. iodine concentration up to 10 mg ml⁻¹ for CT acquisition at 33.5 keV. A linear fit of the data with $\chi_v^2 = 3.37$ (black line), and 95% prediction interval (dashed lines) are shown. The individual data points have been plotted to illustrate the spread in the measurements. 63

Figure 44: CAMD results plotted in CT number vs. iodine concentration up to 1 mg ml⁻¹ for KES. The linear fit (solid black) is constrained to go through the origin ($\chi_v^2 = 0.92$). The solid red and dashed black lines represent the 95% confidence and prediction bands. Error bars represent the standard deviation. 65

Figure 45: CAMD results plotted in CT number vs. iodine concentration up to 10 mg ml⁻¹ for KES. A linear fit of the data with $\chi_v^2 = 3.07$ (black line), and 95% prediction interval (dashed lines) are shown. The individual data points have been plotted to illustrate the spread in the measurements. 66

Figure 46: CT image of the CAMD MTF test phantom. A Ram-Lak filter with a cut-off at the Nyquist frequency was used during reconstruction..... 67

Figure 47: The composite edge profile is shown in the top left which is smoothed to obtain the ERF (top right). The analytical derivative of the ERF is used smoothed to produce the PSF (bottom left). The Fourier transform of the PSF is the MTF (bottom right) for the CAMD tomography system. The spatial frequency of the MTF measured at 10% of the maximum was found to be 56 lp mm⁻¹ 68

Figure 48: Cutaway view of the PMMA base used to mechanically support the microcentrifuge tube and the HDPE tube containing water. The red dashed line indicates the approximate beam path through the cell mass in the bottom of the microcentrifuge tube. 75

Figure 49: A typical CT image acquired at 33.5 keV of the PMMA base, the CHO cell tube containing IUDR-labeled cells and the HDPE tube filled with distilled/deionized water. 75

Figure 50: Example of a KES image of CHO cells assuming the mass attenuation coefficients of water as the buffering solution. 78

Figure 51: X-ray scatter diagram from Bragg lattice planes (adapted from Thornton et al 2002).³⁶ The X-ray scatter angle is twice the incident angle (2θ). D is the lattice parameter and d is the interlattice spacing. The difference in path length is $2d \sin(\theta)$... 90

Figure 52: A top view example of three possible Bragg planes in a NaCl crystal and their corresponding interlattice spacings (adapted from Thornton et al 2002).³⁶ 90

Figure 53: Diagram of the Si640c powder sample. The sample holder was constructed from PMMA. The Si640c powder (A) was contained by Scotch® tape on both sides. The empty hole (B) was used to obtain correct vertical alignment of the sample holder. 91

Figure 54: The side view (left) and top view (right) of the X-ray powder diffraction experimental apparatus are shown. 93

Figure 55: Diagram illustrating the effects of X-ray powder diffraction. The resulting Debye-Scherrer patterns are shown at several film planes. 94

Figure 56: On the left is an example of a film shot from X-ray powder diffraction measurements. The concentric diffraction rings can be seen around the collimated beam. On the right is the same film after being passed through a band pass filter. The collimated beam has been obscured for display. 95

Figure 57: Comparison of CAMD Tomography beamline monochromator settings versus X-ray powder diffraction measurements. 96

Abstract

Purpose: Treatment planning for x-ray activated Auger electron radiotherapy requires knowledge of the spatial distribution of Auger electron-producing target atoms in DNA; iodine is a candidate atom. Because planning uses computed tomography (CT) data to show anatomy, obtaining the target atoms' distribution with CT methods is an attractive goal. This study evaluates the ability of two available CT systems to measure the target atoms' spatial distribution.

Method and Materials: A polychromatic desktop CT scanner and a synchrotron monochromatic CT system acquired images of iodine concentrations in water, ranging from 0.03-10 mg/ml. The polychromatic scanner was operated at 40 kVp while the synchrotron system was operated at 32.5 keV and 33.5 keV. Calibration curves of Hounsfield units (HU) vs. iodine concentration were obtained from each CT set, with minimum detectable iodine concentration defined as the smallest concentration distinguishable from water with contrast-to-noise ratio of 3. K-edge subtraction (KES) analysis was applied to the synchrotron CT data as another quantification method.

To determine if iodine uptake could be quantified in vitro, Chinese hamster ovary (CHO) cells grown with iododeoxyuridine (IUdR) were imaged with the synchrotron. Iodine uptake was measured with the HU calibration curve and KES.

Results: The expected iodine concentration for breast cancer in vivo is estimated to be 0.06 mg/ml for IUdR. The minimum detectable iodine concentration was 0.1 mg/ml for the 40 kVp polychromatic CT data and 0.1 mg/ml for the synchrotron CT at 33.5 keV; minimum detectability using KES was 0.25 mg/ml. Thus, these current systems could not visualize the estimated target concentration. The measured iodine concentration in the

cells was 0.21 ± 0.04 mg/ml using the HU calibration curve and 0.20 ± 0.01 mg/ml using KES, compared to an expected concentration in DNA of 0.001 mg/ml.

Conclusions: Using the current acquisition methods, these CT systems proved unable to measure the expected concentration. Improvements may be possible by modifying the acquisition parameters. From the cell image results, CT imaging for treatment planning will quantify both DNA-incorporated iodine and intracellular unincorporated iodine; if the two amounts can be shown to have a stable proportion; CT quantification methods may be satisfactory for treatment planning.

Chapter 1. Introduction

A primary challenge of modern radiation therapy techniques is to maximize the radiation dose delivered to cancer while minimizing the dose delivered to normal healthy tissue. Optimally, the radiation dose would be delivered only to the cancer or, more specifically, to the cancer's DNA. Increasing the radiation induced damage done to the cancer's DNA results in a greater cell killing effect. Many techniques have been developed which attempt to conform the dose distribution to the cancer but often require a low dose to normal tissue. Normal tissue tolerances necessitate a high degree of dose conformality. X-ray activated Auger electron radiotherapy is a new treatment modality which attempts to reduce the undesirable low dose to normal healthy tissue by creating a dose enhancement in the cancer's DNA.

Louisiana State University is currently working to develop a treatment planning system for x-ray activated Auger electron radiotherapy. This treatment modality targets tracer compounds embedded in DNA to deliver dose. To effectively plan treatment, knowledge of the tracer distribution is required. Computed tomography is used clinically in conventional external beam treatment planning. The purpose of this study was to evaluate computed tomography's ability to quantify the tracer distribution. The following sections provide background material, culminating in the hypothesis and specific aims of this work. Subsequent chapters present the methods, results and conclusions of this study, arranged by specific aim.

1.1 X-ray Activated Auger Electron Radiotherapy

The principle advantage of x-ray activated Auger electron radiotherapy in the treatment of cancer is its potential to deliver a lower dose to healthy tissue while still

achieving the same cell killing effect in cancerous tissue containing the high-Z radiosensitizer. The desired results include decreasing the harmful side effects and reducing the risk of secondary cancers as a result of radiation exposure.

This technique produces the dose enhancement by irradiating a radiosensitizer that has been introduced into the target cells. The radiosensitizer produces many high-LET Auger electrons whose net result is a localized radiation dose to the target cells. An ideal radiosensitizer will contain a high-Z atom with a large Auger electron yield and will be incorporated into the DNA of the target cells.

Hall et al¹ described halogenated pyrimidines as sensitizers, such as 5-iododeoxyuridine (IUdR) and 5-bromodeoxyuridine; the amount of sensitizing effect on cells is determined by the amount present. These halogenated pyrimidines are chemically similar (Figure 1) to the DNA precursor thymidine, one of the four principle bases of DNA, having an iodine or bromine atom substituted in place of the methyl group CH₃. Incorporation into DNA can occur because the van der Waals radius of these atoms are similar to that of CH₃. These sensitizers become effective only if they are introduced in adequate quantities to actively cycling cells for several generations so as to be incorporated into the DNA.¹

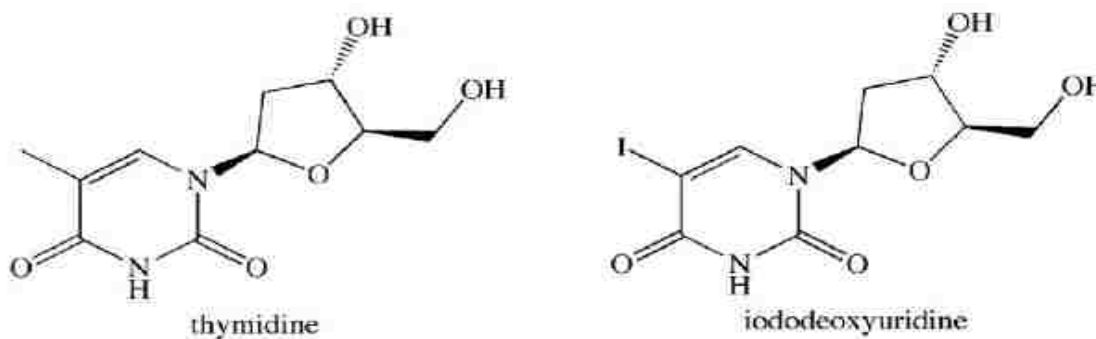


Figure 1: Molecular structure of thymidine and iododeoxyuridine.

Auger electrons are produced as a result of an atom shedding excess energy. They occur when an excited atom rearranges its electronic structure, typically following internal conversion, electron capture, or photoelectric interaction. Internal conversion occurs when a bound electron of a gamma-ray emitting radionuclide absorbs the excitation energy of its nucleus and is ejected. In electron capture, occasionally a neutron deficient atom cannot stabilize by positron emission and one of the extranuclear electrons interacts with an intranuclear proton to become a neutron leaving an electron vacancy in an inner shell orbit. The third mechanism which produces Auger electrons is a photoelectric interaction when a photon ionizes a tightly bound inner shell electron. In all three cases, a complex series of electron shell transitions occurs leaving the atom with excess energy. The atom can rid itself of this energy by emitting characteristic x-rays or by the ejection of secondary electrons. Electrons liberated in this way are Auger electrons shown in Figure 2.

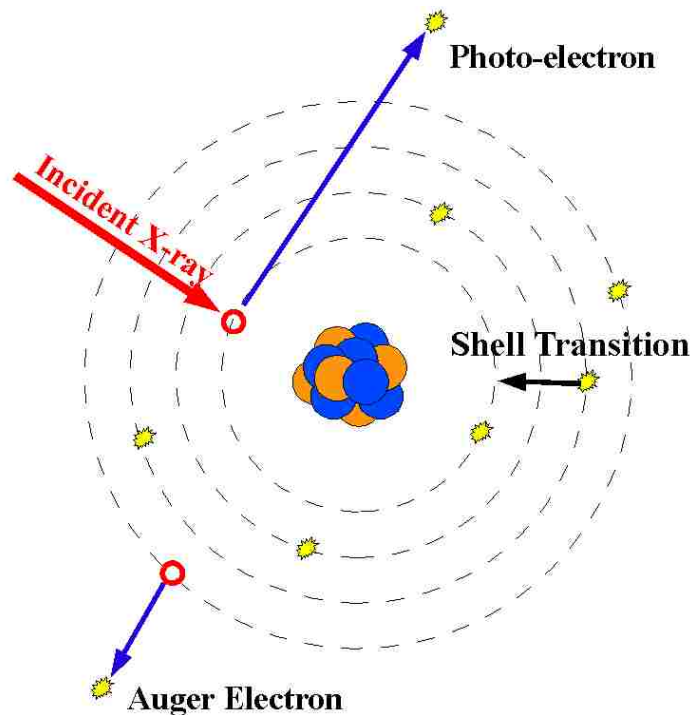


Figure 2: Auger electron production following a photoelectric event.

One can produce Auger electrons at will by irradiating target atoms with x-rays of the appropriate energy to cause photoelectric events. The probability to cause a photoelectric event at low energies can be expressed as being roughly proportional to the Z^3 of the material. Atoms such as iodine and platinum make good Auger emitters because each has a relatively high K-shell binding energy (33.17 keV and 78.4 keV respectively), and produces a significant number of Auger electrons.

Auger electrons are typically low energy. They range in energy from a few eV to ~100 keV with a range in water from a nanometer to several hundred micrometers respectively.² For the same distance traveled, low energy electrons (i.e. Auger electrons) lose more energy than high energy electrons, by as much as 100 times or more.³ This means that a low energy electron will deposit nearly all its energy over a very short distance. Due to their short range and the quantity of ionizations produced, Auger electrons originating in or near the DNA of a cell have the potential to cause fatal double-strand breaks in the DNA. Thus incorporating a high Z target element into the DNA of cancerous cells and then irradiating them with x-rays will produce Auger electrons directly in the DNA. This is an alternative to the strategy of incorporating Auger-emitting radionuclides.⁴

IUdR has an inherent radiation sensitizing effect. Auger electrons produced by irradiation provide a dose enhancing effect above the radiation sensitizing effect found with IUdR. A study by Laster et al has shown the dose enhancement with IUdR (Figure 3).⁵ Chinese hamster V79 cells containing IUdR-labeled DNA were irradiated at 32.9 keV using monochromatic x-rays, below the iodine K-edge of 33.17 keV (diamonds), and were compared to cells without IUdR irradiated under the same conditions (circles) to

show the radiation sensitization effects. Cells with IUdR-labeled DNA were also irradiated at 33.4 keV (triangles). The iodinated cells irradiated above the iodine K-edge were found to have a greater degree of cell death than iodinated cells irradiated below the K-edge. The ratio of the dose required to achieve 10% survival of cells labeled with IUdR irradiated above the K-edge (D_1) to cells labeled with IUdR irradiated below the K-edge (D_2) is the Auger dose enhancement.

Cells showing a 15-18% thymidine replacement by IUdR were found to have a dose enhancement ratio of 1.4 at 33.4 keV above the sensitizing effect of IUdR alone. That is, to achieve the same cell killing effect as cells with IUdR irradiated below the iodine K-edge, 29% less dose was required when cells containing IUdR were irradiated above the iodine K-edge.

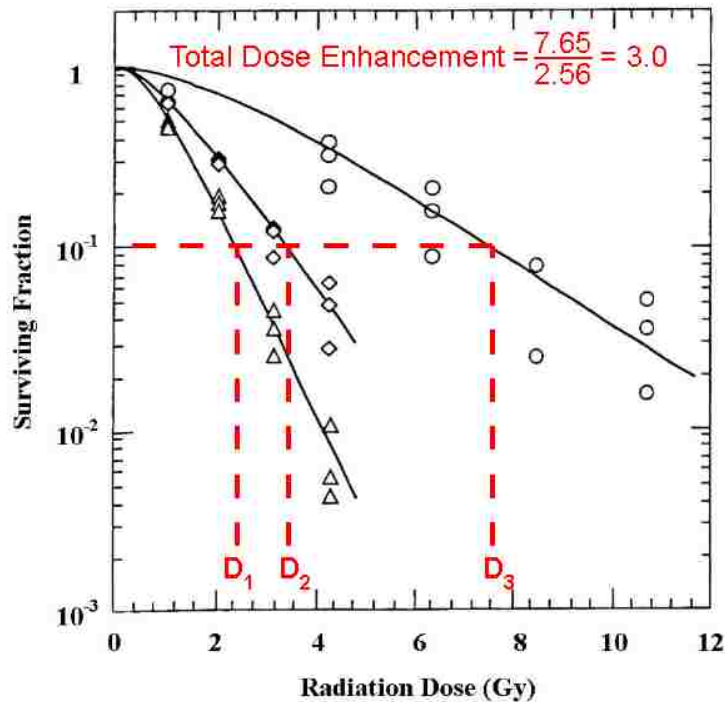


Figure 3: V-79 Chinese hamster cell survival curves plotted as a function of dose. (Δ) IUdR-labeled cells irradiated at 33.4 keV, (\diamond) IUdR-labeled cells irradiated at 32.9 keV, and (\circ) control cells irradiated at 32.9 keV.⁵

Laster et al. showed that Auger electron production by irradiation with monochromatic x-rays produces a dose enhancement.⁵ Others have shown that filtered kilovoltage x-rays can also be used. Karnas et al irradiated IUdR laden Chinese hamster ovary (CHO) cells with monochromatic x-rays and found that the dose enhancement reached a maximum at about 50 keV shown in Figure 4. The calculated optimum energy for x-ray activated Auger electron radiotherapy was 50 keV delivered via a monochromatic beam.⁶

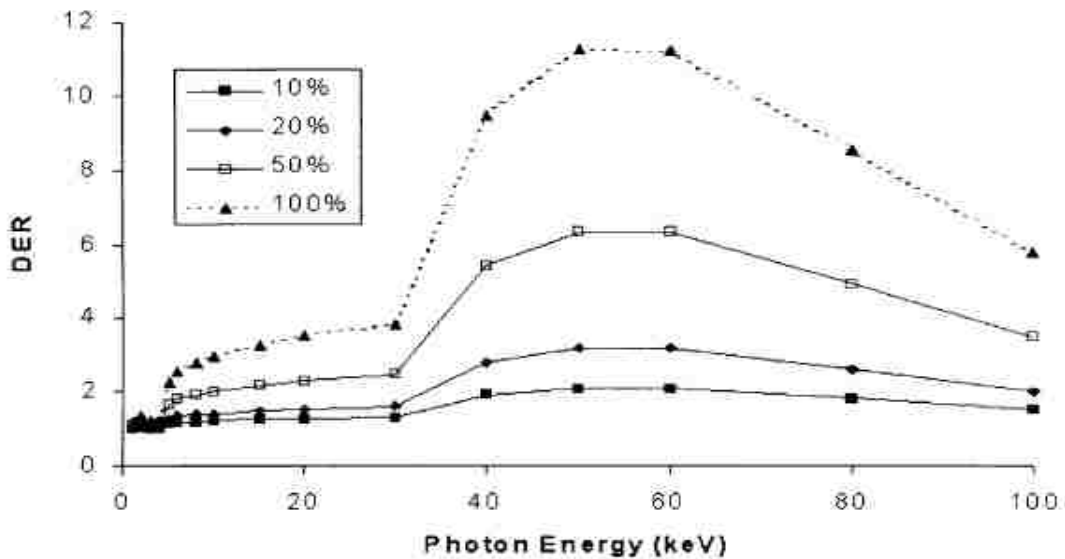


Figure 4: Dose enhancement as a function of photon energy for x-ray activated Auger electron radiotherapy. Each curve represents a different percentage of thymidine molecules in DNA replaced by IUdR.⁶

Iodine has a relatively low K-shell binding energy and treatment involving IUdR would likely only be useful in shallow/superficial tumors. This is because an x-ray beam would be highly attenuated in trying to reach deeper seated lesions resulting in an unnecessarily high surface dose to the patient. Low thymidine replacement by IUdR is also a concern. In vivo studies have shown that continuous intravenous infusion of IUdR

provides superior IUdR incorporation into DNA than perorally administered IUdR.^{7,8}

Table 1 shows the results of this comparison. Intravenous infusion clearly shows a greater degree of IUdR incorporation in the case of faster growing malignancies such as head and neck cancers with an IUdR replacement of up to 26.3%. Slower growing malignancies such as gliomas showed fewer than 25% of cancer cells had up to 4% IUdR replacement.

Table 1: Comparison of in vivo studies of continuous intravenous infusions (Cook et al 1992) and perorally administered (Kinsella et al 1994) IUdR incorporation into DNA.^{7,8}

	Cancer Type	% IUdR Replacement
Continuous	Gliomas (human)	< 25% of cells had 0-4%
Intravenous Infusion	Head and Neck (human)	63-85% of cells had 2.9-26.3%
	Sarcomas (human)	57-79% of cells had 7.5-14.2%
Perorally Administered	Subcutaneous tumors (mice)	3.65%
	Liver tumors (mice)	4.79%

Inherent toxicity is a limiting factor in the clinical use of IUdR. Systemic effects to the marrow (thrombocytopenia) and GI tract (stomatitis and diarrhea) limit IUdR dosage. The mechanism of IUdR's cytotoxicity is still poorly understood. Potentially, it inhibits DNA base excision repair following chemical or ionizing radiation damage.⁸ Additionally, it has poor specificity for tumor cells. That is, IUdR will be incorporated into the DNA of any cells undergoing DNA synthesis. For this reason, IUdR would only be useful for treating fast growing tumors surrounded by slow growing normal healthy tissue.

1.2 Monochromatic X-ray Sources

Polychromatic x-rays have several drawbacks not present with monochromatic x-rays as a result of their continuous spectrum. The low energy portion of polychromatic x-ray beams delivers high radiation doses to the patient. There are relatively few high

energy photons produced which are needed to penetrate tissues or reach deep seated lesions which makes treatment with polychromatic x-rays undesirable.⁹

X-ray activated Auger electron radiotherapy should be most pronounced with a monochromatic X-ray source, but there is a current lack of practical monochromatic x-ray sources in the clinical setting. Alternatively, this has prompted the development of quasi-monochromatic x-ray sources, such as a conventional narrow energy band x-ray tube focused on a monochromator.¹⁰ A monochromator uses Bragg diffraction on mosaic crystals to effectively monochromatize a polychromatic spectrum. X-ray tubes are notoriously inefficient, with vastly more input power being converted to heat energy than into photons, resulting in very low photon fluence rates when coupled with a monochromator.¹¹ Likewise, typical metal-anode x-ray tubes, filtered to produce characteristic x-rays, are not tunable across a broad range and are also plagued with low fluence rates (bottom curve in Figure 5).

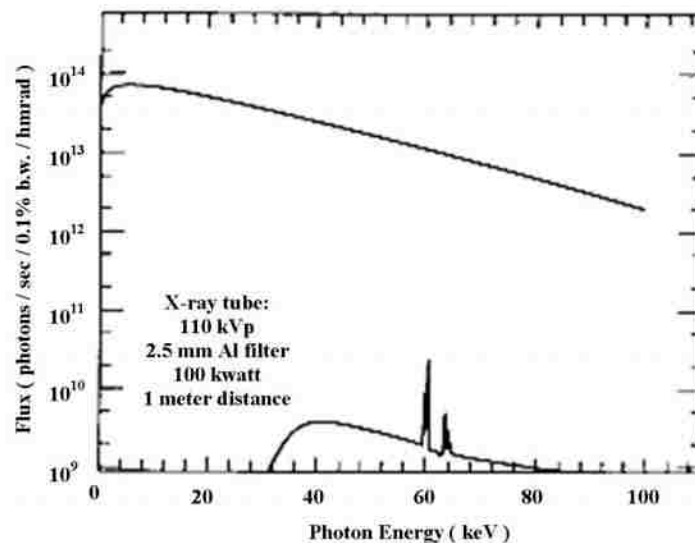


Figure 5: (Top curve) X-ray flux from National Synchrotron Light Source at 250 mA ring current compared to (bottom curve) the flux from a 100 kW x-ray tube at 110 kVp measured 1 meter from the source.¹²

One viable option for tunable monochromatic x-rays has been large synchrotron radiation (SR) facilities. The high fluence rates (top curve in Figure 5) of these machines are such that even when used with a monochromator, the intensity is acceptably high. Beam time at these facilities is both limited and expensive, so synchrotron based sources are impractical for widespread clinical use.¹¹

A new modality in monochromatic x-ray production has been developed by MXI systems, Inc. (<http://mxisystems.com>) based on the work of Carroll et al.^{9,11,13} MXI systems' instrument uses inverse Compton scattering to produce monochromatic x-rays. The process consists of a head-on collision of a high-energy electron beam with an intense beam of infrared light (Figure 6). The electrons scatter the infrared photons and impart some of their energy to the photons thereby shortening their wavelengths to those of x-rays. Conservation of energy dictates that the photons produced by this interaction are monochromatic. It is possible to manipulate the resulting x-ray energy by adjusting the initial energy of the electrons.¹⁴

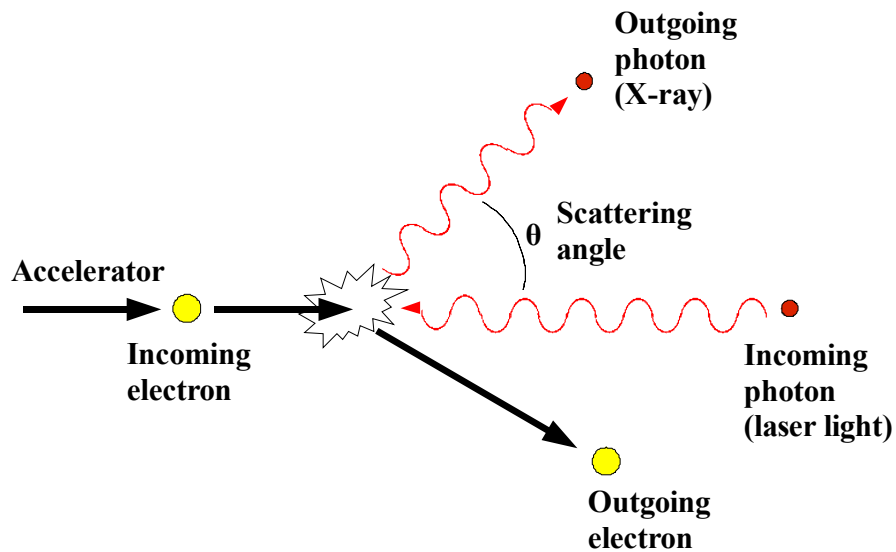


Figure 6: Inverse Compton scattering process.⁹ High energy electron beam collides with focused intense infrared beam to produce x-rays.

This technology could make feasible the clinical use of monochromatic x-rays for x-ray activated Auger electron radiotherapy. For this reason a research group at Louisiana State University (LSU) has begun to explore the feasibility of designing a radiotherapy treatment planning system. This includes dosimetric verification of the Auger emitters for radiotherapy and investigation of imaging methods for quantitative analysis of replacement of the high-Z target in DNA. This is possible because of LSU's Center for Advanced Microstructures and Devices (CAMD), a synchrotron facility.

1.3 Computed Tomography

Computed tomography (CT) is a valuable cross-disciplinary tool. It is of particular importance in radiation oncology for the purposes of diagnosis and treatment planning. This project is investigating CT image data to see if it can be used to assess the amount of IUDR replacement in DNA. The first CT machine was developed by Nobel Prize winners Godfrey Hounsfield and Allan Cormack in 1979. The basis for their work was the mathematical principles of Johann Radon in 1917.¹⁵

In radiation therapy treatment planning, accurate dosimetry can only be performed with appropriate information about the patient data; this includes surface contour and internal composition. Khan¹⁶ describes CT and magnetic resonance imaging (MRI) as the optimum methods. Occasionally, CT and MRI are used in conjunction during treatment planning. This is because MRI is superior to CT in soft tissue discrimination but is rather insensitive to the calcifications and bony structures that CT visualizes well. A drawback to using MRI is its long acquisition time which leads to motion artifacts. CT has superior geometric accuracy over that of any other imaging

modality and it returns the relative electron density map. For these reasons, CT is the preferred imaging modality in radiotherapy treatment planning.¹⁶

To produce CT images there are three primary components required; an x-ray source, a detector, and a computer to reconstruct and view the images. Conventional CT scanners use an x-ray tube which produces x-rays by boiling electrons off of a filament or cathode into a vacuum before being accelerated toward an anode by an electric field created by the potential difference between the positive-potential cathode and the negative-potential anode. When the electrons impinge on the anode, they undergo a deceleration which causes “braking” radiation or x-rays. The x-rays produced are comprised of a spectrum of energies with a maximum energy equal to the accelerating potential used by the tube (see Figure 5 or Figure 10). The formation of an x-ray image of a subject depends on x-rays being attenuated, absorbed, or scattered as they pass through the subject. The resulting transmission image at the detector plane provides information about the subject based on the intensity pattern of x-rays that reach the detector.

CT imaging requires 2D projection images, as in a standard radiograph (x-ray), acquired at different axial positions around a subject. Each point in the image records the number of x-rays reaching the detector plane at a particular point. This image records attenuation within the subject, which is related to the structure and composition of the subject. X-rays interacting within the subject are either absorbed or scattered away from their original path as shown in Figure 7. Those x-rays that are absorbed do not reach the detector plane and therefore do not contribute to the image. X-rays which scatter are either scattered away from the detector, in which case they do not contribute to the image, or they are scattered toward the detector and contribute to noise and blurring.

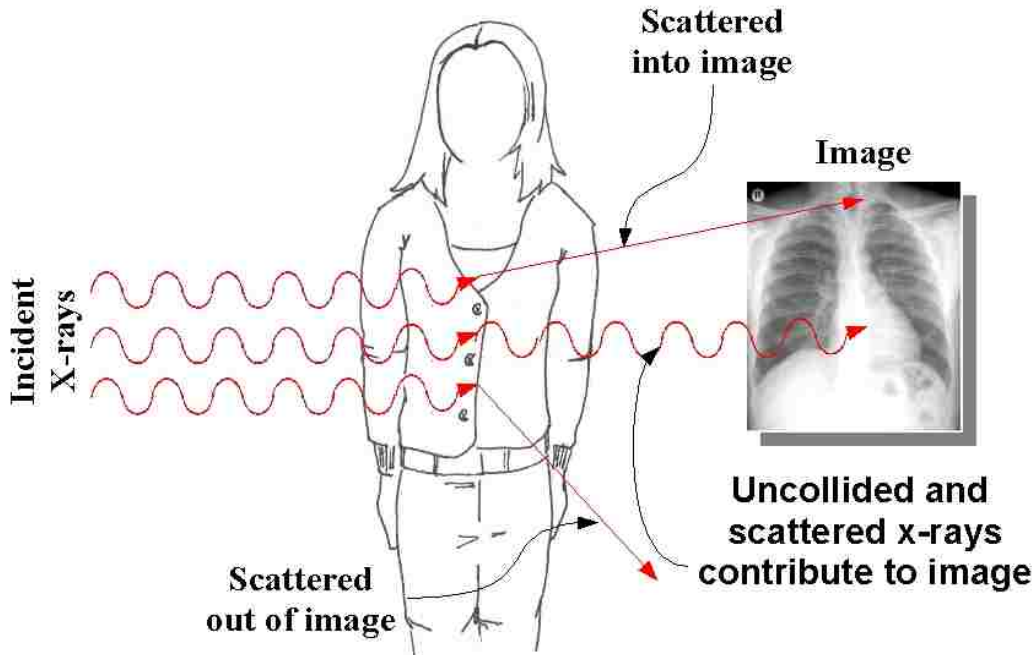


Figure 7: Illustration of the role of x-rays in image formation. Uncollided X-rays reaching the detector plane carry information about the subject. X-rays which interact with the subject are removed entirely from the resulting image or they contribute to noise or blurring.

The image is a measure of the number of X-ray photons reaching the detector. For a composite of i separate materials in a given X-ray path, the number of uncollided photons reaching a point on the detector can then be expressed as the following

$$N = N_0 e^{-\sum_i (\mu_i t_i)} \quad (1-1)$$

where N is the number of photons passing uncollided; N_0 is the initial number of photons; and μ_i is the linear attenuation coefficient of a material of thickness t_i .

$$\ln \left[\frac{N_0}{N} \right] = \sum_i (\mu_i t_i) \quad (1-2)$$

$$\mu_E t_{total} = \sum_i (\mu_i t_i) \quad (1-3)$$

The effective linear attenuation coefficient (μ_E) is the measured value and is defined as the integral of the attenuation coefficients from the X-ray source to the detector. A reconstructed CT image is proportional to the effective mass attenuation coefficient defined as the quotient of μ_E and the density ρ .

$$\left(\frac{\mu}{\rho}\right)_E = \mu_E * \frac{1}{\rho} \quad (1-4)$$

A CT acquisition for a single slice is the set of projection images from multiple projections (angles); when displayed as a function of their acquisition angle, the resulting image is called a sinogram. A sample object and its corresponding sinogram have been displayed in Figure 8. It is called a sinogram because the position of an object (e.g., the white circle at left in Figure 8) varies sinusoidally with the acquisition angle (e.g., the white sinusoid at right in Figure 8).

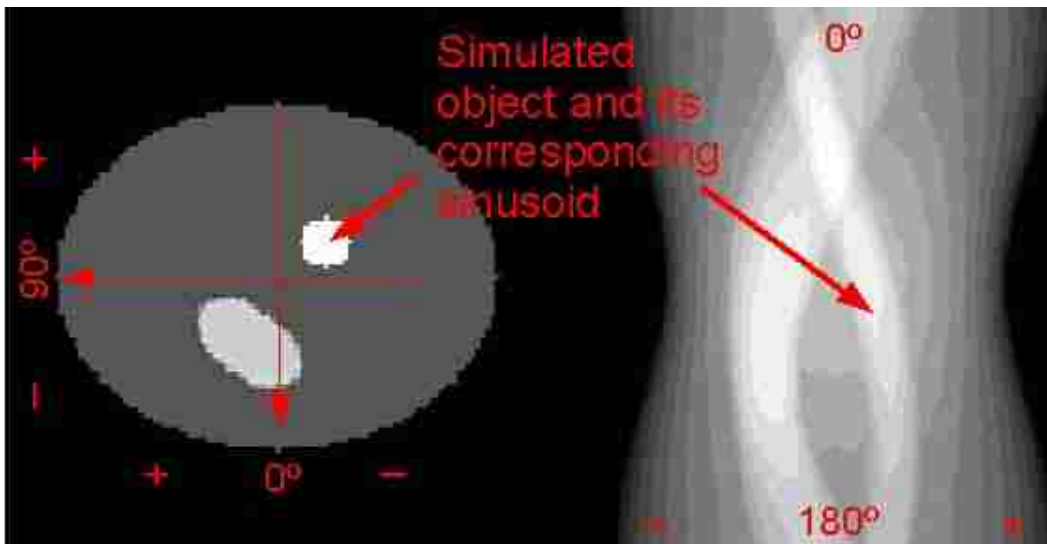


Figure 8: A simulated object (left) and its sinogram (right). Sinogram consists of projections acquired over 180° with 1° step size.

According to Radon's work, backprojecting the 2D images, typically slice by slice, reconstructs a 3D tomographic image of the subject. The tomography images

correlate to the approximate electron densities (due to primary Compton interactions) of the subject, which is used to calculate the radiation dose delivered to tissue in radiation therapy treatment planning. Filtered backprojection is one type of algorithm used to reconstruct the tomographic image from the individual projections. Each projection is added into the reconstructed image based on the angle at which it was taken.

The result of the backprojection is the subject convolved with $1/r$ blurring. This can be corrected using filtering in frequency space by multiplying by a ramp function (labeled “Ram-Lak” in Figure 9). Because this filter function continuously increases, it accentuates high frequency noise. This is undesirable. To counter this effect other possible filter functions, shown in Figure 9, are often employed to minimize the high frequency noise.

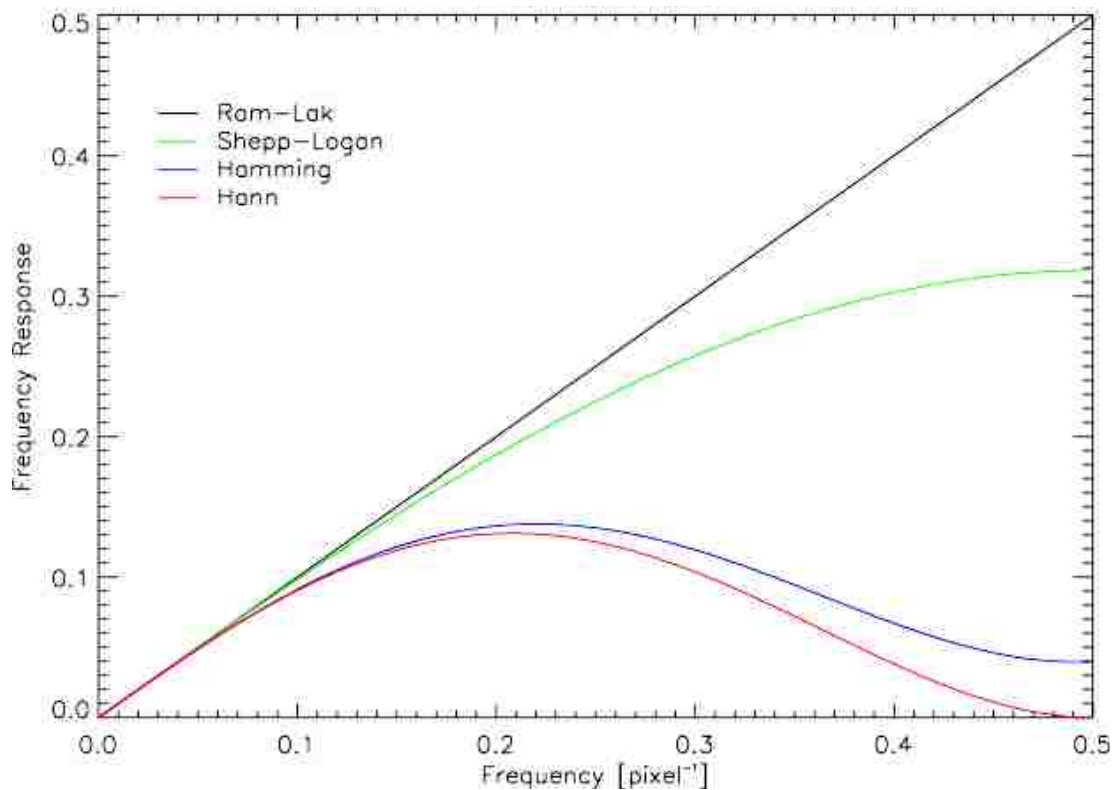


Figure 9: Typical filter functions used in CT.

The value of each pixel in the reconstructed image is proportional to the effective attenuation coefficient for that pixel. Due to the energy spectrum in polychromatic CT, the reconstructed value for a given pixel is a complicated function of the X-ray energy spectrum as well as the subject's attenuation properties. The polychromatic spectrum consists of mostly lower energy photons. As the lower energy photons are preferentially removed from the beam by the subject, the mean energy of the X-ray beam is increased in an effect called beam hardening, illustrated in Figure 10. This further complicates any determination of the actual attenuation coefficient for each pixel. Figure 11 shows the mass attenuation curve of water and iodine represented as functions of incident photon energy. The iodine absorption curve (illustrated in blue) exhibits a discontinuity at 33.169 keV which corresponds to the iodine K-edge. Discontinuities at lower energies correspond to the L-shell and M-shell binding energies.

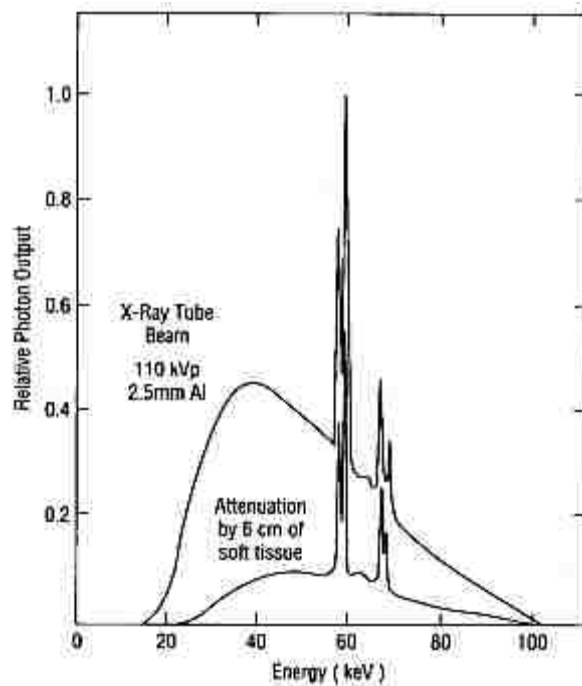


Figure 10: Beam hardening effect illustrated by comparing filtered x-ray spectrum to the same beam after traversing 6 cm of tissue (Dilmanian et al. 1992).¹²

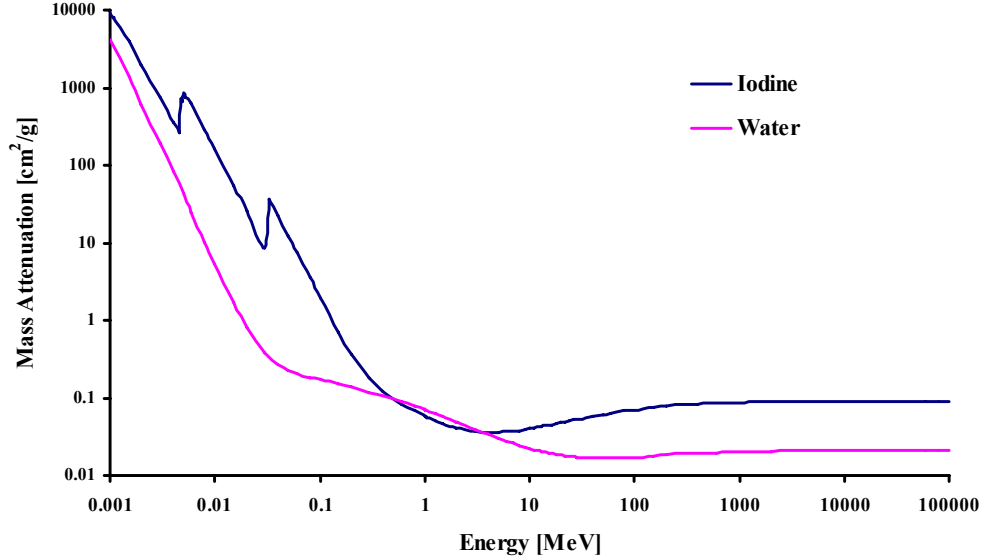


Figure 11: Mass energy absorption coefficients $[\mu_{en}/\rho]$ as a function of photon energy (MeV).¹⁷

One method used to record pixel values in CT images is to express the pixel values in the image relative to the attenuation coefficient of water. This is often called CT numbers or Hounsfield units (HU). In this scale, air is defined to be -1000 HU and water to be 0 HU with other materials being scaled linearly. The advantage of using this system is that it provides a means for comparison between different CT systems. The conversion from measured attenuation coefficients to HU is

$$HU = -1000 \left(\frac{\overline{ROI}_n - \overline{ROI}_{H_2O}}{\overline{ROI}_{Air} - \overline{ROI}_{H_2O}} \right) \quad (1-5)$$

The values \overline{ROI}_n , \overline{ROI}_{H_2O} , and \overline{ROI}_{Air} are the mean values of the n^{th} region of interest (ROI) and the ROIs pertaining to water and air respectively.

Another informative measure to assess the quality of a CT image is the contrast to noise ratio (CNR). The CNR measures the relative difference between a given value in

the image and the value for water. Assuming the noise magnitude doesn't depend on position in the image, the CNR based on multiple measurements is

$$CNR = \frac{\langle \overline{ROI}_n \rangle_M - \langle \overline{ROI}_{H_2O} \rangle_M}{\sigma_n} \quad (1-6)$$

where $\langle \overline{ROI}_n \rangle_M$ and $\langle \overline{ROI}_{H_2O} \rangle_M$ are the mean values of \overline{ROI}_n and \overline{ROI}_{H_2O} obtained from M measurements. The value σ_n is the standard error of $\langle \overline{ROI}_n \rangle_M$. A low CNR for a given ROI means that the signal is difficult to distinguish from water. A CNR of 3 or better is required to visually distinguish one region from background. Any noise will further obfuscate the signal.

Dual-energy subtraction and temporal subtraction are two image processing techniques that are useful for separating points of interest in an image from the background, including giving quantitative assessment. These methods require multiple scans of the same subject. Also, there are potentially novel hardware methods for obtaining multiple different –energy CT images from a single acquisition.^{18,19} These methods require specialized detectors or suffer from severe mispositioning artifacts from multiple acquisitions.

Dual energy subtraction involves the logarithmic subtraction of two x-ray/CT images obtained at widely separated energies.²⁰ Temporal subtraction requires two images to be obtained which are separated by time²¹ where factors such as composition vary. An example of this is CT data sets acquired before and after the administration of a contrast agent such as iodine, useful for angiography. In each case, the images are logarithmically subtracted from one another to accentuate the image contrast.

In CT contrast imaging the beam energy can be optimized for a particular agent such as iodine. The beam energy is tuned to slightly above the K- or L-shell binding energy where there is a significant increase in the attenuation. Dual-energy subtraction and temporal subtraction both can provide a quantitative analysis of contrast agent concentration.^{20,22} A special case of dual energy subtraction, more specifically called K-edge subtraction (KES), occurs when the monochromatic beam's energy or polychromatic beam's mean energy can be tuned to narrowly bracket the K-shell binding energy of specific contrast agents such as iodine (33.169 keV), gadolinium (50.239 keV), and platinum (78.395 keV) and then the resulting pair of images is subtracted (Figure 12).

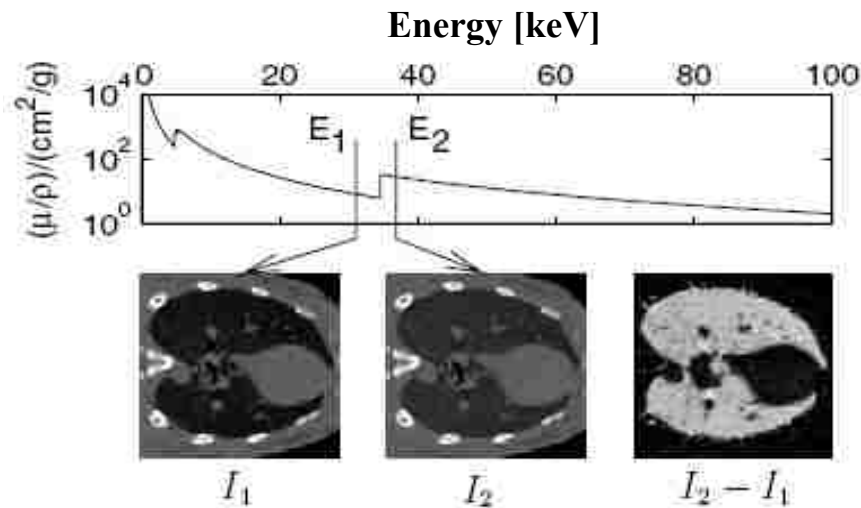


Figure 12: Example of K-edge subtraction (KES) results in thorax using xenon gas (K-edge of 34.56 keV) from Suhonen et al (2008).²³

At the K-edges of I, Gd, and Pt, the attenuation increases by factors of ~ 6 , ~ 5.4 , and ~ 4.7 respectively.¹⁷ Previous studies have suggested temporal subtraction to be more sensitive than KES in contrast imaging^{21,24} but temporal subtraction is not always suitable for clinical imaging. Work by Suhonen et al²³ has shown temporal subtraction to have a higher degree of noise and artifacts (Figure 13). Ideally, the CT images required

for KES could be obtained in a single acquisition by either using two separate x-ray sources or by using a beam splitter. This is not possible in temporal subtraction imaging.

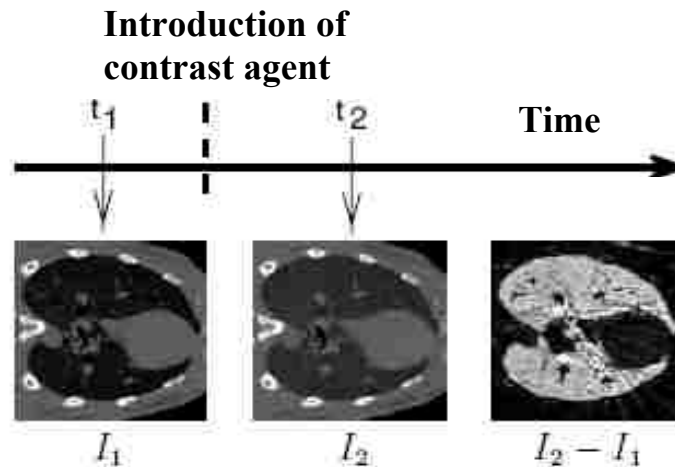


Figure 13: Example of temporal subtraction results from Suhonen et al (2008).²³

The work reported in this thesis focuses on KES for quantitative assessment of IUdR replacement. For X-ray activated Auger electron radiotherapy, knowing the high-Z target atom distribution will be important for treatment planning. The ability to image these high-Z target atoms is dependent upon the mass present per unit volume. In the case of breast cancer, a 1 cm^3 tumor has approximately 1.07×10^9 cells.²⁵ Assuming that IUdR replaces 18% of thymidine, which comprises about 25% of the roughly 5.8×10^9 bases per cell nucleus, and using the molar mass of iodine (127 g/mole), the iodine concentration in breast cancer will be approximately $60 \mu\text{g cm}^{-3}$.

1.4 Previous Synchrotron Based Iodine Imaging Studies

One of the principal concerns regarding x-ray activated Auger electron radiotherapy is the ability to determine the amount of IUdR uptake and its spatial distribution. The governing factor in determining the uptake and distribution is the

minimum detectable concentration of IUdR, or more specifically, iodine in tissues for several types of quantitative imaging techniques. Several studies have investigated the minimum detectable concentration of iodine. The use of radiolabeled IUdR allows for radioisotope imaging methods to image iodine. Iodine-131-iododeoxyuridine and iodine-123-iododeoxyuridine have been used in single photon emission computed tomography (SPECT)^{26, 27} and iodine-124-iododeoxyuridine has been used in positron emission tomography.²⁸ Neither method is suitable for small concentrations of iodine due to low count rates; poor spatial resolution is also a problem.

A planar imaging study by Baldelli et al compared the results of European Synchrotron Radiation Facility (ESRF) monochromatic x-rays to those of a clinical digital mammography system. For each system, KES and TS methods were used to measure the minimum iodine concentration detectable. For the KES techniques, images were acquired at energies bracketing the iodine K-edge at 32.5 keV and 33.9 keV. Using KES and TS, the estimated minimum iodine concentrations detectable with the SR system were $9.0 \times 10^2 \mu\text{g cm}^{-3}$ and $8 \times 10^2 \mu\text{g ml}^{-3}$ respectively. The minimum detectable iodine concentration detectable using KES and TS with the digital mammography system were $4.13 \times 10^3 \mu\text{g cm}^{-3}$ and $1.01 \times 10^3 \mu\text{g cm}^{-3}$, respectively. The minimum detectable iodine concentration was determined as the minimum amount required to visualize a detail with a contrast-to-noise ratio of 5.²⁴

A previous study focusing on CT imaging by Dilmanian et al, was aimed at determining the minimum detectable iodine concentration using SR at the National Synchrotron Light Source. A 135 mm diameter acrylic phantom with 11 mm channels was employed to image iodine concentrations ranging from $15 \mu\text{g cm}^{-3}$ to $240 \mu\text{g cm}^{-3}$. A

phantom is a synthetic test subject, often used to simulate a patient for imaging or dosimetric studies. Using KES methodology, images were acquired with energies bracketing the iodine K-edge at 33.09 keV and 33.25 keV. The system was able to measure iodine concentrations as low as $60 \mu\text{g cm}^{-3}$. The image noise was measured to be ~ 1 Hounsfield Unit (HU). The same phantom imaged with a conventional CT system produced image noise of ~ 3 HU.²⁹

A study by Elleaume et al²¹ compared SR based CT results using KES and TS of iodine solutions in concentrations ranging from $50 \mu\text{g cm}^{-3}$ to $5 \times 10^3 \mu\text{g cm}^{-3}$ using the monochromatic x-rays at ESRF. The KES method imaged the solutions at energies bracketing the iodine K-edge while for the TS technique the energy was set to 50 keV. The determination of the minimum detectable concentration was based on a SNR of 3. For an iodine concentration of $100 \mu\text{g cm}^{-3}$, the level of error in KES and TS measurements were found to be in agreement and amount to less than 10%. The experimental results found the minimum detectable iodine concentration to be $185 \mu\text{g cm}^{-3}$ and $90 \mu\text{g cm}^{-3}$ for KES and TS respectively.

Suhonen et al performed *in vivo* studies with SR based CT of ventilation and blood flow in rabbit lungs using combined KES and TS. In this study, KES and TS images were obtained simultaneously at energies above and below the iodine and xenon K-edges. The advantages of simultaneous imaging are a reduction of motion artifacts and decreased acquisition time. Quantitative analysis was performed of iodine in lung blood vessels and xenon in ventilation airways which was used to compare the results of KES and TS. The study found that concentration quantification using TS when compared to using KES, agreed well in the case of xenon but was on average 20% lower in the case of

iodine (Figure 14). Additionally, the noise in TS was higher than that of KES. This was attributed to misregistration of the temporally separated images which contributed to a factor of $\sqrt{2}$ increase in the standard deviation.²³

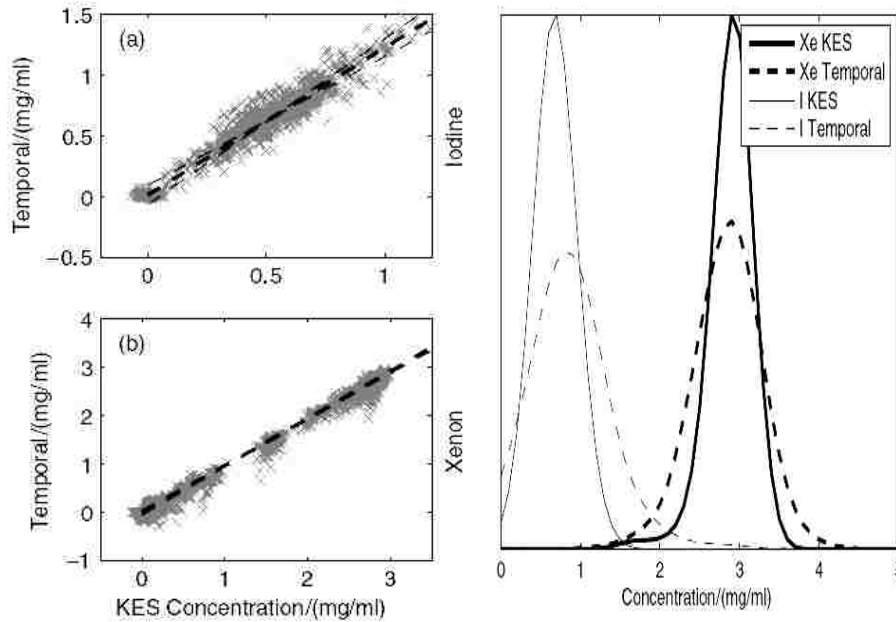


Figure 14: Results from Suhonen et al (2008) comparing KES and TS techniques.²³ The left two images show the concentration quantification comparison of KES and TS using iodine (top) and xenon (bottom). The above right image shows concentration histograms in part of a rabbit’s lung for KES and TS using iodine and xenon.

1.5 Hypothesis and Specific Aims

This present study used a Skyscan-1074 bench top micro-computed tomography system to obtain conventional CT images and Louisiana State University’s CAMD synchrotron to obtain CT images with monochromatic x-rays. These two systems were evaluated to determine the minimum detectable iodine concentration and to develop a methodology to image CHO cells containing IUdR-labeled DNA for use in the future

development of an x-ray activated Auger electron radiotherapy treatment planning system.

The hypothesis of this thesis was that using the current image acquisition and processing setup for these systems, an iodine concentration in CHO cells of 0.06 mg ml^{-1} can be measured from the CT image data with a contrast to noise ratio of 3. The specific aims for this project have been classified into three tasks.

- 1) Polychromatic CT Sensitivity Measurements: determine the minimum detectable iodine concentration using the Skyscan-1074 benchtop microCT system. The minimum iodine concentration will be determined by the CNR obtained from HU calculations.
- 2) Monochromatic CT Sensitivity Measurements: determine the minimum detectable iodine concentration using CAMD's microCT system for energies above and below the K-edge of iodine. The minimum iodine concentration will be determined by the CNR obtained from HU calibration and from KES calculations.
- 3) In Vitro Imaging Study: image IUdR-labeled CHO cells to quantify in vitro iodine concentration. Evaluate feasibility of quantifying IUdR uptake in cell cultures based on HU and KES results.

Chapter 2. Aim 1, Polychromatic CT Sensitivity Measurements

Determine the minimum detectable iodine concentration using the Skyscan-1074 benchtop microCT system.

2.1 Goals

The first goal was to develop methodology for use with the Skyscan-1074 benchtop microCT system to determine the minimum iodine concentration that produces a signal with a CNR greater than 3. The second goal was to obtain a calibration curve to relate CT number to iodine concentration.

2.2 Analytical Approach

Multiple scans of various iodine concentrations were used to determine the minimum detectable concentration based on a CNR greater than 3 and a calibration curve was created to provide a means of determining the uncertainty in the iodine concentration based on the mean CT number from a single measurement. With limited CAMD synchrotron beamtime available, this specific aim served to establish methodology to be applied to the CAMD system in specific aim 2.

2.3 Materials and Methods

2.3.1 Microtomography System

The Skyscan-1074 Portable X-Ray Microtomograph (Figure 15 and Figure 16) uses an rtw RÖNTGEN-TECHNIK DR. WARRIKHOFF GmbH & Co. KG brand metal-ceramic x-ray tube, model number MCB 65 C – 0.2 W. The air-cooled x-ray tube uses a tungsten target and has a 0.2 mm × 0.2 mm focal spot with 0.2 mm inherent beryllium filtration. The tube operates with selectable high-voltage settings from 20 - 40 kVp with a maximum anode load of 40 W at 1000 μ A.

The x-ray detector is a Pulnix TM-6AS 8-bit charged-coupled device (CCD) camera with 768×576 pixels. The camera lens is coupled to a scintillator. The scintillator is P43 powder scintillator (GdO) 20 μm thick. The maximum reconstructed field of view is $27.2 \text{ mm} \times 27.2 \text{ mm} \times 18.9 \text{ mm}$. Projection images are acquired with conebeam geometry.



Figure 15: Skyscan-1074 Portable X-ray Microtomograph system (right) connected with a desktop computer for image acquisition.



Figure 16: Skyscan-1074 imaging compartment. Samples are placed on the stage (pedestal in image center) which rotates. The x-ray tube (not shown) produces a “cone” of x-rays which travel from right to left. The scintillator is located behind the circular mylar-covered window at left.

2.3.2 Image Acquisition

Images were acquired using Skyscan 1074 v 2.1 software. The software allows user control of the x-ray tube's voltage and current. This software offers several user adjustable acquisition settings, including: 180° or 360° acquisition range, projection step size, flood field correction, geometric correction, exposure time, projection averaging, gain, and median filtration.

The Skyscan 1074 v 2.1 software allows the user to calibrate the system's rotational alignment. The system requires periodic alignment calibration due to mechanical stresses on the object stage. These stresses force the rotation axis of the object stage out of alignment with the x-ray tube focal spot and the center of the detector array. This effect is illustrated in Figure 17.

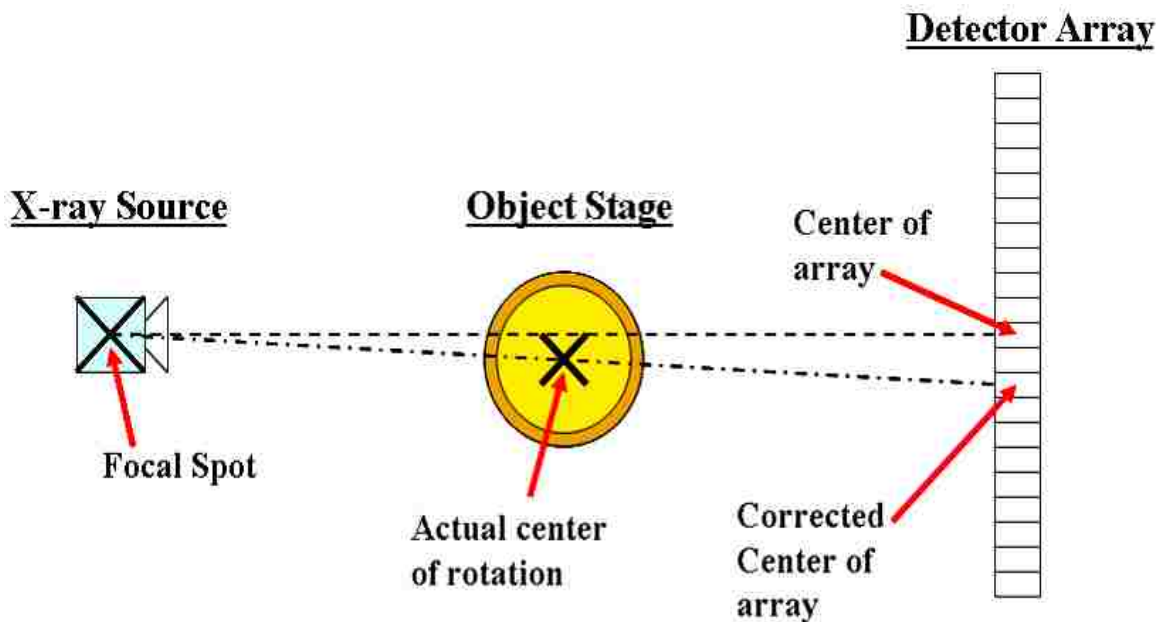


Figure 17: Schematic of X-ray source, object rotation center, and detector array center (top view). The dashed line shows the expected collinear arrangement of the source, object center, and detector center used for reconstruction. The dashed-dotted line shows the results of an alignment correction.

The Skyscan 1074 v 2.1 system uses a long straight object, placed on the object stage and oriented with its long axis vertically, to perform the alignment calibration. We used a standard thumb-tack for alignment calibration. To secure the thumb-tack to the stage, removable adhesive putty was placed between the plastic bottom of the tack and the alignment stage. The automated calibration activated the x-ray tube and acquired 8 different projections of the tack to use for calculating the required center of rotation correction. For all studies, an alignment calibration was acquired prior to each set of acquisitions.

A flood (open) field correction minimizes the effects of pixel to pixel non-uniformities and x-ray field inhomogeneity. To obtain the flood field images, all samples were removed from the imaging compartment to obtain a completely open field. An averaged open field image is shown in Figure 18. Under responding pixels appear dark and over responding pixels appear white. The average flood field pixel value was 34116 with the lowest and highest pixel values being 30497 and 46330 respectively. It was required for each unique voltage, current, exposure time, and gain setting used for data acquisition; each combination of these settings resulted in a different flood field correction.

It was recommended in the help files accompanying the software to periodically obtain new flood field images to correct for the change in detector response over time. For all studies, a flood field correction was acquired prior to any new set of acquisitions. The average standard error in the mean pixel values for 211 flood field images and the corresponding standard deviation in the standard error was 1.39 ± 0.10 on a scale of 0 to 65535 based on an image size of 736×512 pixels.



Figure 18: Skyscan-1074 open field. The pixel values representing photon counts are displayed in grayscale. Tube settings were 40 kVp, 1000 μ A, 420 ms exposure time, 100% gain. This open field image is an average of five acquisitions.

The CT data were acquired with the 360° acquisition range and a step size of 0.9°. The 360° setting was chosen instead of 180° acquisition setting because the former resulted in a more uniform reconstructed image, as shown in Figure 19. A blank acrylic phantom was imaged over a 360° range. Two reconstructions of the phantom were performed. The first reconstruction used only the 0° to 180° projections and the second used all projections from 0° to 360°. To compare the results, a 140×140 pixel ROI was selected from the center of each image. The relative instrumental uncertainty was calculated by dividing the standard deviation of pixel values within the ROI by the mean value of the ROI. The relative uncertainties for the 180° and 360° reconstructions were 0.08 and 0.05, respectively. Because a lower value corresponds to a more uniform image, the 360° acquisition setting was chosen.

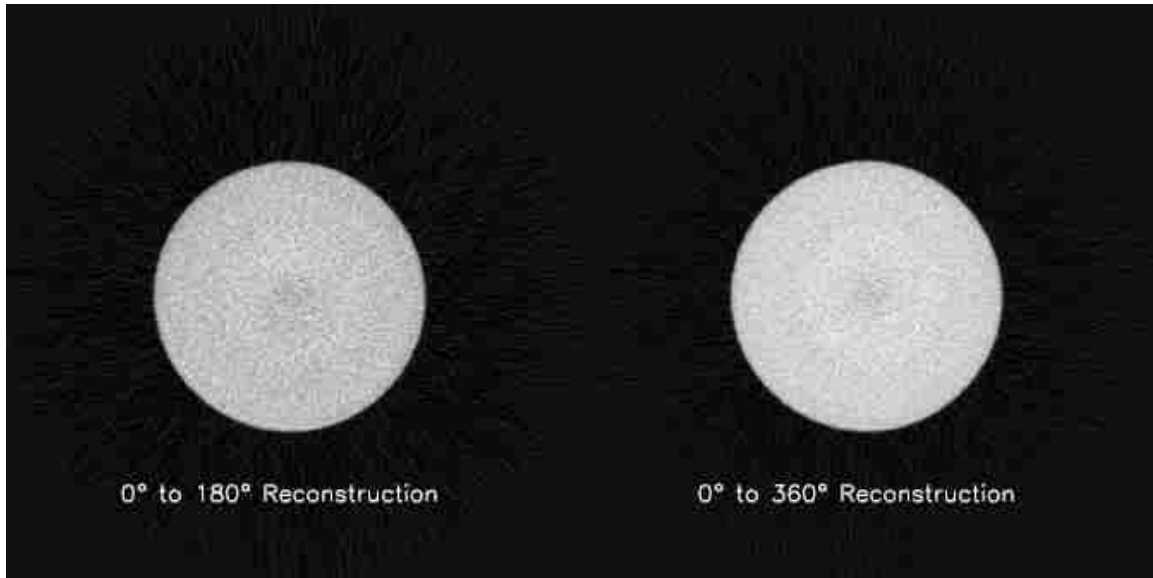


Figure 19: Reconstruction of the central slice of a blank acrylic phantom acquired on Skyscan-1074. The left image was reconstructed using only the 0° to 180° projections. The right image was reconstructed using the 0° to 360° projections. The 0° to 180° projections for both images are the same.

The flood field correction setting was enabled for all acquisitions. The median filter setting was enabled to remove the effects of bad CCD pixels. The geometric correction setting was enabled to correct for geometrical distortion of the x-ray conebeam projected onto the flat scintillator.

The projection averaging setting allowed for a user defined number of identical acquisitions for each projection which would be averaged. This setting was disabled as it caused very long acquisition times during which it was noticed that the tube current would unexpectedly drop. This was attributed to overheating in the tube. This problem was circumvented by making multiple identical acquisitions of the sample while allowing sufficient time for tube cooling. The multiple projections were then averaged later using software developed in house in IDL.

The SkyScan 1074 instructions were followed to select exposure time and gain setting. First, the sample was placed on the pedestal in the scanner. The x-ray tube was set to the desired voltage and current settings. Projections were acquired in live acquisition mode starting at the lowest gain setting of 100%. Using the display of a profile of the x-ray intensity transmitted through the sample, with the gain held at 100% the exposure time was adjusted until the profile exhibited the largest amount of transmission without saturating the CCD. For the samples scanned in these studies, a 420 ms exposure time and a gain setting of 100% were chosen from this adjustment process. Acquisition parameters have been compiled in Table 2.

Table 2: Skyscan-1074 acquisition parameters.

Flood Field Correction	enebled
Median Filtration	enebled
Gain	100%
Step Size [°]	0.9
Exposure Time [ms]	420
Voltage [kVp]	40
Current [μ A]	1000

2.3.3 Phantom Construction

A phantom was constructed from polymethyl methacrylate (PMMA) to perform the concentration studies. Designed to fit within the Skyscan-1074 field of view, the phantom was a cylinder of dimensions 2.6 cm height and 1.25 cm diameter. Five 0.19 cm diameter holes were drilled parallel to the long axis of the phantom to a depth of 1.5 cm to later hold iodinated solutions. The holes were arranged according to the diagram shown in Figure 20. A typical cross-sectional reconstructed image of the phantom is displayed in Figure 21.

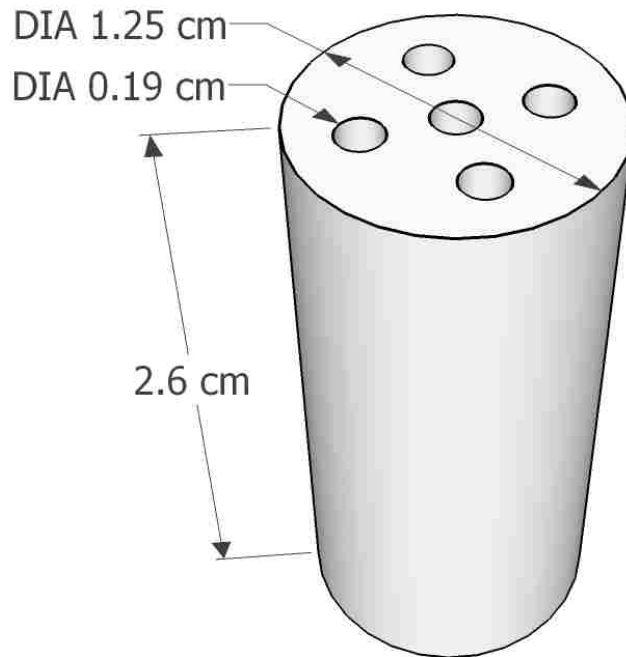


Figure 20: Skyscan-1074 PMMA phantom. Each of the 5 sample holes were 1.5 cm deep.

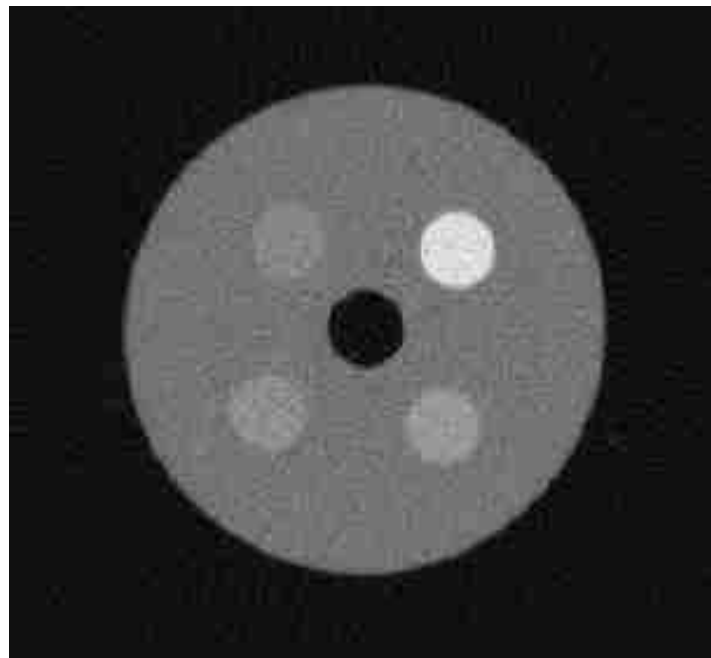


Figure 21: Reconstructed image of Skyscan phantom with iodine solutions from NRecon® software. The central hole contained air while the remaining 4 holes contained a water solution having 0.0, 2.5, 5.0, 25.0 mg cm^{-3} of iodine (CCW from the top left). The image was acquired with the acquisition parameters listed in Table 2.

2.3.4 Image Reconstruction

Image reconstruction was performed using NRecon® (Skyscan, Kontich, Belgium) software. The reconstruction process began by selecting the desired projection data. The reconstruction process included auto-misalignment compensation, the maximum setting for ring artifact reduction, and a beam hardening correction. A setting of 55% was selected for the beam hardening correction, following the selection process described in the NRecon® software manual. This setting was qualitatively sufficient to minimize cupping effects due to beam hardening within the PMMA phantom.

After selecting the reconstruction parameters, a preview image was reconstructed for a slice near the middle of the data set. The histogram of this slice was windowed to a fixed range of -0.0018 to 0.0260 pixel values, which are proportional to the attenuation coefficients. This range encompassed the expected range of pixel values for all iodine concentrations; using a fixed range for all data ensured that different image sets were reconstructed with the same range. The images were saved out as TIFF format files. During reconstruction, NRecon® uses a fixed Hamming window filter similar to the one shown in Figure 9.

2.3.5 Concentration Measurements

Iodinated contrast solutions were created by diluting measured volumes of Reno-30® (diatrizoate meglumine), a radiopaque contrast agent used clinically for retrograde pyelography, with distilled-deionized water. Each milliliter of Reno-30® contains 300 mg diatrizoate meglumine ($C_{11}H_9I_3N_2O_4 \cdot C_7H_{17}NO_5$) with 3.2 mg sodium citrate ($Na_3C_6H_5O_7$) as a buffer, resulting in approximately 141 mg cm^{-3} organically bound iodine. Iodine dilutions of 0.0, 0.03, 0.05, 0.1, 0.25, 0.5, 1.0, 2.5, 5.0, 10.0, and 25 mg

iodine cm^{-3} were used. The iodinated solutions were imaged in three of the peripheral wells of the concentration phantom; the fourth well and the central well always contained distilled-deionized water and air, respectively.

Each well of iodinated solution in the concentration phantom formed a column in the reconstructed tomographic volume. The tomographic data were analyzed using software written in IDL (ITT Visual Information Studios, Boulder, CO, USA). On one cross-sectional slice, a circular ROI was defined for each well containing solution and another circularly defined ROI in air located outside the phantom for a total of 5 ROIs. The ROIs corresponding to solutions were centered in the wells and were small enough such that they were completely contained within the well. The diameter of each ROI was approximately 0.096 cm. The 5 ROIs were copied to all slices of the reconstructed data.

The mean pixel value and standard deviation of the mean were calculated for each ROI in a slice. Using the values for air and water, the mean ROI values were converted to Hounsfield units on a slice-by-slice basis (equation 1-5). The resulting ROI values in Hounsfield units were then averaged over all slices (typically 250). The lowest measured concentration, which produced a CNR of 3 or higher (from equation 1-6), was used as the estimate of the lower limit of detection.

The data were fit to a $Y = a X$ model. The reduced chi-squared error statistic (χ_v^2) was calculated as

$$\chi_v^2 = \frac{1}{N} \sum \left(\frac{(Y - \hat{Y})^2}{\sigma^2} \right) \quad (2-1)$$

where N is the number of data points used in the fit. Y is the mean HU value for a given concentration of iodine and \hat{Y} is calculated HU for a given iodine concentration based on the linear model. σ is the standard error in HU for a given iodine concentration.

Using the above data, a plot of mean HU was plotted versus iodine concentration for all concentrations. The error in the mean HU for each concentration (\overline{HU}) was determined by averaging the results from multiple CT acquisitions. From the data, the 95% prediction interval and 95% confidence interval for the slope of the line were calculated.³⁰ The 95% confidence interval for the slope of the fit line is the range of possible slopes for the data that have a 95% probability for containing the true slope. The confidence interval (CI) is defined as

$$CI = t_{v,\alpha} \frac{RMSE}{\sqrt{\sum (X_i - \bar{X})^2}} \quad (2-2)$$

where RMSE is the root mean squared error. X_i and \bar{X} are the mean value for a given iodine concentration and the mean of all iodine concentrations respectively and $t_{v,\alpha}$ is the t-value of the two tailed Student's t-distribution as a function of the probability $(1 - \alpha)$ and the number of degrees of freedom.

A 95% prediction interval is the HU range for a given iodine concentration where there is a 95% probability that the next experiment's HU value will occur. Prediction intervals are useful for predicting, for a given X value, what the Y value of the next experiment will be. It can be used to determine possible range of iodine concentrations that could produce a given HU value. The prediction interval (PI) for N data points is

$$PI = t_{v, \alpha} RMSE \sqrt{1 + \frac{1}{N} + \frac{\left(X_i - \bar{X}\right)^2}{\sum \left(X_i - \bar{X}\right)^2}} \quad (2-3)$$

where the terms have been defined in preceding paragraphs.

2.3.6 Resolution Measurements

To compare the Skyscan-1074 and the CAMD microCT results from the iodine concentration studies, a standard reference between the systems was required.

Fundamental differences between the two imaging systems made any direct comparison difficult. To compare the systems, a measurement of imaging performance is useful.

Spatial resolution is a measure of the system's ability to image fine detail or to resolve small structures. To measure this, a protocol outlined by the American Society for Testing and Materials (ASTM E 1695-95) was employed.³¹

Following ASTM E 1695-95 protocol, a second PMMA phantom was constructed identical in dimension to the one used for the Skyscan concentration studies but without any holes. The blank phantom, henceforth called the MTF test phantom, was imaged using identical acquisition (Table 2) and reconstruction parameters. An algorithm was written in IDL to perform the analysis of the system resolution. The flowchart in Figure 22 outlines the process for obtaining the MTF from an input image.

In the determination of the Skyscan-1074 imaging system performance, each reconstructed slice was bit-scaled using a threshold at approximately 1/3 the average phantom pixel value to create a mask. Pixel values above the threshold corresponding to phantom material were set to unity and all values below the threshold were set to a value of zero. A value of 1/3 the average pixel value of the MTF test phantom was chosen

because it was well above the average pixel value of air but low enough to include nearly all the cylindrical PMMA phantom.

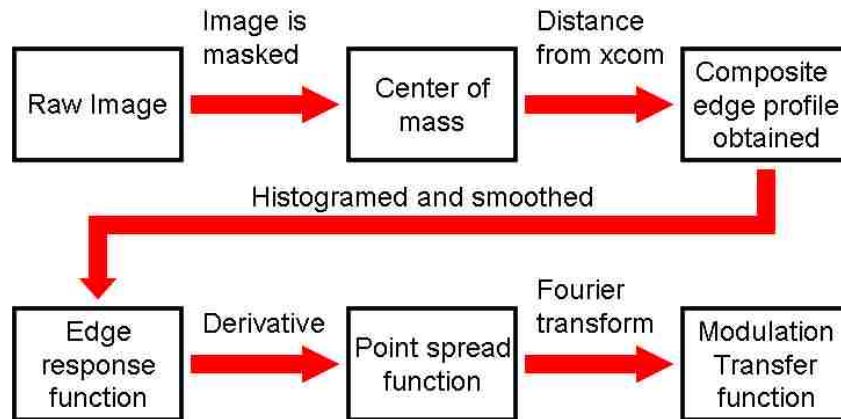


Figure 22: Flow chart showing the process for obtaining the modulation transfer function from a raw image of the MTF test phantom.

The resulting mask for each slice was analyzed using a center-of-mass calculation to determine the center of the phantom for each slice. An edge response function (ERF) was created by plotting every pixel as a function of its distance from the center of mass of the phantom for all slices. The ERF data points were histogrammed into bins of size 7.4 μm . A 41 point piece-wise cubic fit was applied to smooth the data. The analytical derivative of the ERF was then obtained which is the point spread function (PSF). A 41 point piece-wise cubic fit was then applied to the PSF to further smooth the data. The Fourier transform of the PSF then is the modulation transfer function (MTF).

To ensure that the routine written in IDL was functioning correctly, test data were created to simulate the PMMA phantom. A 736×736 array was created with a circle in the center. The circle diameter was 337 pixels which equates to 1.25 cm which is the diameter of the actual MTF test phantom. The circle and its interior were all set to a value of 1000 while the exterior was set to zero. The image was then convolved with a two

dimensional Gaussian filter function with σ of 9 pixels (0.33 mm) to simulate image blur. The resulting simulated image (Figure 23) was then analyzed as before to obtain the PSF shown in Figure 24.

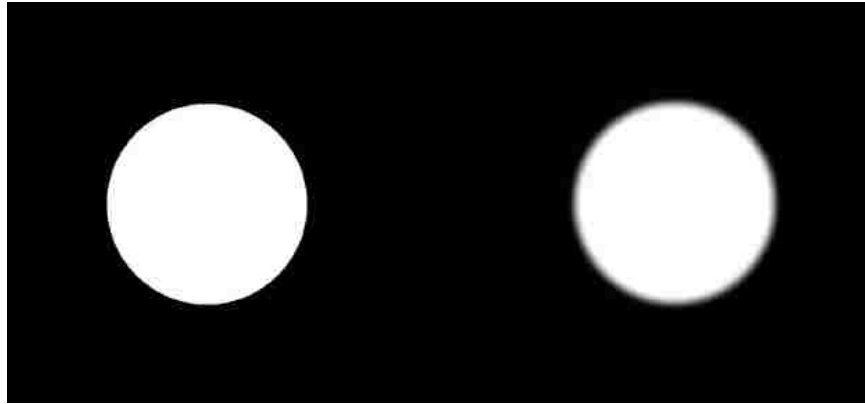


Figure 23: Simulated data to test proper function of the MTF calculation routine. On the left is a circle 337 pixels in diameter to approximate the MTF test phantom. The image on the right is the left image convolved with a 2D Gaussian filter with σ of 9 pixels.

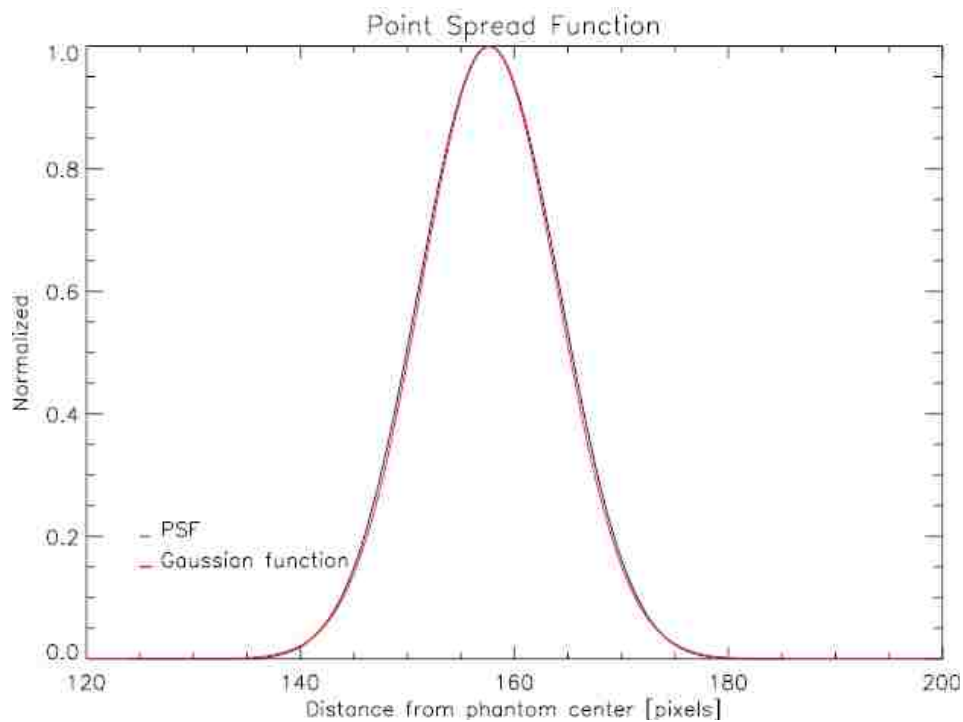


Figure 24: PSF obtained from the simulated MTF image is displayed in black. Displayed in red is the one dimensional representation of the Gaussian filter ($\sigma = 9$) that generated the simulated image. The calculated PSF agreed closely with the true Gaussian PSF.

2.4 Results

2.4.1 Concentration Measurements

Table 3 summarizes the ROI analysis results. Figure 25 plots the mean measured CT number as a function of iodine concentration up to 1.0 mg ml^{-1} . The data were fit to a line constrained to go through the origin ($Y = a X$), shown as the solid black line in Figure 25. The slope was $35.28 \pm 2.75 \text{ [HU mg}^{-1}\text{ml]}$ with $\chi_v^2 = 55.2$ and 5 degrees of freedom. The 95% confidence interval is shown as solid red lines and the 95% prediction interval is shown as dashed black lines. Figure 26 plots CT number vs. iodine concentration up to 10 mg ml^{-1} . This data was also fit to the linear model; only the trend line and prediction interval have been plotted for clarity. The slope was $31.70 \pm 0.26 \text{ [HU mg}^{-1}\text{ml]}$ (black line) with $\chi_v^2 = 51.1$ and 8 degrees of freedom.

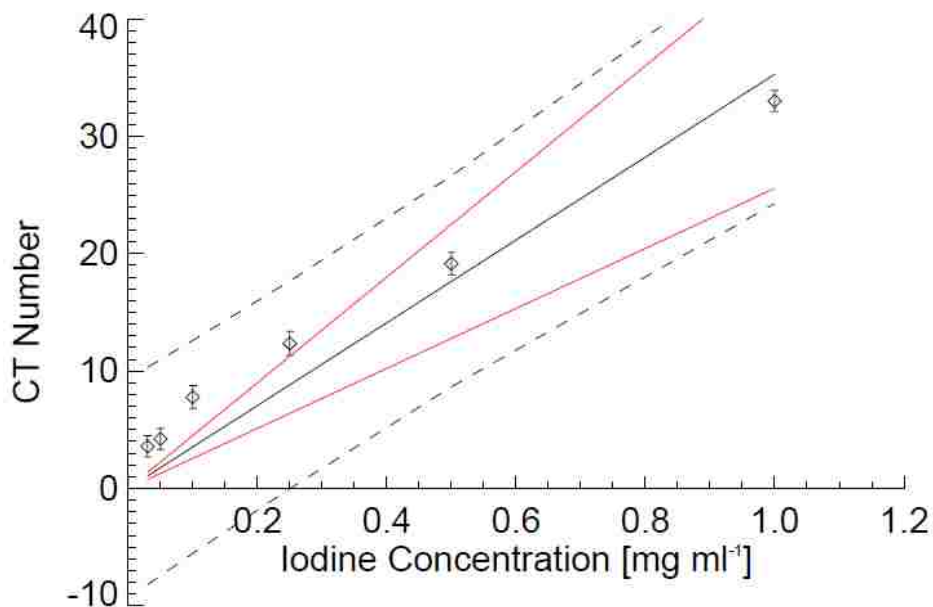


Figure 25: Skyscan results plotted in CT number vs. iodine concentration up to 1 mg ml^{-1} for CT acquisition at 40 kVp. The solid black line represents a linear fit constrained to go through the origin ($\chi_v^2 = 55.2$). The solid red and dashed black lines represent the 95% confidence and prediction bands. Error bars represent the standard deviation.

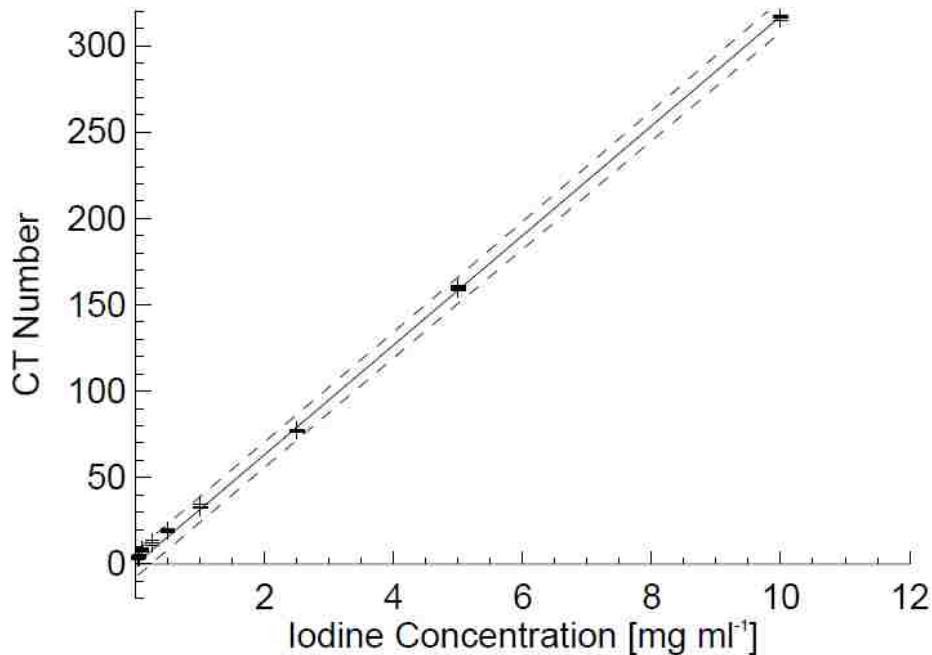


Figure 26: Skyscan results plotted in CT number vs. iodine concentration up to 10 mg ml⁻¹ for CT acquisition at 40 kVp. A linear fit of the data with $\chi_v^2 = 51.1$ (black line), and 95% prediction interval (dashed lines) are shown. The individual data points have been plotted to illustrate the spread of the measurements at each concentration.

All of the individual measurements compiled in Table 3 were used to compute mean HU and CNR for each concentration with the corresponding standard deviation. The standard deviation was calculated from five data points for each concentration, and the standard error was then calculated by propagation of errors from initial uncertainty in each ROI. The average standard error for any iodine concentration using this method was approximately 0.08 HU. This value is a factor of 5 times smaller than the standard error calculated solely from the spread in the data points (0.4 HU) and does not adequately represent the results. The lowest concentration of iodine measured to produce a CNR of 3 or higher was 0.1 mg ml⁻¹ of iodine.

Table 3: Results from the Skyscan-1074 measurements at 40 kVp.

I [mg ml ⁻¹]	Mean pixel value from ROI [HU] ^a					Mean HU	Std Dev ^b	Std Err ^b	CNR
	Acq 1	Acq 2	Acq 3	Acq 4	Acq 5				
0.03	3.44	3.78	3.14	2.55	4.98	3.58	0.90	0.40	1.77
0.05	5.44	4.05	4.75	3.08	3.77	4.22	0.91	0.41	2.08
0.1	7.71	8.29	7.05	6.72	9.14	7.78	0.97	0.43	3.58
0.25	12.49	11.05	12.39	11.97	13.87	12.36	1.02	0.46	5.41
0.5	19.84	20.26	18.40	18.00	19.28	19.16	0.95	0.43	9.01
1	34.36	33.15	32.47	31.98	33.09	33.01	0.89	0.40	16.51
2.5	78.09	76.86	76.78	77.87	76.39	77.20	0.74	0.33	46.77
5	160.89	160.14	159.37	159.30	158.37	159.61	0.95	0.43	75.07
10	317.74	314.37	317.52	316.49	316.09	316.44	1.35	0.60	105.01

^a The standard error of each mean ROI value is not shown.

^b The standard deviation and standard error represent the uncertainty based on the repeat measurements of the pixel values' mean.

2.4.2 Resolution Measurements

The MTF is a measure of the spatial frequency response of an imaging system and is usually measured in line pairs per millimeter (lp mm⁻¹). When stating a system's resolution it is often reported at 10% maximum and allows for inter-comparison between imaging systems to assess performance. In this case, using the MTF test phantom, the MTF measured at 10% the maximum response was 5.5 lp mm⁻¹. The results of the MTF measurements are displayed in Figure 27.

2.5 Discussion

2.5.1 Concentration Measurements

Skyscan's lower limit of detection of 0.1 mg ml⁻¹ at a CNR of 3.58 is insufficient to quantify the IUdR uptake in a breast cancer with a thymidine replacement of 18%. The large value of the reduced chi-squared statistic indicates that a linear fit through the origin is a poor model for this polychromatic CT system. It may be possible to improve the detection limit by reducing the noise. Using larger pixels (e.g. 1 mm) in the image acquisition will sacrifice spatial resolution, but each new larger pixel should have

relatively lower noise so this may be one method for improving the CNR at lower iodine concentrations (current pixel size is 37.4 μm). If clinical implementation requires ~ 1 mm resolution, then it may be practical to sacrifice resolution for reduced noise. The image noise in the Skyscan system was ~ 1 HU. Previous imaging studies involving conventional CT have measured iodine concentrations as low as 0.06 mg ml^{-1} with image noise on the order of ~ 3 HU.²⁹

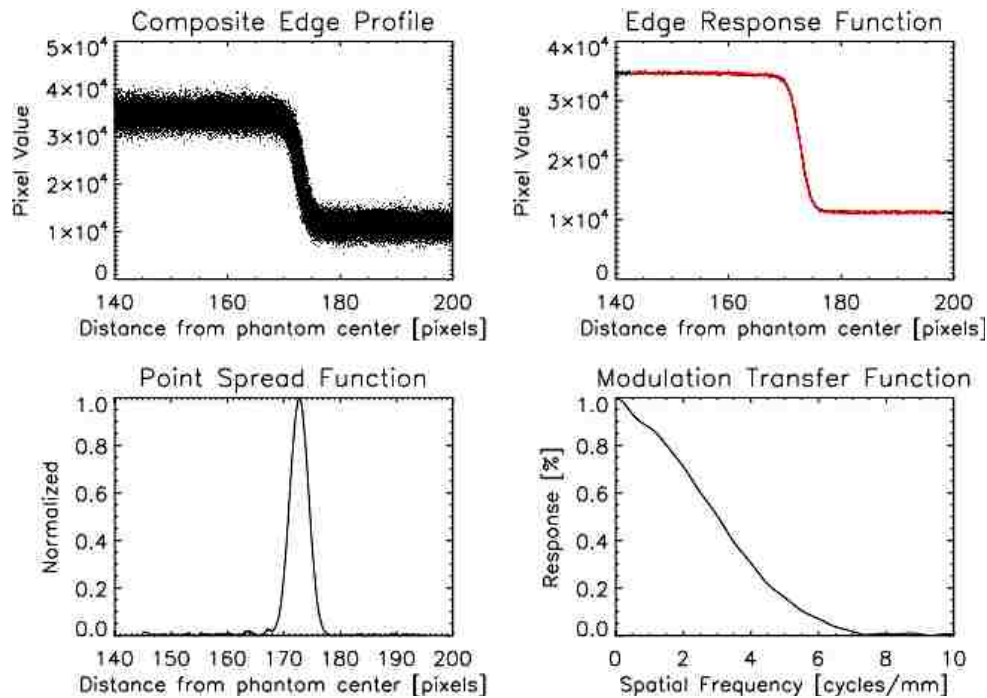


Figure 27: The composite edge profile is shown in the top left which is smoothed to obtain the ERF (top right). The analytical derivative of the ERF is used smoothed to produce the PSF (bottom left). The Fourier transform of the PSF is the MTF (bottom right) measured for the Skyscan-1074 system. The spatial frequency of the MTF measured at 10% of the maximum was found to be 5.5 lp mm^{-1} .

2.5.2 Resolution Measurements

The MTF has been successfully measured for the Skyscan-1074 system using ASTM E 1695-95 protocol. From this, 10% of the MTF was found to occur at 5.5 lp

mm^{-1} . By comparison, 10% of the MTF for a clinical GE LightSpeed RT scanner occurs at 5.8 lp/cm (NHS Purchasing and Supply Agency, London).

Some of the primary factors affecting the system resolution are the polychromatic spectrum, the finite dimensions of the X-ray tube focal spot, the conebeam geometry, CCD pixel size and depth, and stage rotation step-size. The evaluation of the MTF for the Skyscan system indicates that the system has resolution to spare in terms of the needs of the treatment planning for x-ray activated Auger electron radiotherapy. By going to a larger pixel size, the spatial resolution will be sacrificed in favor of improved noise performance.

Chapter 3. Aim 2, Monochromatic CT Sensitivity Measurements

Determine the minimum detectable iodine concentration using CAMD's microCT system.

3.1 Goals

The first goal was to apply methodology developed on the Skyscan-1074 imaging system to the CAMD microCT system to determine the minimum iodine concentration that produces a signal with a CNR greater than 3. The second goal was to obtain a calibration curve to relate CT number to iodine concentration. The third goal was to apply KES techniques to directly quantify the iodine concentration.

3.2 Analytical Approach

Multiple scans of various iodine concentrations acquired at energies 32.5 keV and 33.5 keV were used to determine the minimum detectable concentration based on a CNR greater than 3. A calibration curve was created to provide a means of determining the uncertainty in the iodine concentration based on the mean CT number from a single measurement. A K-edge subtraction was then applied to the data. The minimum detectable iodine concentration and calibration curve was determined as before. This specific aim serves to establish methodology to be applied to imaging IUdR-labeled CHO cells using the CAMD system in specific aim 3.

3.3 Materials and Methods

3.3.1 CAMD Synchrotron Facility

The CAMD synchrotron consists of a ring (octagon) for beam transport that has 8 bending magnets (radius of 2.928 m) that each bend the beam 45°. Two straight portions of the accelerating ring accommodate insertion devices. One produces the x-ray beam

used in this study. It contains a wiggler consisting of a 3-pole superconducting magnet with maximum field strength of 7 T at the central pole and 1.55 T at the ends.

Photons for the various CAMD beamlines are produced in two ways. Beamlines located tangential to the bending magnets receive x-rays as a result of the change in the electron's velocity. X-rays are also produced by passing the electron beam through the wiggler. As the bending magnets or the wiggler deflect the path of the electrons, a polychromatic or "white" beam of photons is produced. Due to losses in the synchrotron, the number of electrons passing around the ring decreases over time. The beam half-life is approximately 9.5 hours (<http://camd.lsu.edu/aboutcamd.htm>).

A narrow energy band, nearly monochromatic, of the polychromatic beam can be obtained by passing the photons through a monochromator. The monochromator can be tuned to select a desired energy band. The CAMD tomography beamline uses a double-multilayer monochromator (Oxford Danfysik, UK). The monochromator was calibrated by measuring the photon transmission through various targets with distinct K-edges. The K-edge binding energies of these targets are well-defined, providing a reliable calibration for the monochromator. Figure 28 shows photon absorptivity as a function of energy for several target materials used to calibrate the monochromator. The calibration was performed using two ion chambers located downstream from the target; the measured charge in the ion chamber is related to the absorptivity, which changes as a function of photon energy. The monochromator settings were adjusted to find the discontinuity in the absorptivity that corresponds to the K-edge for each target material.

The manufacturer specifies the accuracy of the monochromator to better than +/- 0.1 keV, which has been confirmed in previous measurements.³² The system has a

selectable energy from 6 keV to 40 keV. All monochromator adjustments in this study were performed by qualified CAMD personnel.

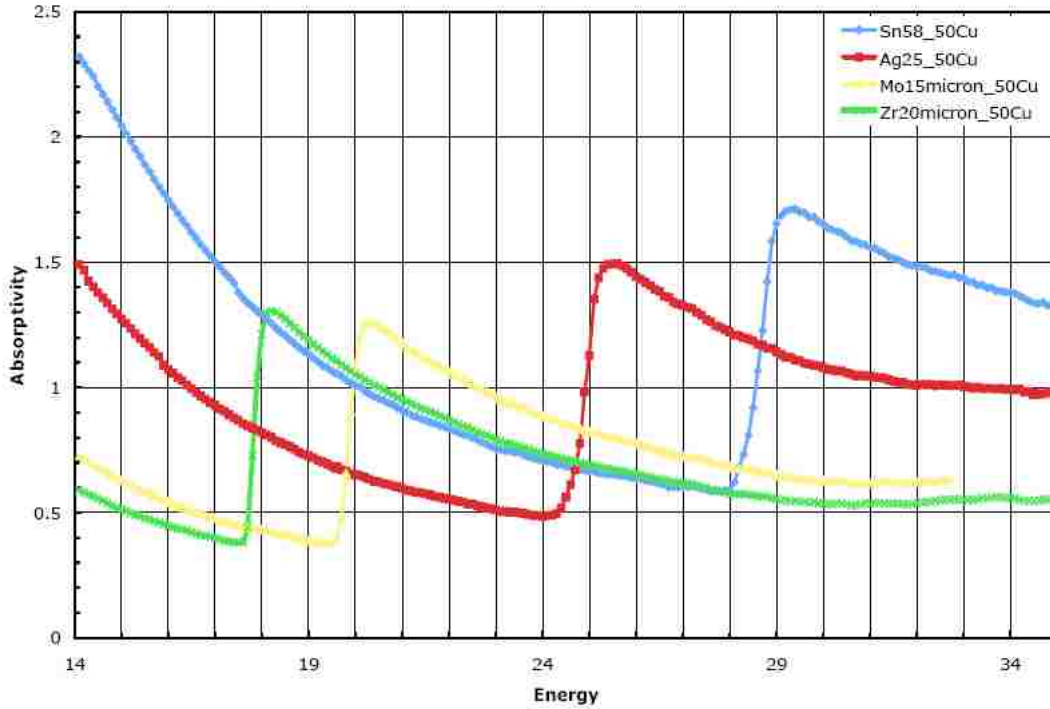


Figure 28: Plot of photon absorption measurements as a function of energy showing the K-edges of several target materials used to calibrate the monochromator on the CAMD tomography beamline (<http://tomo.camd.lsu.edu>).

3.3.2 Tomography Apparatus

Imaging studies on the CAMD tomography beamline were performed inside the experimental hutch. Photons entered the experimental hutch via a Kapton® window (Figure 29). Beamline shutters, located upstream of the Kapton® window, were user controlled via a remote terminal. Restrictions imposed on the beam by the wiggler, monochromator and collimators produce a beam with cross-sectional dimensions of approximately 2.8 cm horizontally \times 0.1 cm vertically.

The monochromatic beam entering the experimental hutch contains a significant fraction of low energy (<10 keV) contamination. The beam passed through 800 μm of aluminum filtration located downstream of the Kapton® window to reduce the low energy contaminants to less than 5% of its original intensity.³² Vertical tungsten collimators were added to eliminate undesirable scattered photons located outside the primary beam (seen in Figure 30). The photon flux downstream of the Kapton® window ranged between 1.1×10^{11} and 3×10^{11} photons $\text{cm}^{-2} \text{sec}^{-1}$ per 100 mA.³³

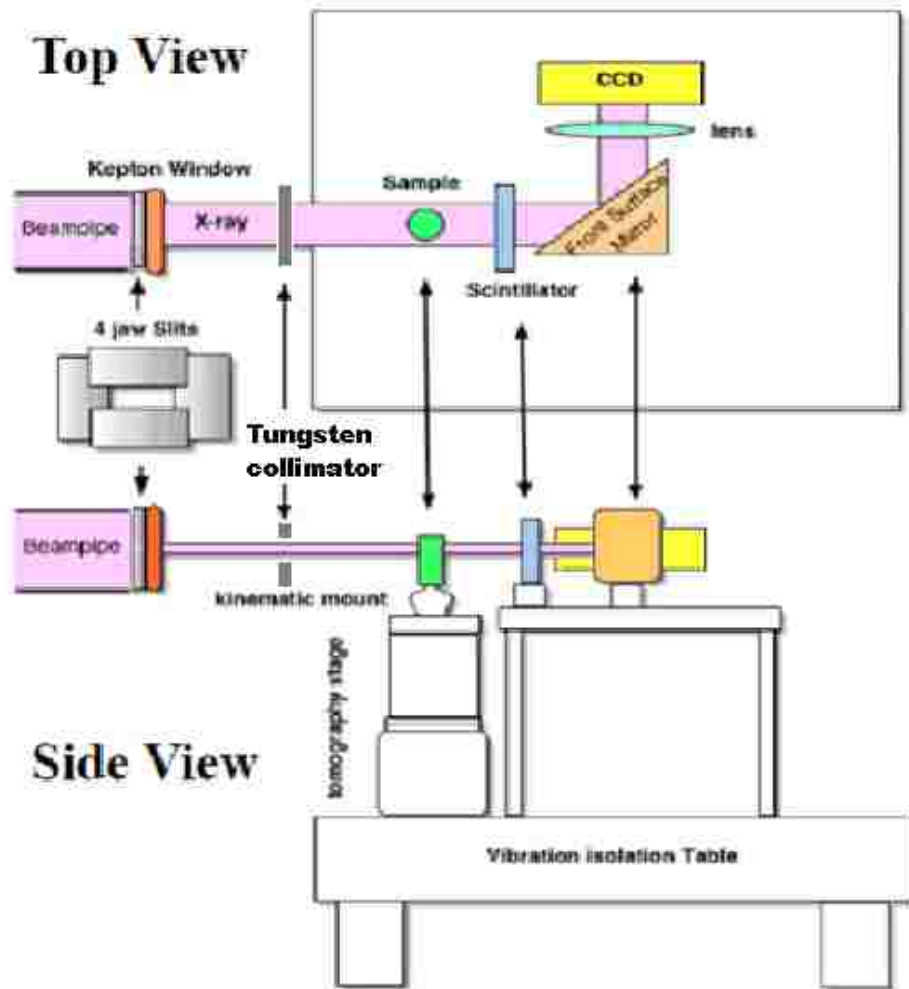


Figure 29: Top and side view of the CAMD tomography apparatus within the experimental hutch. (Drawing not to scale.)

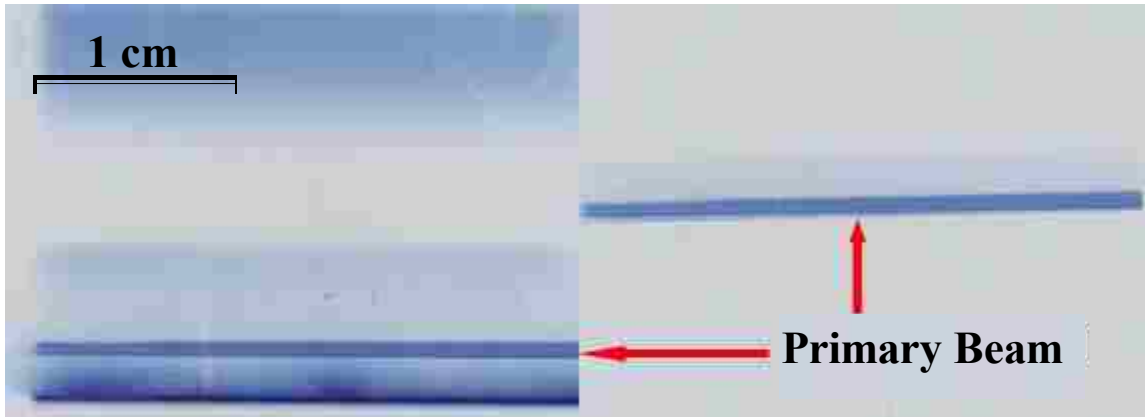


Figure 30: Images of the CAMD x-ray beam acquired with radiochromic film. (Left) Image of the uncollimated beam, showing the primary beam (red arrow) surrounded by secondary radiation coming from the monochromator and other surfaces. (Right) Image of the collimated and filtered beam used for CT imaging.

The tomography bench consisted of a vibration isolation table, sample stage, scintillator, front surface mirror, focusing lens, and CCD camera. The sample stage was servo-operated and provided for stage rotation, elevation, and translation perpendicular to the beam path. The stage was controlled via software developed in Labview by CAMD personnel. Fine control of sample orientation on the stage was performed with analog adjustments to a 4-axis mount on top of the stage. Two axes controlled lateral positioning, while the other two axes controlled tilt. The sample stage positioned the object approximately 6 cm from the scintillator.

The scintillator was a 500 μm thick piece of cerium-activated yttrium aluminum garnet (YAG:Ce). The CCD camera was a Princeton Instruments PIXIS-XO:2KB. The readout was 16 bits per pixel with 2048×512 viewable pixel array. The pixel size was $13.5 \mu\text{m} \times 13.5 \mu\text{m}$. A micro-optic focusing lens projected the light from the scintillator, after reflecting from the mirror, onto the CCD, magnifying the image to an effective pixel

size of $7.42 \mu\text{m} \times 7.42 \mu\text{m}$. The CCD camera was controlled using software developed by CAMD personnel in Labview.

3.3.3 Image Acquisition

Prior to CT acquisitions, the sample was first positioned on the sample stage and secured with modeling compound. To ensure that the sample was properly positioned to fit within the field of view, the beamline shutters were opened and the projection images from the CCD camera were displayed in real time. The sample stage was rotated and the resulting projection images were observed to ensure that the sample indeed fit within the field of view. Any adjustments to the sample position or tilt were performed by first closing the beamline shutters and then manually adjusting the stage. The beamline shutters were reopened and the sample was checked again for proper positioning. In each case, the sample was positioned such that there were at least 60 columns of pixels on either side of the sample for measuring transmission through air.

With the beamline shutters open, projection images from the CCD camera were used to adjust the CCD camera exposure time per projection image. The desired exposure time would produce a maximum pixel value of $\sim 60,000$ in the pixels that measured transmission through air; the CCD would saturate at a pixel value of 65,536 (16 bits max). The exposure times varied between 1 second and 2.5 seconds depending on beam current and beam energy. Lower monochromator energy settings typically resulted in shorter exposure times. Once set, this exposure time was used for all projection images in the data acquisition.

Prior to reconstructing the tomographic images, each projection image had to be converted to represent attenuation, sorted into a sinogram, and corrected for center-of-

rotation error. First each tomography acquisition began by closing the beamline shutters and obtaining five dark field images. The beamline shutters were reopened and three white field images were obtained without any sample object in the field of view. The sample was then moved into position and the projection images were acquired. After each set of 30 projection images, 3 new white field images were obtained; these white field images were used to compensate for changes in the x-ray beam profile as the beam current decayed.

Acquisition time depended on the number of projections and the exposure time per projection. For each acquisition, projections were spaced over 180-degrees with the 0° and 180° projections acquired first. The remaining projection images were then acquired. For all iodine concentration studies, 721 projection images were acquired which corresponded to a projection interval of 0.25° over the 180° range. Total acquisition times ranged from 55 to 75 minutes, which included all white field and dark field images, as well as the mechanical motions of the tomography stage. White field, dark field, and projection images were saved in .SPE file format. The type of image (projection, white field, or dark field) and the projection number and projection angle were recorded in the filename of each image.

3.3.4 Phantom Construction

To perform iodine concentration measurements, a phantom to hold the iodine dilutions was required which would be relatively transparent to photons at the energies used and would fit within the CAMD tomography field of view. To accomplish this, two types of tubing were selected. The first type of tubing was polypropylene (PP) tubing with an average inner diameter of 3 mm and a wall thickness of ~0.2 mm; sections were

cut to a length of 3 cm. The second type of tubing was high density polyethylene (HDPE) tubes. These had an inner diameter of 1.18 mm and a wall thickness of 0.5 mm; sections were cut to a length of 3 cm. The tubes were chosen because they were rigid enough to stand upright without bending.

A base was constructed from PMMA to support the tubes in an upright position. The base was cylindrical and had overall dimensions of 10 mm height and 20 mm diameter. A single hole of 6 mm depth with a 12 mm diameter was milled into the base to hold the tubes. For both types of tubes, modeling compound was used to hold the tubes within the hole of the base. The modeling compound was sufficient to act as a plug for the polypropylene tubes to provide a reservoir for the iodine dilutions. However, the diameter of the HDPE tubes was too large to be plugged consistently with modeling compound, so Critoseal® microhematocrit tube sealing compound was used to plug the HDPE tubes.

When placing the PP tubes in the base, six tubes were loosely arranged in a circle around a central 7th tube. The size of the field of view limited the phantom to this number of PP tubes. Five of the perimeter tubes contained iodine dilutions and the 6th tube contained distilled/deionized water. The center tube, used primarily to provide structure and space the perimeter tubes around the center of the field of view, was left empty. When using the HDPE tubes, 9 or 10 fluid-filled tubes were arranged in a circle around a central empty PP tube, which provided structure and spacing. Phantoms assembled from both types of tubes are shown in Figure 31; and a sample cross-sectional slice of the HDPE tubes filled with iodine concentrations is shown in Figure 32.



Figure 31: Top and side views of the polypropylene (left) and HDPE (right) tubes arranged in the PMMA base for imaging.

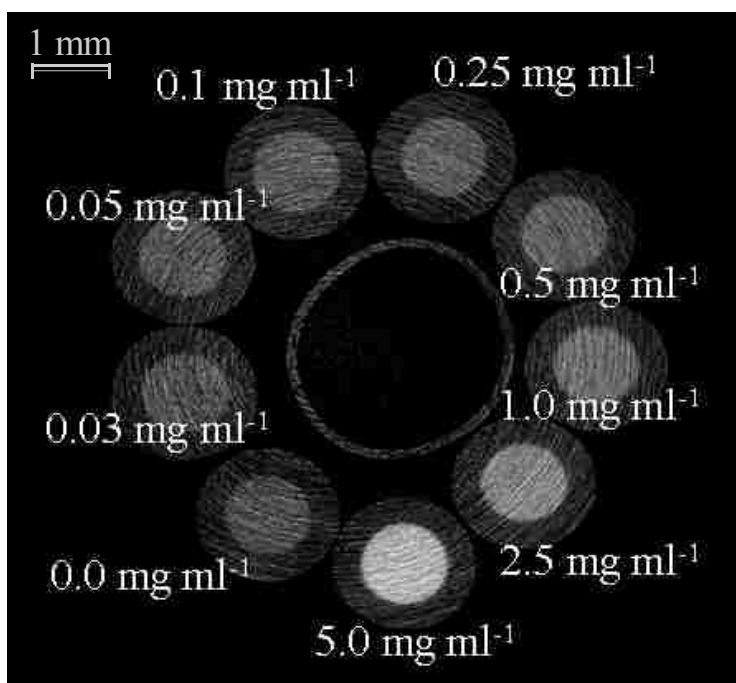


Figure 32: Cross-sectional slice of the HDPE tubes with iodine concentrations surrounding a PP tube.

3.3.5 Image Reconstruction

Image processing and reconstruction were performed using software written in IDL. The images taken were first converted from .SPE format to 32 bit TIFF images to remove the file header. The five dark field images were averaged to obtain a single mean dark field image. Each set of three white field images were averaged together and the mean dark field image was subtracted to obtain a corrected mean white field. The mean white field image was normalized by its mean pixel value.

The dark field image and white field images were used to correct for beam inhomogeneities and pixel-to-pixel response variations. The mean dark field image was subtracted from each projection image to create dark-field corrected projections. Each mean white field image was used to correct the 30 projections that were acquired after the corresponding set of white of field images. The dark field-corrected projections of each set were normalized by dividing by their mean normalized white field. Utilizing white fields acquired every thirty projections compensated for changes in the beam profile over time. While the corrections did not completely eliminate all effects of beam inhomogeneity, scintillator non-uniformity, and CCD pixel variations, it did significantly reduce them (compare Figure 35 and Figure 36 in 3.4.2).

Each pixel value was first converted to total attenuation along the line represented by this pixel. For each projection image, an ROI was selected that spanned the first and last 60 columns of pixels for a total of 120 columns. This ROI size and location was chosen to ensure that the pixels in the ROI only represented transmission through air and not through any part of the object. The mean air pixel value determined from this ROI

was used to calculate (see equation 1-2) on a pixel-by-pixel basis, the total attenuation along the line represented by the pixel.

The projection images, after being converted to attenuation maps, were sorted into sinograms corresponding to each pixel row. The center of rotation for the imaging geometry was determined from the sinograms. This was done by first comparing the 0° projection to a copy of the 180-deg projection that had its columns reversed in order, corresponding to a horizontal flipping of the image. (Note: x-ray beam was assumed parallel based on measured beam divergence by Dugas et al.³³). By definition, the X-rays that comprise these two projections experienced identical paths through the object although traveling in opposite directions. To find the center of rotation, the 180° projection was iteratively shifted by one column and then subtracted from the 0° projection; the square root of the sum of the squares (RSS) of all pixels in the difference image was calculated for each shift. The shift with the lowest RSS was taken to represent twice the distance to the center of rotation, measured from the center of the 0° projection.

Using this calculated center of rotation, each sinogram was reconstructed using FBP. A Ramp-Hann filter (Figure 9) with a cutoff at the Nyquist frequency was used as the reconstruction filter. This filter was chosen because it provided reasonable noise suppression and resulted in the clearest visible distinction between the iodine dilutions and the tubes in which the solutions were contained. The final reconstructed images were saved as TIFF files, with a reconstructed size of 1700×1700 pixels and 120 slices.

The choice to write the FBP program in IDL was due to availability and because it gave greater control over filtering. To confirm that the IDL code used for reconstruction was working as expected, its results were compared to a reconstruction

code provided in MATLAB (The Mathworks, Natick, Massachusetts). To accomplish this, a sample data set of the CAMD concentration phantom containing iodine concentrations of 0.0, 1.0, 2.5, 5.0, 10.0, 25.0 mg ml⁻¹ was reconstructed in both IDL and in MATLAB. The mean value for each concentration was calculated by averaging all pixels within a circular ROI. The data were then fit to a linear model. In IDL, Shepp-Logan and Ramp-Hann filtered (see Figure 9) reconstructions were compared to the MATLAB Shepp-Logan filtered reconstruction.

3.3.6 X-ray Scatter Measurement

The contribution of scattered x-rays to the image was directly measured; an excessive amount of scatter could bias the iodine concentration measurements. One way to express the amount of scatter is as a fraction of the total radiation. This is called the scatter to primary ratio (SPR). A solid cylindrical phantom was constructed with a diameter of 8 mm. A small Pb block was placed upstream of the phantom, strongly attenuating photons through the center of the field of view (Figure 33). Using $\mu_{Pb} = 22.9$ cm⁻¹ (XCOM photon cross-section database), the thickness of Pb required to attenuate 99% of a beam of 33.4 keV photons is 2 mm, so a 2 mm thick \times 1 mm wide \times 4 mm tall Pb block was used.

Only a few transmitted photons and any scattered photons from the periphery of the object should reach the detector in the center of the field of view. The amount of scatter was estimated by comparing the number of photons reaching the detector to the number expected only due to penetration through the Pb block, as measured in a projection image of the PMMA cylinder and Pb block.

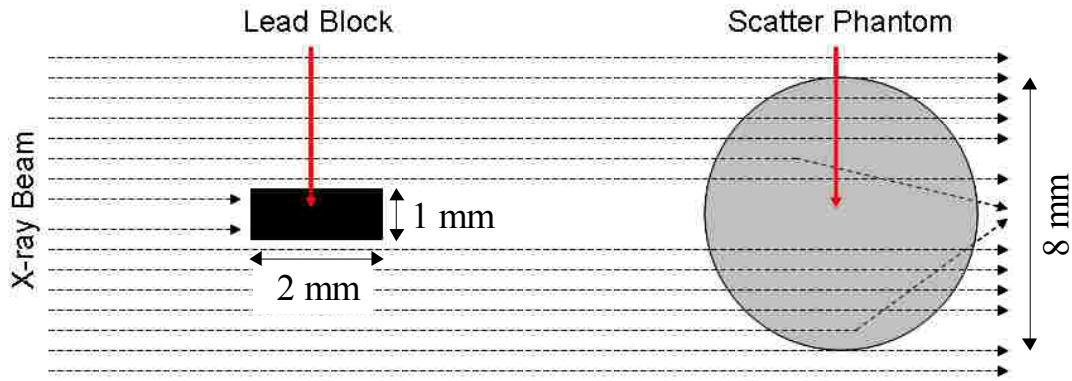


Figure 33: Diagram (top view) illustrating the X-ray scatter contribution measurement. The dashed lines represent X-rays. At the detector, there should be a photon deficiency due to the lead block. Any scattered photons reaching this region would contribute to an increased signal.

3.3.7 Concentration Measurements

The same iodinated contrast solutions used in the Skyscan measurements (see section 2.3.5) were used again in the CAMD concentration studies. As before, the iodine dilutions were 0.0, 0.03, 0.05, 0.1, 0.25, 0.5, and 1.0 mg iodine ml⁻¹, placed in the PP and HDPE tubes. The phantom was imaged at energies bracketing the iodine K-edge of 33.169 keV. In each acquisition, one tube was always filled with distilled-deionized water and the central tube was empty.

Post reconstruction, the data were analyzed similarly to the Skyscan data. ROIs were positioned within each tube with one additional ROI for air placed outside the tubes. The mean pixel values and standard deviations for the air and water ROIs were calculated for each slice, from which the pixel values in the images were scaled to Hounsfield units and were fitted to a linear model with the constraint that the fit line went through the origin. CNR analysis was performed on the resulting data, similarly to that for the SkyScan data. From the data, the 95% confidence and 95% prediction interval was calculated.

3.3.8 K-edge Subtraction Implementation

A K-edge subtraction was performed using the mean ROI data but without converting it to HU. To do this, the attenuation coefficients for air ($\mu_{Air,E}$) and water ($\mu_{H_2O,E}$) were obtained at the corresponding acquisition energy E from the XCOM database. The linear attenuation coefficients were calculated from the mean ROI data for each iodine concentration, which was linearly scaled based on the attenuation coefficients of air and water to obtain

$$\mu_E = \mu_{Air,E} - \left(\overline{ROI}_{n,E} - \overline{ROI}_{Air,E} \right) \frac{(\mu_{H_2O,E} - \mu_{Air,E})}{(\overline{ROI}_{H_2O,E} - \overline{ROI}_{Air,E})} \quad (3-1)$$

where $\overline{ROI}_{n,E}$, $\overline{ROI}_{Air,E}$, and $\overline{ROI}_{H_2O,E}$ are the mean values corresponding to the nth iodine dilution, air, and water respectively acquired at energy E. Details of the K-edge subtraction calculations are given in Appendix A. From the data, the 95% confidence and 95% prediction interval was calculated.

3.3.9 Resolution Measurements

To implement the ASTM E 1695-95 protocol, a resolution phantom was constructed to fit within the CAMD tomography field of view (Figure 34). The phantom was cylindrical and constructed from PMMA. Its dimensions were 10.2 mm diameter and 18 mm height. The phantom was turned down on a lathe from a larger cylinder of extruded PMMA. A 1/4" end mill was used to bore a hole coaxial with the long axis of the phantom, forming a blemish-free PMMA/air interface. The final inside diameter of the hole bored through the resolution phantom was 6.7 mm. A CT acquisition of the CAMD resolution phantom was acquired at 33.62 keV over 180° with a step size of 0.25°.

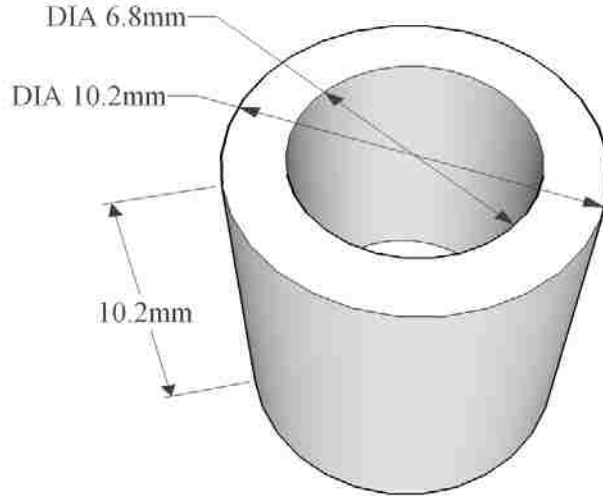


Figure 34: Illustration of the CAMD MTF test phantom used to measure the resolution of the CAMD tomography system.

3.4 Results

3.4.1 Beam Energy Measurements

The beam energy was verified by measurement using the x-ray powder diffraction methodology described by Oves et al. for the CAMD tomography beamline.^{32, 33} The powder diffraction measurement agreed to within 0.12 keV with monochromator settings of 32.5 and 33.5 keV. Details of the measurement and analysis are given in Appendix B.

3.4.2 Reconstruction Algorithm Comparison

An example projection image of 10 HDPE tubes with iodine dilutions prior to any white or dark-field corrections is shown in Figure 35. The same image after these corrections is shown in Figure 36. Results are plotted in Figure 37 to compare MATLAB's built-in FBP algorithm to the IDL reconstruction algorithm routine. The reduced chi-square (χ_v^2) results were used to evaluate the linearity of the reconstruction algorithm. The χ_v^2 results for Shepp-Logan, Ramp-Hann, and MATLAB filters were within 1.7% of each other.

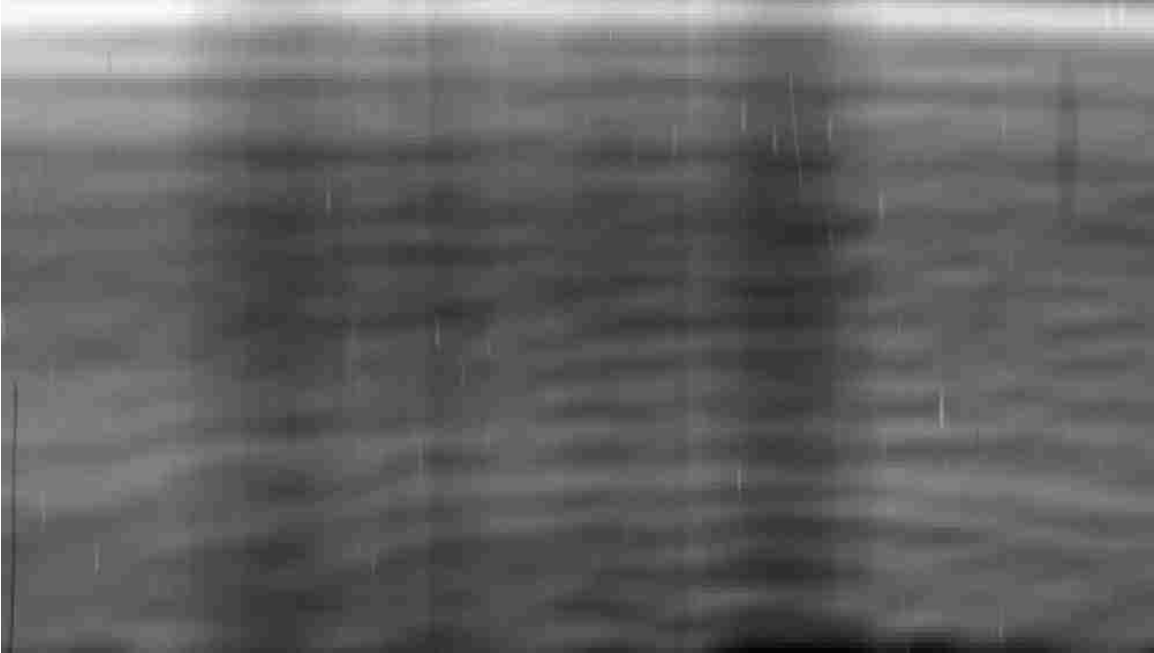


Figure 35: An unprocessed projection image of 10 HDPE tubes arranged in a rough circle around a PP tube. The white spots are and wavy background structure are attributable to impurities in the scintillator and beam inhomogeneities.

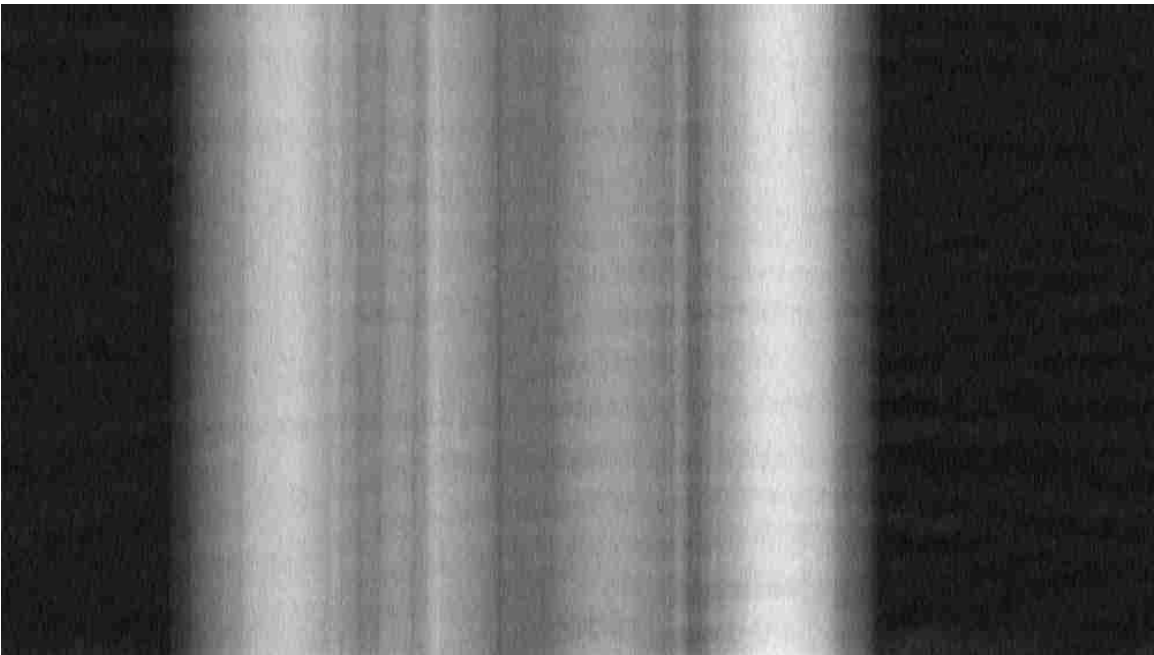


Figure 36: Displayed is the projection image data from Figure 35 after being corrected for the white and dark field effects. The projection image has been converted into total attenuation per pixel.

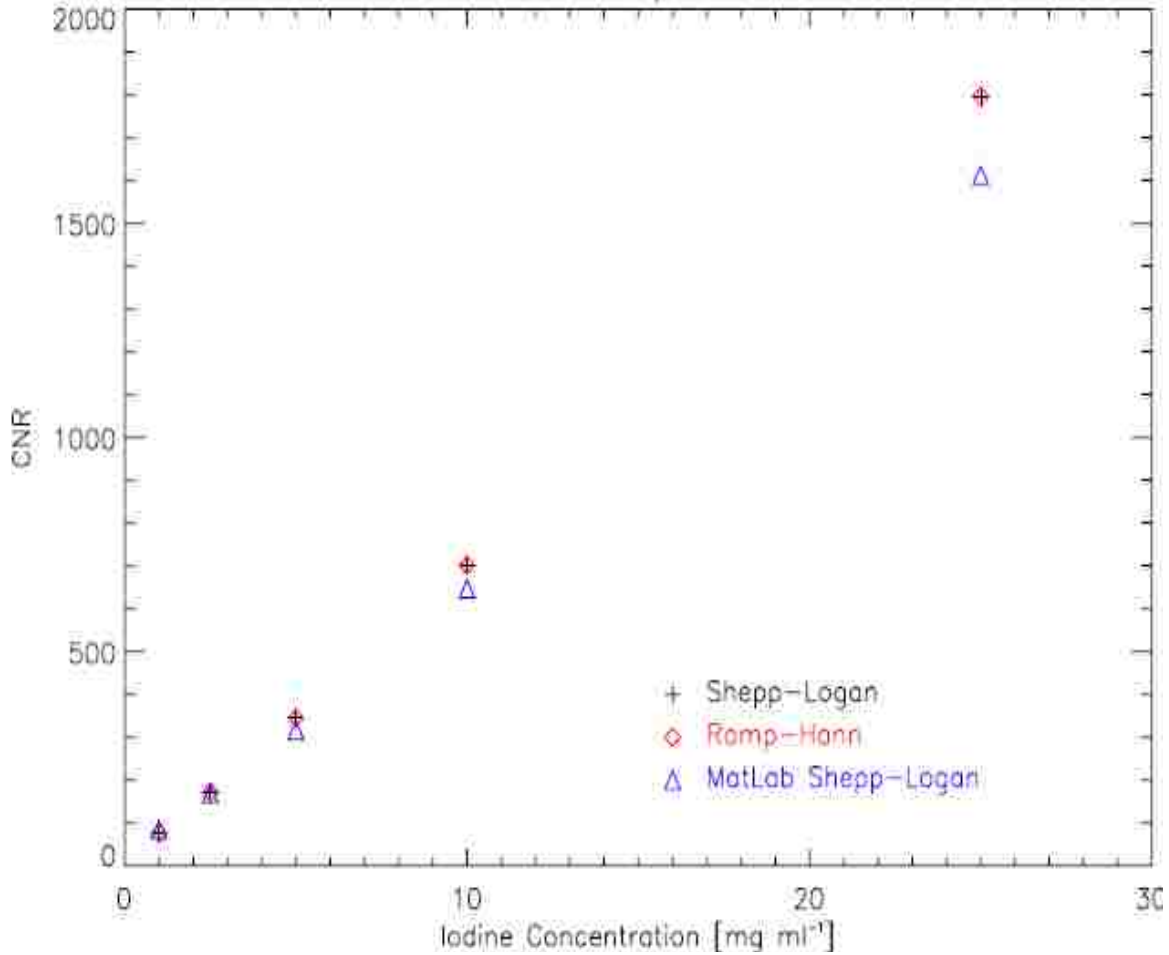


Figure 37: Results from FBP comparison between MATLAB’s reconstruction using a Shepp-Logan filter (Δ) and the in house routine written in IDL using Shepp-Logan (+) and Ramp-Hann filters (◇).

3.4.3 X-ray Scatter Measurement

Figure 38 shows a projection image of the Pb block in front of the PMMA phantom. Figure 39 shows a mean profile calculated from all rows of the projection image. The pixel value at the midpoint of the lead beam block was 568; the calculated pixel value for the same position without the beam block was 20572, so the SPR was 0.0276. This indicates that the scatter contribution is ~2.8% which is negligible as far as the CNR and KES analysis are concerned.

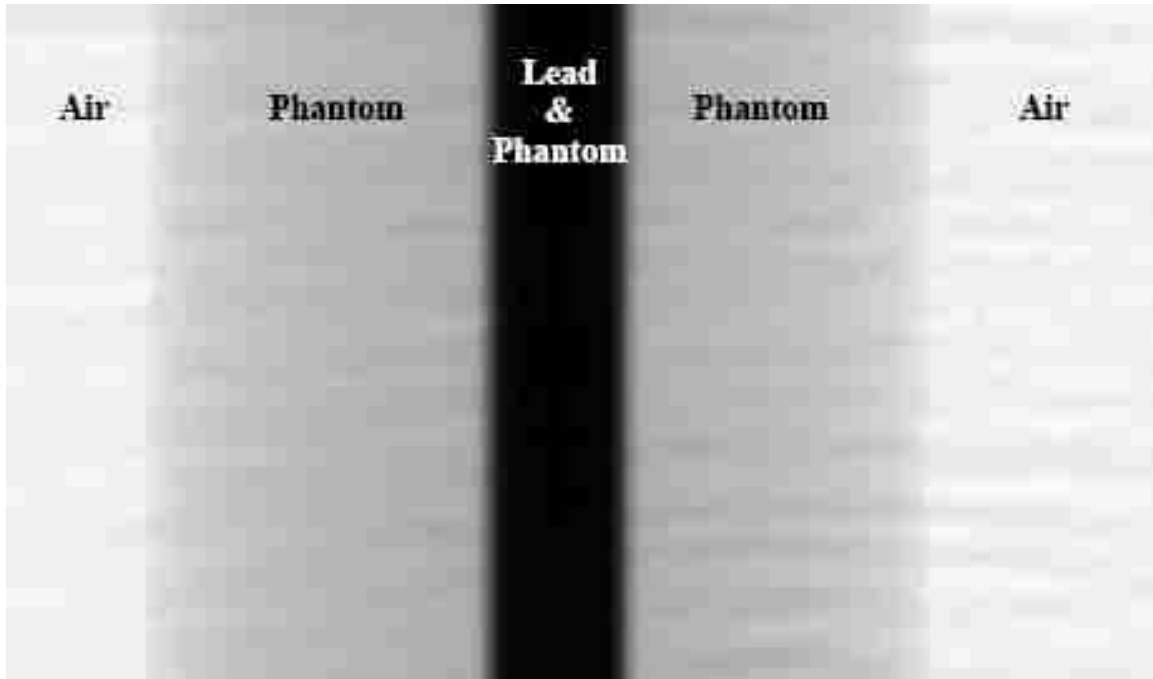


Figure 38: Corrected projection image of scatter phantom with 1 mm wide by 2 mm thick lead beam block.

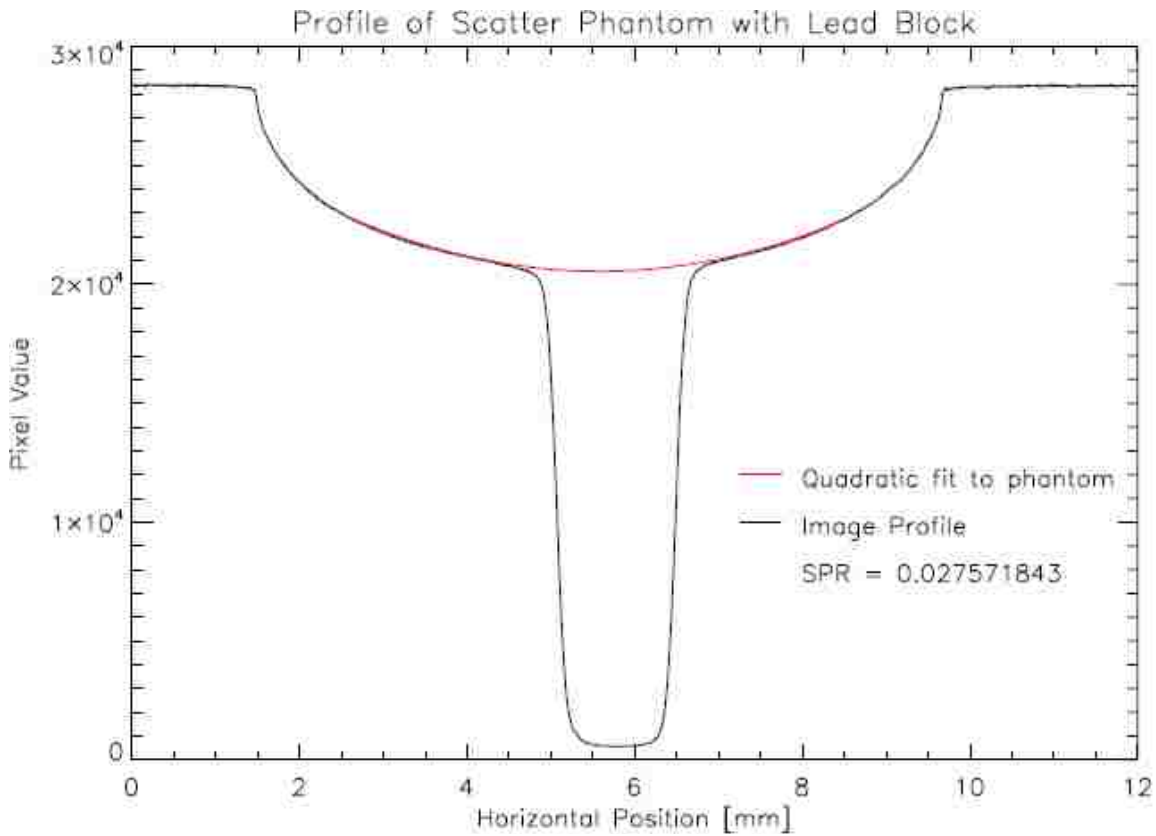


Figure 39: Average profile of scatter phantom and lead beam block. The scatter to primary ratio was calculated to be 0.0276.

3.4.4 Concentration Measurements

The results up to 1 mg ml^{-1} , acquired at a monochromator setting of 32.5 keV , are shown in Figure 40; the slope was $18.1 \pm 3.06 \text{ [HU mg}^{-1}\text{ml]}$, which is represented by a

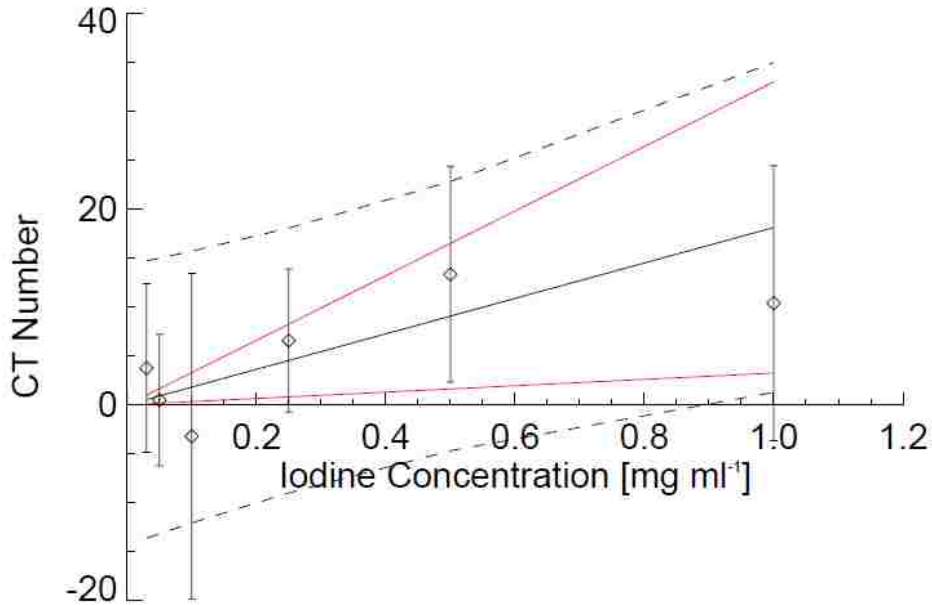


Figure 40: CAMD results plotted in CT number vs. iodine concentration up to 1 mg ml^{-1} for CT acquisition at 32.5 keV . The linear fit (solid black) is constrained to go through the origin ($\chi_v^2 = 0.75$). The solid red and dashed black lines represent the 95% confidence and prediction bands. Error bars represent the standard deviation.

solid black line with $\chi_v^2 = 0.75$ and 5 degrees of freedom. The 95% confidence interval and the 95% prediction interval have been plotted as solid red and dashed black lines respectively. Figure 41 shows the data for concentrations up to 10 mg ml^{-1} . Only a linear fit line (solid) and the 95% prediction interval (dashed) have been displayed. The slope was $18.8 \pm 0.38 \text{ [HU mg}^{-1}\text{ml]}$, which is represented by a solid black line with $\chi_v^2 = 1.20$ and 8 degrees of freedom.

For the data up to 1 mg ml^{-1} concentration acquired at a monochromator setting of 33.5 keV (Figure 42), the slope was $99.84 \pm 4.67 \text{ [HU mg}^{-1}\text{ml]}$, which is represented by a

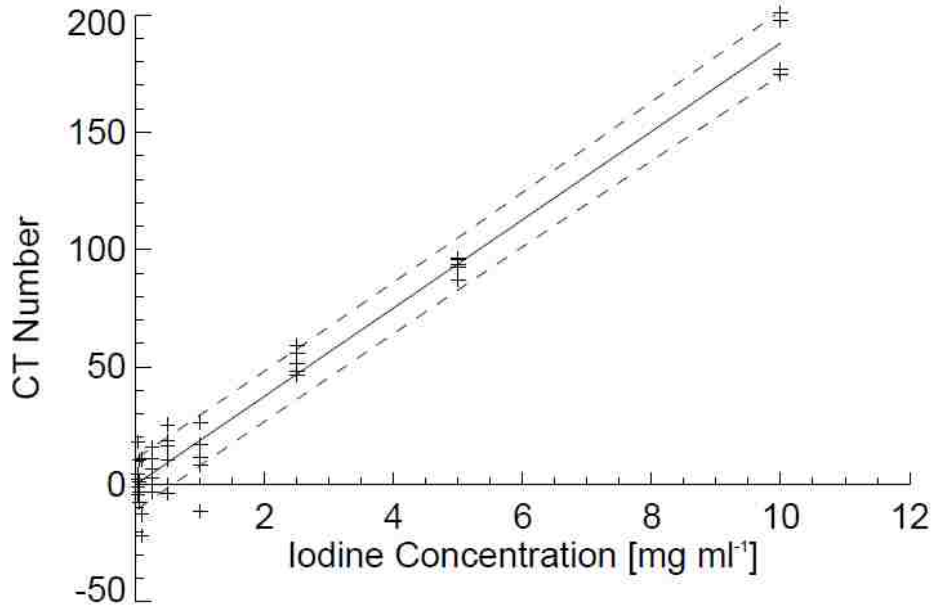


Figure 41: CAMD results plotted in CT number vs. iodine concentration up to 10 mg ml⁻¹ for CT acquisition at 32.5 keV. A linear fit of the data with $\chi_v^2 = 1.20$ (black line), and 95% prediction interval (dashed lines) are shown. The individual data points have been plotted to illustrate the spread in the measurements.

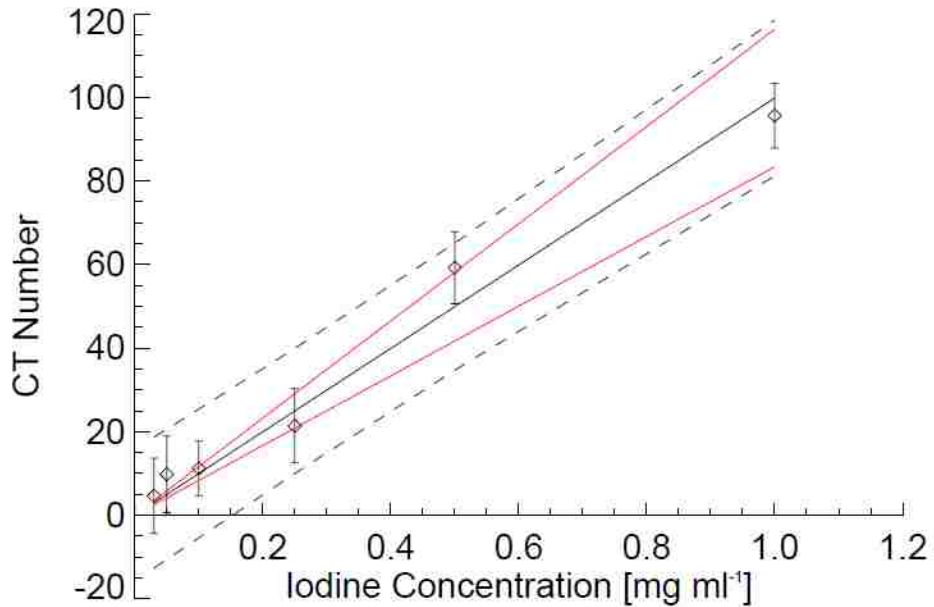


Figure 42: CAMD results plotted in CT number vs. iodine concentration up to 1 mg ml⁻¹ for CT acquisition at 33.5 keV. The linear fit (solid black) is constrained to go through the origin ($\chi_v^2 = 1.97$). The solid red and dashed black lines represent the 95% confidence and prediction bands. Error bars represent the standard deviation.

solid black line with $\chi_v^2 = 1.97$ and 5 degrees of freedom. The 95% confidence interval and the 95% prediction intervals are plotted as solid red and dashed black lines respectively. Figure 43 shows the data for concentrations up to 10 mg ml^{-1} . Only a linear

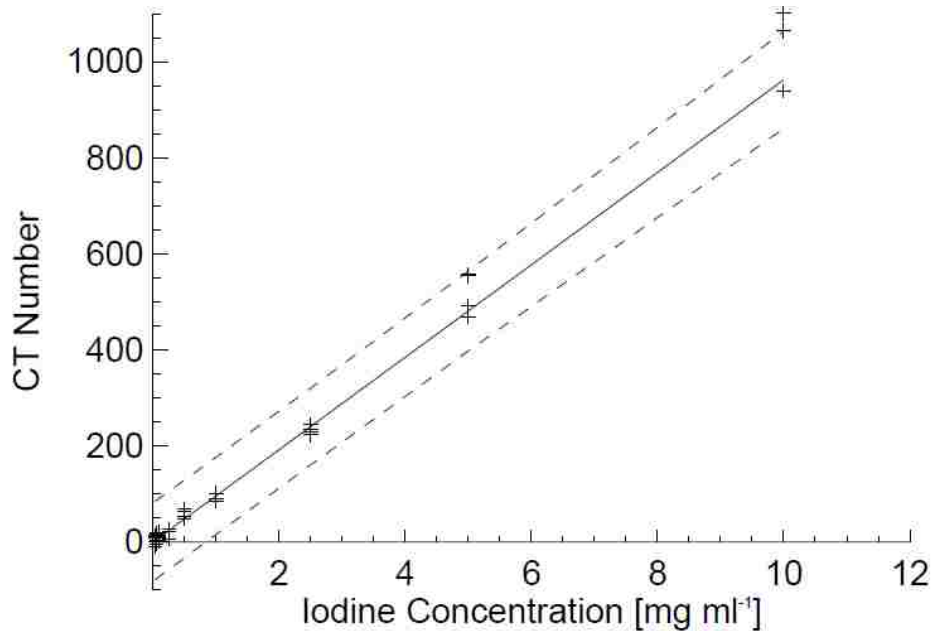


Figure 43: CAMD results plotted in CT number vs. iodine concentration up to 10 mg ml^{-1} for CT acquisition at 33.5 keV. A linear fit of the data with $\chi_v^2 = 3.37$ (black line), and 95% prediction interval (dashed lines) are shown. The individual data points have been plotted to illustrate the spread in the measurements.

fit line (solid) and the 95% prediction interval (dashed) have been displayed. The slope was $103.8 \pm 0.98 \text{ [HU mg}^{-1}\text{ml]}$, which is represented by a solid black line with $\chi_v^2 = 3.37$ and 8 degrees of freedom.

The results for the HU calculations and the CNR evaluation are compiled in Table 4 and Table 5. The mean value for each concentration and the corresponding standard deviation has been included. The standard deviation was calculated from the spread in the data in HU. The standard error was also calculated by propagation of errors from the initial uncertainty in each ROI. The average standard error for any iodine concentration

using this method was approximately 0.25 HU, regardless of energy. This value is significantly smaller than the standard error calculated from the spread in the measurements (average of 9.64 HU and 19.19 HU for 32.5 keV and 33.5 keV respectively), which does not adequately represent the results. The lowest measured concentration of iodine that produced a CNR of 3 or higher was 1.0 mg ml⁻¹ and 0.1 mg ml⁻¹ of iodine for 32.5 keV and 33.5 keV respectively.

Table 4: Results from CAMD measurements at a monochromator setting of 32.5. Empty spaces indicate missing or corrupted data.

I [mg ml ⁻¹]	Mean pixel value from ROI [HU] ^a					Mean HU	Std Dev ^b	Std Err ^b	CNR
	Acq 1	Acq 2	Acq 3	Acq 4	Acq 5				
0.03	4.18	-1.32	2.30	-4.39	17.96	3.74	8.61	3.85	0.97
0.05	-3.09	1.18	1.37	-7.56	10.56	0.49	6.71	3.00	0.16
0.1	10.72	10.95	-12.78	-21.78		-3.22	16.64	8.32	0.39
0.25	-3.25	6.52	2.76	11.19	15.61	6.56	7.31	3.27	2.01
0.5	18.47	10.44	25.42	-3.91	16.19	13.32	11.03	4.93	2.70
1	8.24	26.47	11.52	17.11	-11.46	10.37	14.03	6.27	3.97
2.5	51.47	48.34	55.74	46.75	58.95	52.25	5.08	2.27	23.00
5	87.05	96.27	93.82	95.55	92.34	93.01	3.67	1.64	56.73
10	197.66	174.62	176.56	200.72		187.39	13.70	6.85	27.35

^a The standard error of each mean ROI value is not shown.

^b The standard deviation and standard error represent the uncertainty based on the repeat measurements of the pixel values' mean.

Table 5: Results from CAMD measurements at a monochromator setting of 33.5. Empty spaces indicate missing or corrupted data.

I [mg ml ⁻¹]	Mean pixel value from ROI [HU] ^a					Mean HU	Std Dev ^b	Std Err ^b	CNR
	Acq 1	Acq 2	Acq 3	Acq 4	Acq 5				
0.03	0.94	8.36	12.50	-9.40	10.89	4.66	9.02	4.03	1.15
0.05	-3.71	4.47	14.67	15.54	18.08	9.81	9.16	4.10	2.39
0.1	2.44	7.99	12.47	13.24	19.93	11.22	6.50	2.91	3.86
0.25	22.28	26.68	5.81	26.57	25.66	21.40	8.90	3.98	5.38
0.5	48.43	52.05	68.85	64.12	62.75	59.24	8.62	3.85	15.37
1	84.61	101.58	101.28	90.30	100.50	95.65	7.76	3.47	27.57
2.5	223.03	230.35	225.16	233.88	244.70	231.42	8.56	3.83	60.43
5	467.76	491.22	557.89	557.91	554.09	525.77	43.09	19.27	27.29
10	938.66	1100.50	1063.99	1065.98		1042.28	71.09	35.54	29.32

^a The standard error of each mean ROI value is not shown.

^b The standard deviation and standard error represent the uncertainty based on the repeat measurements of the pixel values' mean.

3.4.5 K-edge Subtraction

The KES results are plotted in Figure 44. Using a linear fit constrained to go through the origin, the slope from a fit of the data up to an iodine concentration of

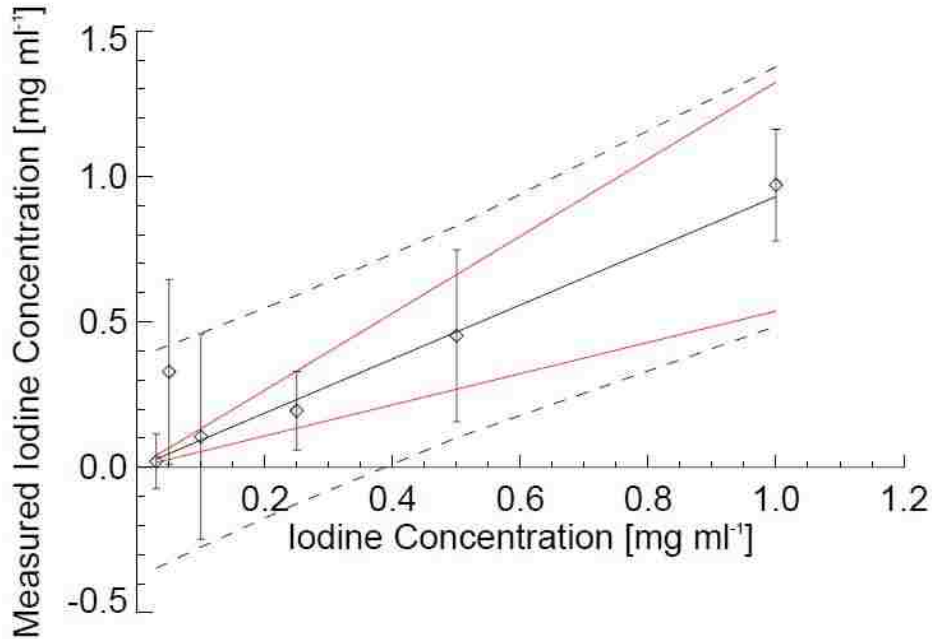


Figure 44: CAMD results plotted in CT number vs. iodine concentration up to 1 mg ml^{-1} for KES. The linear fit (solid black) is constrained to go through the origin ($\chi_v^2 = 0.92$). The solid red and dashed black lines represent the 95% confidence and prediction bands. Error bars represent the standard deviation.

1 mg ml^{-1} is 0.93 ± 0.05 with $\chi_v^2 = 0.92$ and 5 degrees of freedom. The theoretical model is a line going through the origin with a slope of 1. The 95% confidence interval (solid red) and 95% prediction interval (dashed black) are included. Error bars represent the standard deviation. Figure 45 shows a fit of the data up to an iodine concentration of 10 mg ml^{-1} with a slope of 0.98 ± 0.01 with $\chi_v^2 = 3.07$ and 8 degrees of freedom.

The KES results and the corresponding CNR values are compiled in Table 6. The mean measured value for each iodine concentration and the corresponding standard deviation are included. The standard deviation in mg ml^{-1} was calculated from the spread

in the data. The standard error was also calculated by propagation of errors from the initial uncertainty in each ROI. The average standard error for any iodine concentration using this method was approximately $0.0042 \text{ mg ml}^{-1}$. Again, this value is significantly

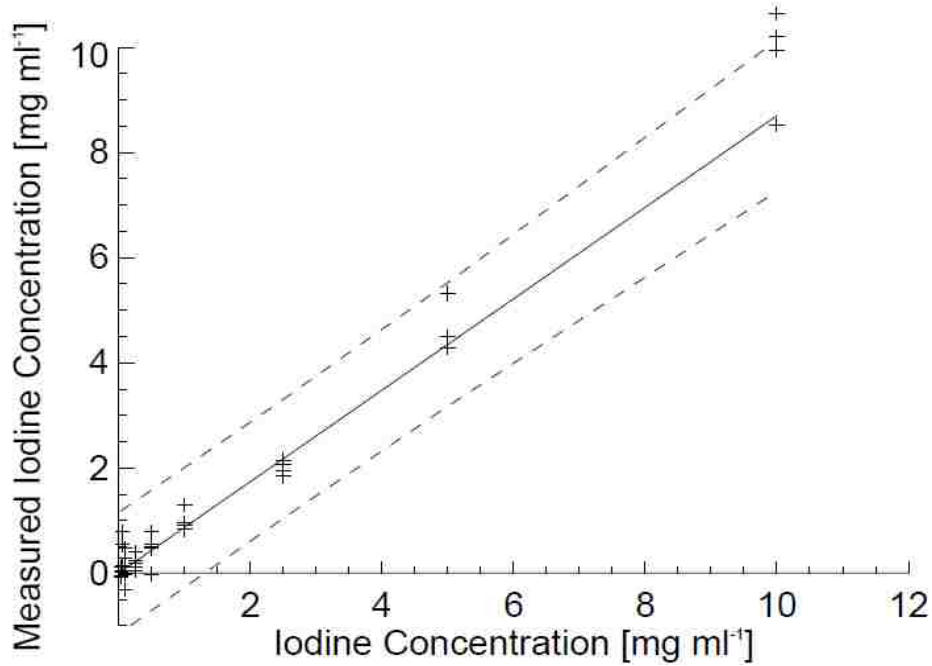


Figure 45: CAMD results plotted in CT number vs. iodine concentration up to 10 mg ml^{-1} for KES. A linear fit of the data with $\chi_v^2 = 3.07$ (black line), and 95% prediction interval (dashed lines) are shown. The individual data points have been plotted to illustrate the spread in the measurements.

Table 6: Results from the CAMD KES.

I [mg ml^{-1}]	Mean pixel value from ROI [HU] ^a					Mean HU	Std Dev ^b	Std Err ^b	CNR
	Acq 1	Acq 2	Acq 3	Acq 4	Acq 5				
0.03	0.12	-0.06	-0.08	0.11	0.01	0.02	0.09	0.04	0.50
0.05	0.15	0.78	0.54	0.04	0.13	0.33	0.32	0.14	2.30
0.1	0.29	0.48	-0.03	-0.32		0.10	0.35	0.18	0.58
0.25	0.04	0.18	0.12	0.23	0.40	0.19	0.14	0.06	3.11
0.5	0.50	0.78	0.54	0.47	-0.03	0.45	0.29	0.13	3.43
1	1.30	0.91	0.96	0.85	0.83	0.97	0.20	0.09	10.86
2.5	1.95	2.15	2.13	2.07	1.84	2.03	0.13	0.06	34.11
5	5.33	5.31	5.31	4.49	4.28	4.94	0.51	0.23	21.47
10	10.64	10.20	9.94	8.52		9.82	0.92	0.46	21.44

^a The standard error of each mean ROI value is not shown.

^b The standard deviation and standard error represent the uncertainty based on the repeat measurements of the pixel values' mean.

smaller than the standard error calculated from the spread in the measurements (average of 0.143 mg ml^{-1}) and does not adequately represent the results. The lowest measured concentration of iodine that produced a CNR of 3 or higher was 0.25 mg ml^{-1} .

3.4.6 Resolution Measurements

A sample CT slice of the CAMD MTF phantom is shown in Figure 46. Using the MTF test phantom constructed for the CAMD system, the MTF measured at 10% of the maximum the response was 56 lp mm^{-1} . The results of the MTF measurements are displayed in Figure 47.

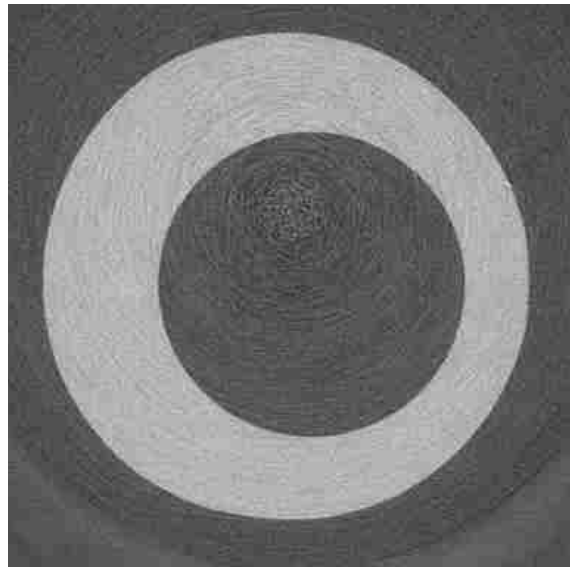


Figure 46: CT image of the CAMD MTF test phantom. A Ram-Lak filter with a cut-off at the Nyquist frequency was used during reconstruction.

3.5 Discussion

3.5.1 Energy Measurements

There was an average discrepancy of 0.1 keV between the X-ray powder diffraction measurements and the monochromator setting. This is consistent with previous studies using X-ray powder diffraction to measure the tomography beamline

energy at CAMD.³² This discrepancy was sufficiently small that the monochromator setting was used as the beam energy for calculations in subsequent sections.

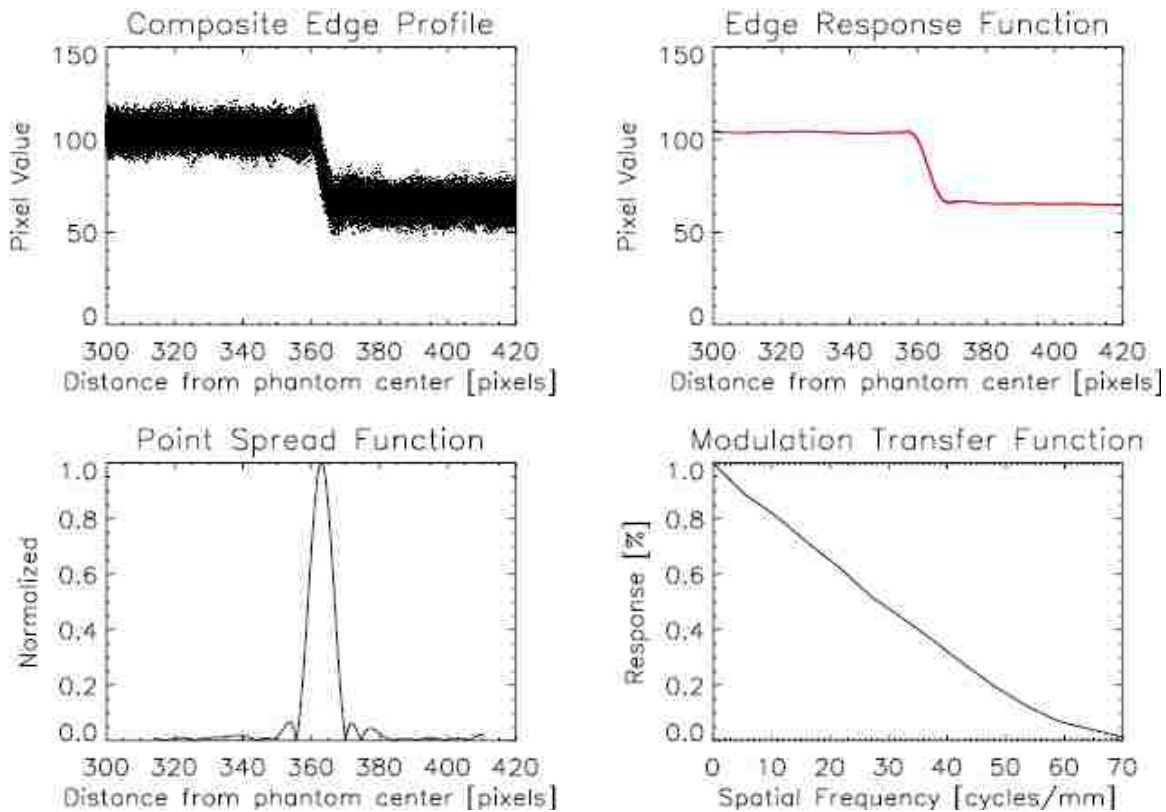


Figure 47: The composite edge profile is shown in the top left which is smoothed to obtain the ERF (top right). The analytical derivative of the ERF is used smoothed to produce the PSF (bottom left). The Fourier transform of the PSF is the MTF (bottom right) for the CAMD tomography system. The spatial frequency of the MTF measured at 10% of the maximum was found to be 56 lp mm⁻¹.

3.5.2 Reconstruction Algorithm Comparison

Results from the reconstruction routine written in IDL were found to agree well with those from MATLAB's built in inverse Radon transform function when compared based on their CNR values. A comparison of the reduced chi-square (χ_v^2) results for the IDL and MATLAB routines showed a difference of less than 0.2% when comparing the Shepp-Logan filters. The reconstruction routine written in IDL was considered to be

acceptable for use in CT reconstruction. However, there was significant ring artifacts present in the CT images for both the IDL and MATLAB routines. The implementation of a ring artifact suppression/correction technique may help to reduce structured noise.

3.5.3 X-ray Scatter Measurement

The SPR was determined to evaluate the impact of scatter in the uncollimated projection images. The motivation for this was to determine whether a correction was required to compensate for the effects of scatter. A measured SPR of < 3% was found. The SPR can exceed values of 50% in uncollimated clinical CT systems. A high degree of scatter reduces image contrast.³⁴ The relatively low amount of scatter present in the CAMD tomography system was considered acceptable.

3.5.4 Concentration Measurements

Results indicated that CAMD images at a monochromator setting of 33.5 keV may be capable of imaging 0.06 mg ml⁻¹ of iodine; the concentration of 0.1 mg ml⁻¹ was distinguishable from water at a CNR of 3.86 while the concentration at 0.05 mg ml⁻¹ was not, which suggests that the lower limit lies between 0.05 mg ml⁻¹ and 0.1 mg ml⁻¹. However, the lowest measured iodine concentration with a CNR greater than 3 at a monochromator setting of 32.5 keV was 1.0 mg ml⁻¹ with a CNR of 3.97. Furthermore, this suggests that it may be possible to image cells labeled with IUdR but the relatively large uncertainty in the calculated iodine concentration based on a single measurement will render dosimetric calculations from a treatment planning system unreliable. Including additional iodine concentrations may help to improve statistics at lower concentrations and better define the lower limit of detection.

3.5.5 K-edge Subtraction

From the KES results, the lowest iodine concentration with a CNR of 3 was 0.25 mg ml⁻¹ with CNR = 3.11. A large relative standard deviation in the measurements at lower concentrations significantly affected the results in this region, compromising the ability to discern the lower limit of detection. Previous KES studies involving other synchrotron based microCT systems have measured iodine concentrations as low as 0.185 mg ml⁻¹ with a CNR of 3.²¹ This suggests that it may be possible to improve our lower limit of detection using KES.

3.5.6 Resolution Measurements

The MTF was effectively measured using the ASTM E 1695-95 protocol. The response of the MTF at 10% occurs at 56 lp mm⁻¹ which significantly outperforms the Skyscan-1074 with a response at 10% of 5.5 lp mm⁻¹. With the CAMD system there is approximately 18 μm lp⁻¹, which means each line, at 9 μm wide, is visualized. CAMD's resolution is pixel-size limited; unlike SkyScan where the pixel size is not the limiting factor (it's the focal spot size). Clinical implementation may not require such high spatial resolution. It may be more valuable to trade some spatial resolution for decreased noise and dose to improve the lower limit of detectability.

Chapter 4. Aim 3, In Vitro Imaging Study

Image IUdR-labeled CHO cells.

4.1 Goal

To use microCT to image IUdR-labeled CHO cells and use the tomographic image data to quantify the IUdR uptake in vitro.

4.2 Analytical Approach

Thymidine replacement was achieved by growing the cells in IUdR and was verified by a radioiodine assay. CT images were then obtained. The results were compared to the HU calibration curve produced in Specific Aim 2 and KES analysis was also applied to determine absolute iodine concentration, which was compared to expected IUdR replacement.

4.3 Materials and Methods

4.3.1 Chinese Hamster Ovary Cells

In this study, CHO cells were used concurrently in a study at Louisiana State University and CAMD to verify uptake of IUdR in an attempt to determine the efficacy of X-ray activated Auger electron radiotherapy. The specific cell line used was CHO-K1. This cell line was derived as a subclone from the parental CHO line that originated from the biopsy of an adult Chinese hamster's ovary in 1957.³⁵

4.3.2 Cell Culturing and Preparation

Cell culturing was performed in the cell culture lab located at LSU Pennington Biomedical Research Center in Baton Rouge, LA. The CHO cells were cultured as a monolayer in Ham's F12 medium supplemented with 10% fetal bovine serum. They were incubated at 37° C in a 5% CO₂ atmosphere. The cell doubling rate was roughly 14±0.8

hours. The cells were seeded at a density of 10^5 cells per 25 cm^2 in a T25 flask (25 cm^2 Cell Culture Flask, BD Falcon). After 24 hours incubation, IUdR (obtained from Sigma-Aldrich) was added at a final concentration of $20\text{ }\mu\text{M}$ to a portion of the cells. The cells were returned to incubate for another 24 hours after which, all cells were harvested. After pouring off the medium, the cells were washed with trypsin for 1 minute. Additional medium was then added to arrest the trypsinization process and suspend the cells. The resulting cell suspension was then collected.

To more closely approximate tissue and to improve quantification through CT imaging, the cells were centrifuged in several stages into a semi-solid pellet. First, the cell suspension was centrifuged for 2 minutes at 10,000 rpm in a 1.5 ml PP microcentrifuge tube. The separated medium was poured off and the cell pellet was resuspended in 5 ml of phosphate buffered saline (PBS). After a second cycle of centrifuging, the PBS was poured off and $250\text{ }\mu\text{L}$ of PBS was added to moisten the pellet. Each cell pellet was imaged in the microcentrifuge tube.

To obtain a pellet volume of $\sim 300\text{ }\mu\text{l}$ of cells labeled with IUdR, the cells from four T25 flasks were combined. The need for four flasks was due to the inherent toxicity of IUdR. For cells without IUdR, only one T25 flask was necessary. To determine the cell density of the pellets, $10\text{ }\mu\text{l}$ of the pellet was removed and added to $900\text{ }\mu\text{l}$ PBS and re-suspended. This suspension was then counted using a hemocytometer.

To verify the uptake of IUdR by the CHO cells, a radioisotope assay technique was employed which involved the use of ^{125}I labeled IUdR (^{125}I -IUdR); this assay was being performed concurrently by others within the same research group at LSU's Department of Physics and Astronomy working on the X-ray activated Auger electron

radiotherapy project. This group performed the radioiodine assay, with the results reported here. The technique involved the incorporation of the radiolabeled ^{125}I -IUdR into the CHO cell DNA followed by DNA extraction and assay. To do this, the cells were plated and grown in monolayers in tube flasks at Pennington Biomedical Research Center cell culture lab before being moved to LSU's Nuclear Science Building cell culture lab. The IUdR, to be added to the growth medium, was made from 134 μl of cold 15 mM IUdR + 9 μl of hot 15 mM (IUdR + ^{125}I -IUdR) in 57 μl 0.1 N NaOH. This was mixed well before 30 μl per 5 ml of 20 μM IUdR concentration was added to the medium overlay. The cells were given ~24 hours growth before they were rinsed twice with 5 ml PBS and drained well.

The process of DNA isolation followed Promega Wizard[®] Genomic DNA Purification Kit (Madison, WI) protocol. Following those guidelines, to each flask 600 μl nuclei lysis solution was added to break cytoplasmic and nuclear membranes. The RNA was digested with an RNase enzyme to eliminate any potential RNA contamination. The DNA was then precipitated out of the solution using isopropanol. The DNA was washed and the pellet was re-hydrated. This procedure yielded 100-200 μl rehydrated DNA solution. The DNA was counted in a Packard Cobra II Auto-gamma counter to determine the amount of IUdR present. The samples were then measured using a spectrophotometer to determine the mass of DNA per ml of solution. The absorbance was measured at 260 nm and again at 280 nm to determine DNA mass per ml and purity.

The CHO cells with and without IUdR were imaged at energies 33.5 keV and 32.5 keV to bracket the iodine K-shell binding energy. The fit parameters obtained from the averaged HU data in section 3.4.4 were used to determine the most probable iodine

concentration based on the cell data. To do this, an iodine concentration (in mg ml^{-1}) was obtained for the average cell ROI value from the appropriate HU calibration curve according to acquisition energy. The HU value for cells without IUdR was subtracted from that of cells with IUdR to obtain a difference in HU. An iodine concentration was determined for cells with IUdR based on the difference in HU using the HU calibration curves and the 95% prediction intervals were used for the corresponding energy to determine the range of iodine concentrations which could have produced the given HU measurement. A KES analysis was also performed to directly quantify the iodine concentration. The KES calibration curve was used to determine the corrected iodine concentration. The 95% prediction interval was used to obtain the range of possible iodine concentrations that could have produced the given measurement.

4.3.3 Phantom

To mechanically support the microcentrifuge tube and an HDPE tube containing water during image acquisition, a phantom was constructed from PMMA. The phantom was designed to fit within the field of view of the CAMD tomography system. The cell phantom was made with two holes in it. One hole held the microcentrifuge tube and was terraced to support the microcentrifuge tube. The second hole held the water-filled HDPE tube. The phantom is illustrated in Figure 48 and a sample CT slice is shown in Figure 49.

4.3.4 Surface Dose Estimate

An estimate of the surface dose, defined as the energy deposited per unit mass, delivered as a result of one 360° monochromatic CT scan using the CAMD system was calculated using equation 4-1. where D_{tomo} is the dose in Gy [Joule kg^{-1}], m is the total

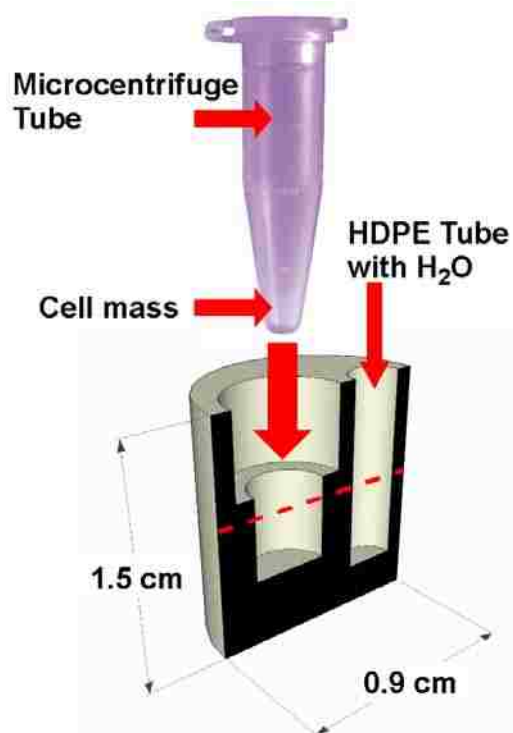


Figure 48: Cutaway view of the PMMA base used to mechanically support the microcentrifuge tube and the HDPE tube containing water. The red dashed line indicates the approximate beam path through the cell mass in the bottom of the microcentrifuge tube.

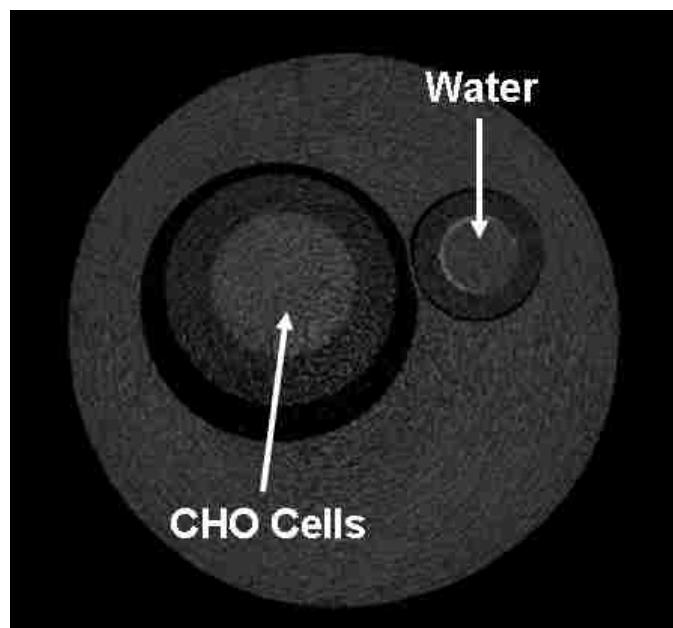


Figure 49: A typical CT image acquired at 33.5 keV of the PMMA base, the CHO cell tube containing IuDR-labeled cells and the HDPE tube filled with distilled/deionized water.

$$D_{\text{tomo}} = 1000 \frac{m N_0}{w h} E_\gamma \left(\frac{\mu_{\text{en}}}{\rho} \right)_{M_1, E_\gamma} \left[\frac{1}{2} + \frac{1}{2\pi} \int_{-\frac{\pi}{2}}^{\frac{\pi}{2}} \exp(-\bar{\mu}_{E_\gamma} D_p \cos(\theta)) d\theta \right] \quad (4-1)$$

number of projections, N_0 is the mean number of photons per pixel per projection, w is the pixel width in cm, h is the beam height in cm, D_p is the phantom diameter in cm, $(\mu_{\text{en}}/\rho)_{M_1, E_\gamma}$ and $\bar{\mu}_{E_\gamma}$ are the mass energy absorption coefficient for material M_1 [$\text{cm}^2 \text{g}^{-1}$] and the linear attenuation coefficient [cm^{-1}] at energy E_γ respectively.²¹ The mass energy absorption coefficient of $0.079 \text{ cm}^2 \text{ g}^{-1}$ and the linear attenuation coefficient of 0.328 cm^{-1} were used for the phantom material PMMA.¹⁷ The average estimated surface dose delivered to the cell phantom for a 360° acquisition was determined to be 373 Gy. Actual CAMD acquisitions were only capable of 180° scans which would reduce the surface dose delivered. Detector quantum efficiency was not considered. There is a tradeoff between the pixel size which governs resolution and the dose.

4.4 Results

4.4.1 Cell Density Assay

Table 7 shows the results from the hemocytometry measurements. The cell density for the control was 2.4×10^7 cells per ml. Cells grown in $20 \mu\text{M}$ IUdR had a cell density of 2.25×10^7 cells per ml for a total volume of $320 \mu\text{l}$. By comparison, the density of breast cancer is 1.07×10^9 cells per ml. This lower cell density in turn lowered the iodine concentration for DNA-incorporated iodine in the cell mass from the expected value of 0.06 mg ml^{-1} to 0.001 mg ml^{-1} .

Table 7: Results from hemocytometry measurements of cell density. Each cell per grid square corresponds to 10^6 cells per ml in suspension. Three squares were added to obtain the cell count.

IUdR [μ M]	Cell Count	Cell Density [ml^{-1}]
0	72.25	2.40E+07
20	67.50	2.25E+07

4.4.2 IUdR Uptake Assay

The IUdR uptake using 20 μ M solution was determined to be $17.4\% \pm 3.6\%$ standard deviation and $\pm 0.8\%$ standard error over 20 trials.

4.4.3 IUdR Replacement Measurements

For images made at the monochromator setting of 32.5 keV, cells containing IUdR measured 68.6 ± 1.7 HU while cells without IUdR measured 69.2 ± 0.7 HU. The difference in the two values is -0.6 ± 1.8 HU. Because this difference in HU value is less than one standard deviation, the two values are not considered statistically different. The cells containing IUdR measured -0.04 ± 0.10 mg ml^{-1} of iodine from the calibration curve in section 3.4.4.

For the images made at a monochromator setting of 33.5 keV, cells containing IUdR measured 84.8 ± 1.3 HU while cells without IUdR measured 64.6 ± 4.2 HU. The average difference between cells with and without IUdR was 20.2 ± 4.4 HU. The difference in HU value is greater than four standard deviations and is considered statistically different. The range of possible iodine concentrations which could produce this HU difference is ± 0.15 mg ml^{-1} based on 95% confidence. Using the calibration curve from section 3.4.4, the difference in HU equates to a measured iodine concentration of 0.21 ± 0.04 mg ml^{-1} . This significantly exceeds the 0.001 mg ml^{-1} of iodine incorporated in DNA.

Similarly, a KES of the CHO cells without IUdR yielded an iodine concentration of $-0.052 \pm 0.046 \text{ mg ml}^{-1}$. Cells with IUdR measured $0.186 \pm 0.010 \text{ mg ml}^{-1}$. The range of possible iodine concentrations which could produce this measurement is $\pm 0.18 \text{ mg ml}^{-1}$ based on 95% confidence. Based on the KES calibration the iodine concentration is $0.20 \pm 0.01 \text{ mg ml}^{-1}$. A K-edge subtraction image of CHO cells containing IUdR is displayed in Figure 50.

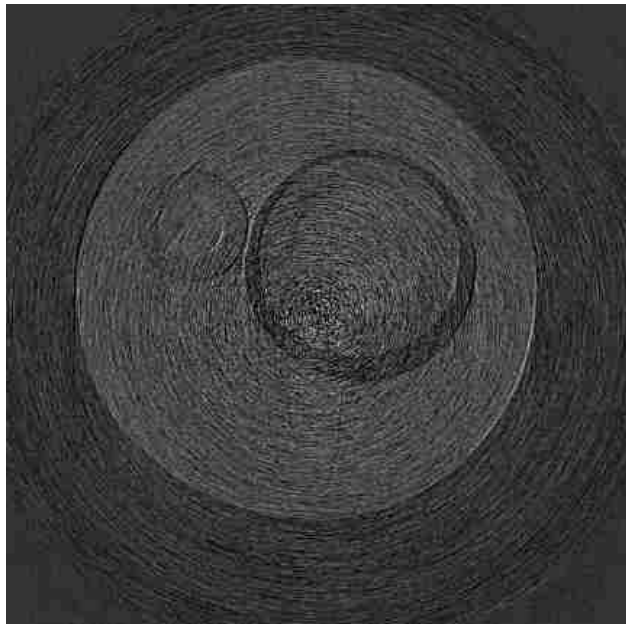


Figure 50: Example of a KES image of CHO cells assuming the mass attenuation coefficients of water as the buffering solution.

4.5 Discussion

4.5.1 Cell Density Assay

From previous calculations, the expected iodine concentration in a breast cancer is 0.06 mg ml^{-1} . The results of the hemocytometry measurement showed that the number of cells per unit volume within the cell pellet was 50 times lower than that of breast cancer. To image the CHO cells at this density, an iodine concentration of 0.001 mg ml^{-1} would need to be distinguishable from water. Centrifuging the cells at a higher rpm should

improve cell density. However, hemocytometry may not be effective for measuring higher cell mass densities.

4.5.2 IUdR Uptake Assay

The radioisotope assay was successfully able to verify the IUdR uptake by the CHO cells using DNA isolation with the results agreeing with the literature. This approach was effective but required facilities equipped to handle both biological and radiological hazards. This approach uses radioactive materials, which provide an additional methodology complication, as well as potentially being difficult to quantify in vivo with the desired resolution. MicroCT has more than enough resolution, doesn't have the radioactivity hazard, and CT will need to be done anyways for radiation therapy treatment planning.

4.5.3 IUdR Replacement Measurements

The HU and KES measurements found that cells grown in 20 μM IUdR were distinguishable from water and from cells grown in the absence of IUdR. However, these calculated iodine concentrations were substantially higher than expected for both HU and KES. The iodine concentrations determined by both methods correspond to an unrealistically large IUdR replacement. A possible explanation for the large iodine concentration is that there is unincorporated unmetabolized IUdR located within the cells. This means that the CT-based measurements are reporting the amount of iodine contained within the entire cell, rather than just the uptake in the DNA. If the total amount of IUdR in the cell (which we can measure) is still proportional to the amount of IUdR in the DNA (and we can learn the proportionality), then CT could conceivably still be used to quantify the IUdR.

Chapter 5. Conclusions and Recommendations

The hypothesis of this thesis was that using the current image acquisition and processing setup for these systems, an iodine concentration of 0.06 mg ml^{-1} can be measured from the CT image data with a contrast to noise ratio of 3.

5.1 Summary of Results

The resolution of the two imaging systems was compared by measuring the MTF of each and expressing the response at 10% of the maximum MTF. At 56 lp mm^{-1} , the CAMD tomography system offers superior imaging resolution over the Skyscan-1074, with 5.5 lp mm^{-1} by a factor of 10 to 1. Results from a measurement of the scatter contribution in the CAMD system yielded a SPR of 2.5%. This contribution was deemed not significant and the implementation of a scatter correction routine was not considered necessary.

The minimum detectable iodine concentration for the Skyscan-1074 was 0.1 mg ml^{-1} at 40 kVp with a CNR of 3.58. For the CAMD system, images acquired above the iodine K-edge of 33.169 keV at a monochromator setting of 33.5 keV were able to measure iodine concentrations as low as 0.1 mg ml^{-1} with a CNR of 3.86 with the potential to image the target concentration of 0.06 mg ml^{-1} . However, CAMD images acquired below the iodine K-edge at a monochromator setting of 32.5 keV could only measure iodine concentrations as low as 1.0 mg ml^{-1} at a CNR of 3.97. Results from KES analysis showed that CAMD could only measure 0.25 mg ml^{-1} of iodine at a CNR of 3.11.

IUdR replacement of thymidine was 17.4% for cells grown in $20 \text{ }\mu\text{M}$ IUdR medium. By applying the HU calibration curves to the CAMD results, measurements of

the iodine concentration at a monochromator setting of 32.5 keV showed that cells with IUdR were indistinguishable from cells without IUdR. For the images made at a monochromator setting of 33.5 keV, the average difference between cells with and without IUdR was 20.2 ± 4.4 HU, which equates to a measured iodine concentration of 0.21 ± 0.04 mg ml⁻¹. The KES results found the iodine concentration to be 0.20 ± 0.01 mg ml⁻¹ for cells with IUdR.

5.2 Conclusions

These studies were unable to prove that the Skyscan-1074 microCT system or CAMD micro-tomography beamline could be used to distinguish the desired iodine concentration of 0.06 mg ml⁻¹ with a CNR of 3 using these methods. While it may not be possible to increase the contrast in the CT images, it may be possible to decrease the relative noise by sacrificing spatial resolution (i.e. bigger pixels). Because the CAMD tomography system offers significantly improved resolution over the Skyscan-1074 microCT system, it may be able to achieve a much lower limit of detection by pixel resizing prior to reconstruction. Due to long acquisition times and high radiation surface doses along with the inability to image the target concentration, CAMD imaging with the current acquisition setup is not appropriate for in vivo small animal studies. With comparable sensitivity, significantly shorter acquisition times, and a larger field of view, the Skyscan-1074 microCT system appears to be a more practical choice for future in vivo small animal studies. However, the poor fit to the data indicates a systematic bias which needs to be investigated further.

Both the Skyscan-1074 system and the CAMD system were capable of imaging iodine concentrations as low as 0.1 mg ml⁻¹ at a CNR of 3 based on a HU calibration

curve. KES was not as sensitive as images acquired above the iodine K-edge which was likely due to a higher sensitivity to noise produced as a result of the subtraction which may be improved by using larger pixels.

The IUdR replacement, as verified by radioiodine assay, was consistent with the literature. However, the cell pellet's low cell density should have produced an expected iodine concentration of 0.001 mg ml^{-1} , below CAMD's lower limit of detection. Results based on both HU calculations and KES were successfully able to differentiate cells with IUdR from cells without IUdR and from water. This indicates that there is substantial residual unmetabolized IUdR remaining unincorporated in the cells' DNA. If it is possible to relate the amount of unincorporated IUdR in the cell to the amount in the DNA it may be possible to use CT to image the iodine distribution for treatment planning.

5.3 Recommendations for Future Studies

The Skyscan and CAMD systems may still be useful in developing an x-ray activated Auger electron radiotherapy treatment planning system provided the lower limit of detection can be improved. One possible method which may accomplish this is to use larger pixels during image reconstruction. This should reduce the relative noise per pixel and thereby increase the contrast to noise ratio.

One future study might investigate the amount of unincorporated IUdR in the cells. It may be possible to relate the amount of unincorporated IUdR in the cells to the amount of IUdR in the DNA. One method which could measure this is with a radioiodine assay, first measuring the intact cells and then measuring the DNA alone. The difference in the two measurements would be the amount of unbound IUdR in the cells.

References

- ¹J. H. Hall, and A. J. Giaccia, *Radiobiology for the Radiologist* (Lippincot Williams & Wilkins, Philadelphia, 2005)
- ²A. I. Kassis, "The Amazing World of Auger Electrons," *Int J Radiat Oncol Biol Phys.* **80**, 789-96 (2004).
- ³A. Cole, "Absorption of 20-eV to 50,000-eV electron beams in air and plastic" *Rad Res.* **38**, 7-33 (1969).
- ⁴J. A. O'Donoghue, and T. E. Wheldon, "Targeted radiotherapy using Auger electron emitters," *Phys Med Biol.* **41**, 1973-92 (1996).
- ⁵B. H. Laster, W. C. Thomlinson, and R. G. Fairchild, "Photon Activation of Iododeoxyuridine: Biological Efficacy of Auger Electrons," *Rad Res.* **133**, 219-44 (1993).
- ⁶S. J. Karnas, E. Yu, R. C. McGarry, and J. J. Battista, "Optimal photon energies for IUdR K-edge radiosensitization with filtered x-ray and radioisotope sources," *Phys Med Biol.* **44**, 2537-49 (1999).
- ⁷J. A. Cook, J. Glass, R. Lebovics, H. Bobo, H. Pass, T. F. DeLaney, E. H. Oldfield, J. B. Mitchell, E. Glatstein, and T. E. Goffman, "Measurement of Thymidine Replacement in Patients with High Grade Gliomas, Head and Neck Tumors, and High grade Sarcoms after Continuous Intravenous Infusion of 5-Iododeoxyuridine," *Cancer Res.* **52**, 719-25 (1992).
- ⁸T. J. Kinsella, K. A. Kunugi, K. A. Vielhuber, W. McCulloch, S. Liu, and Y. Cheng, "An in Vivo Comparison of Oral 5-Iodo-2'-deoxyuridine and 5-Iodo-2-pyrimidinone-2'-deoxyribose Toxicity, Pharmacokinetics, and DNA Incorporation in Athymic Mouse Tissues and the Human Colon Cancer Xenograft, HCT-116," *Cancer Res.* **54**, 2695-2700 (1994).
- ⁹F. Carroll, "Tunable, Monochromatic X-Rays: An Enabling Technology for Molecular/Cellular Imaging and Therapy" *J Cell Biochem.* **90**, 502-8 (2003).
- ¹⁰P. Baldelli, A. Taibi, A. Tuffanelli, M. C. Gilardoni, and M. Gambaccini, "A prototype of a quasi-monochromatic system for mammography applications," *Phys Med Biol.* **50**, 2225-40 (2005).
- ¹¹F. E. Carroll, "Tunable Monochromatic X Rays: A New Paradigm in Medicine," *AJR.* **179**, 583-90 (2002).
- ¹²F. A. Dilmanian, 1992. "Computed Tomography With Monochromatic X-rays." *Am J Physiol Imaging* **3**: 175-193.

- ¹³F. E. Carroll, "Pulsed, Tunable Monochromatic X-ray Beams from a Compact Source: New Opportunities," *AJR*. **181**, 1-6 (2003).
- ¹⁴B. Girolami, B. Larsson, M. Preger, C. Schaerf, and J. Stepanek, "Photon Beam for Radiosurgery Produced by Laser Compton Backscattering from Relativistic Electrons," *Phys Med Biol*. **41**, 1581-96 (1996).
- ¹⁵J. T. Bushberg, J. A. Seibert, E. M. Leidholdt, and J. M. Boone, "The Essential Physics of Medical Imaging Second Edition" Lippincot Williams & Wilkins, 327-72 (2002).
- ¹⁶F. M. Khan, *The Physics of Radiation Therapy: Third Edition* (Lippincot Williams & Wilkins, Philadelphia, 2003)
- ¹⁷J.H. Hubbell, and S. M. Seltzer, "Tables of X-Ray Mass Attenuation Coefficients and Mass Energy-Absorption Coefficients from 1 keV to 20 MeV for Elements Z = 1 to 92 and 48 Additional Substances of Dosimetric Interest," (1996)
<http://physics.nist.gov/PhysRefData/XrayMassCoef/cover.html>
- ¹⁸A. E. Alvarez, and A. Macovski, "Energy-selective Reconstructions in X-ray Computerized Tomography," *Phys MedBiol*. **21**, 733-44 (1976).
- ¹⁹P. M. Shikhaliev, "Detector Technologies for Photon Counting/energy Resolving X-Ray and CT Imaging," *Med Phys* **34**, 2554-5 (2007).
- ²⁰R. A. Kruger, S. J. Riederer, and C. A. Mistretta, "Relative properties of tomography, K-edge imaging, and K-edge tomography," *Med Phys*. **4**, 244-9 (1977).
- ²¹H. Elleaume, A. M. Charvet, S. Corde, F. Esteve, and J. F. Le Bas, "Performance of computed tomography for contrast agent concentration measurements with monochromatic x-ray beams: comparison of K-edge versus temporal subtraction," *Phys Med Biol*. **47**, 3369-85 (2002).
- ²²S. Oelckers, and W.Graeff, "In situ measurement of iron overload in liver tissue by dual-energy methods," *Phys Med Biol*. **41**, 1149-65 (1996).
- ²³H. Suhonen, L. Porra, S. Bayat, A. R. A. Sovijarvi, and P. Sourtti, "Simultaneous *in vivo* synchrotron radiation computed tomography of regional ventilation and blood volume in rabbit lung using combined K-edge and temporal subtraction," *Phys Med Biol*. **53**, 775-91 (2008).
- ²⁴P. Baldelli, A. Bravin, C. Di Maggio, G. Gennaro, A. Sarnelli, A. Taibi, and M. Gambaccini, "Evaluation of the minimum iodine concentration for contrast-enhanced subtraction mammography," *Phys Med Biol*. **51**, 4233-51 (2006).
- ²⁵M. Retsky PhD, *Cancer Growth: Implications for Medicine & Malpractice*.
<http://www.karlloren.com/biopsy/p57.htm>. 1998.

- ²⁶J. G. Tjuvajev, H. A. Macapinlac, F. Daghighian, A. M. Scott, J. Z. Ginos, R. D. Finn, P. Kothari, R. Desai, J. Zhang, B. Beattie, M. Graham, S. M. Larson and R. G. Blasberg, "Imaging of Brain Tumor Proliferative Activity with Iodine-131-Iododeoxyuridine," *J Nucl Med.* **35**, 1407-17 (1994).
- ²⁷G. Mariani, S. Di Sacco, D. Volterrani, L. Di Luca, S. Buralli, R. Di Stefano, J. Baranowska-Kortylewicz, D. Bonora, F. Matteucci, S. Ricci, C. R. Bellina, A. Falcone, P. A. Salvadori, F. Mosca, S. J. Adelstein, and A. I. Kassis, 1996. "Tumor targeting by intra-arterial infusion of 5-[123I]iodo-2'-deoxyuridine in patients with liver metastases from colorectal cancer," *J Nucl Med.* **37**, 22-25 (1996).
- ²⁸R. G. Blasberg, U. Roelcke, R. Weinreich, B. Beattie, K. von Ammon, Y. Yonekawa, H. Landolt, I. Guenther, N. E. Crompton, P. Vontobel, J. Missimer, R. P. Maguire, J. Kozirowski, E. J. Knust, R. D. Finn RD, and K. L. Leenders, "Imaging brain tumor proliferative activity with [124I]iododeoxyuridine," *Cancer Res.* **60**, 642-35 (2000).
- ²⁹F. A. Dilmanian, X.Y. Wu, J. Kress, B. Ren, D. Chapman, J. A. Coderre, D. Greenberg, E. Parsons, M. Shleifer, D. N. Slatkin, W. C. Thomlinson, Z. Zhong, T. M. Button, F. Giron, J. Liang, M. J. Petersen, C. T. Roque, M.H. Miller, H. Weedon, D.J. Krus, L. Perna, Bicon, and K. Yamamoto, "Dual Energy Iodine Contrast CT with Monochromatic X Rays." *Proceedings of the IEEE Nuclear Science Symposium and Medical Imaging Conference*, 1995, **3**: 1392-6.
- ³⁰J. Singer, "Computational formulas for confidence intervals and prediction intervals in simple linear regression."
http://isites.harvard.edu/fs/docs/icb.topic244690.files/Supplemental_resources_for_Unit_3/Computational_formulas_for_confidence_and_prediction_intervals.pdf
- ³¹ASTM E 1695-95. Standard Test Method for Measurement of Computed Tomography (CT) System Performance.
- ³²S. Oves, K. R. Hogstrom, K. Ham, E. Sajo, and J. P. Dugas, "Dosimetry intercomparison using a 35-keV X-ray synchrotron beam," *Eur J Radiol.* in press (2008)
- ³³J. P. Dugas, S. D. Oves, E. Sajo, K. L. Matthews, K. Ham, and K. R. Hogstrom, "Monochromatic beam characterization for Auger electron dosimetry and radiotherapy," *Eur J Radiol.* in press (2008)
- ³⁴M. Endo, S. Mori, T. Tsunoo, and H. Miyazaki, "Magnitude and effects of x-ray scatter in a 256-slice CT scanner," *Med Phys.* **33**, 3359-68 (2006).
- ³⁵T. T. Puck, S. J. Cieciora, and A. Robinson, "Genetics of somatic mammalian cells. III. Long-term cultivation of euploid cells from human and animal subjects" *J Exp Med.* **108**, 945-56 (1958).

³⁶S. T. Thornton, and A. Rex, *Modern Physics for Scientists and Engineers, Second Edition* (Saunders College Publishing, Philadelphia, 2002)

³⁷The NIST Reference on Constants, Units, and Uncertainty,
<http://physics.nist.gov/cuu/index.html>

Appendix A. K-edge Subtraction

A.1 K-edge Subtraction Theory

The principles involved of CT imaging can be further exploited by making use of the discontinuity of the attenuation curve across the K-edge. In K-edge subtraction imaging, which is well suited to monochromatic x-rays, two images are acquired of the same subject at two energies bracketing the K-edge of one of the elements. This technique can be used to directly quantify concentrations of a specific material by enhancing the signal produced by the desired material and effectively canceling the signal produced by other materials. For solutions containing iodine and water, the set of linear equations produced are as follows:

$$\mu[E_1] = \left(\frac{\mu_I}{\rho_I} \right)_1 \rho_{I_c} + \left(\frac{\mu_W}{\rho_W} \right)_1 \rho_{W_c} \quad (\text{A-1})$$

$$\mu[E_2] = \left(\frac{\mu_I}{\rho_I} \right)_2 \rho_{I_c} + \left(\frac{\mu_W}{\rho_W} \right)_2 \rho_{W_c} \quad (\text{A-2})$$

Here, $\mu[E_i]$ is the measured value at energy E_i and $\left(\frac{\mu_n}{\rho_n} \right)_i$ are the mass attenuation coefficients for the given material at that energy. The value ρ_{n_c} is the product of the density of the n^{th} material and the weight fraction and is energy independent. This is the concentration of the desired material and can be expressed as the set of linear equations in equation (A-3).

The matrix of attenuation coefficients forms the matrix A with determinant $|A|$. The concentration can be found by solving the above equation to obtain equation (A-4).

$$\begin{bmatrix} \mu[E_1] \\ \mu[E_2] \end{bmatrix} = \begin{bmatrix} \left(\frac{\mu_I}{\rho_I}\right)_1 & \left(\frac{\mu_W}{\rho_W}\right)_1 \\ \left(\frac{\mu_I}{\rho_I}\right)_2 & \left(\frac{\mu_W}{\rho_W}\right)_2 \end{bmatrix} \begin{bmatrix} \rho_{Ic} \\ \rho_{Wc} \end{bmatrix} \quad (\text{A-3})$$

$$\begin{bmatrix} \rho_{Ic} \\ \rho_{Wc} \end{bmatrix} = \frac{1}{|A|} \begin{bmatrix} \left(\frac{\mu_W}{\rho_W}\right)_2 & -\left(\frac{\mu_W}{\rho_W}\right)_1 \\ -\left(\frac{\mu_I}{\rho_I}\right)_2 & \left(\frac{\mu_I}{\rho_I}\right)_1 \end{bmatrix} \begin{bmatrix} \mu[E_1] \\ \mu[E_2] \end{bmatrix} \quad (\text{A-4})$$

From this, the iodine concentration can be found by the following:

$$\rho_{Ic} = \frac{\mu[E_2] \cdot \left(\frac{\mu_W}{\rho_W}\right)_1 - \mu[E_1] \cdot \left(\frac{\mu_W}{\rho_W}\right)_2}{\left(\frac{\mu_W}{\rho_W}\right)_2 \cdot \left(\frac{\mu_I}{\rho_I}\right)_1 - \left(\frac{\mu_W}{\rho_W}\right)_1 \cdot \left(\frac{\mu_I}{\rho_I}\right)_2} \quad (\text{A-5})$$

Appendix B. CAMD Tomography Beamline Energy Measurement

B.1 X-ray Powder Diffraction Theory

The measurement of the beam energy was performed using X-ray powder diffraction. In this technique, X-rays traversing a solid crystalline lattice scatter off bound atoms (Figure 51). The scattered electromagnetic waves constructively interfere due to lattice planes (also called Bragg planes) inherent in the crystal (Figure 52). For a solid crystal, the observable interference pattern effects are that of bright spots (also called Laue dots) in a plane normal to the beam path. The position and intensities of the dots vary with the orientation of the crystal to the beam path. Because the bound atoms in the crystal lattice act as a 3D diffraction grating, the angular deflection of the bright spots relative to the incident beam can be calculated. This is accomplished using Bragg's law (equation B-1).

$$n \lambda = 2 d \sin \theta \quad (\text{B-1})$$

Bragg's law is satisfied for a given interlattice spacing (d) and angular diffraction (θ) when the difference in path length (λ) is an integer number of wavelengths. The incident beam energy can also be determined, by extension, from the wavelength ($E = h \frac{c}{\lambda}$). The interlattice spacings for a cubic crystal (d) are derived from the lattice parameter (D). The lattice spacing for any given Bragg plane can be determined by dividing D by RSS of the Miller indices³⁶.

Using a powdered sample in place of a solid crystal creates an isotropic distribution of interlattice spacings. Instead of single rays, this produces concentric cones known as Debye-Scherrer cones. A reliable method to measure the Debye-Scherrer

patterns is to use film oriented normal to the beam path.³² The Debye-Scherrer effect at the film plane is concentric rings. The ring radius (r_i) was related to the angular deviation (2θ) of the diffracted X-rays relative to the beam path using the following relationship.

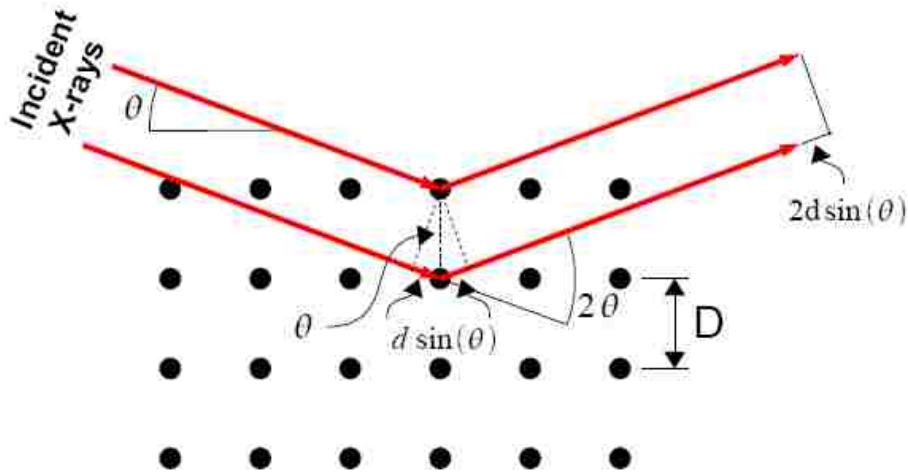


Figure 51: X-ray scatter diagram from Bragg lattice planes (adapted from Thornton et al 2002).³⁶ The X-ray scatter angle is twice the incident angle (2θ). D is the lattice parameter and d is the interlattice spacing. The difference in path length is $2d \sin(\theta)$.

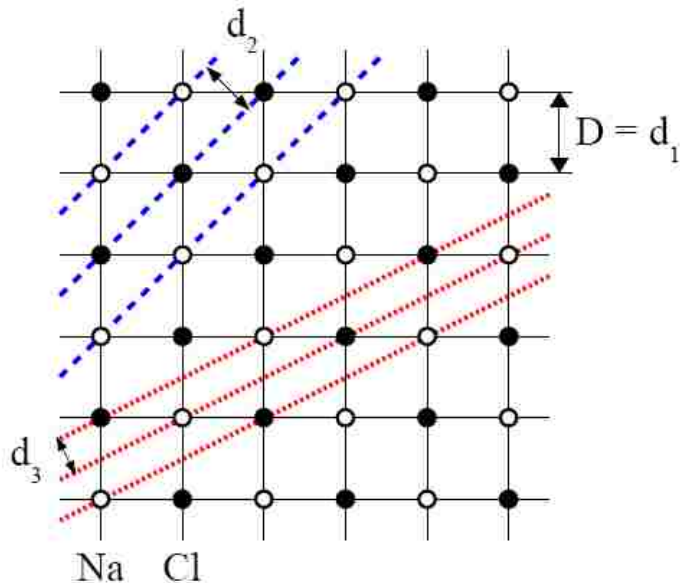


Figure 52: A top view example of three possible Bragg planes in a NaCl crystal and their corresponding interlattice spacings (adapted from Thornton et al 2002).³⁶

In these studies the powder sample used was silicon with a space group 640c (Si640c). The 640c space group designation corresponds to the lattice properties which happen to be well known. In this case, the lattice parameter ($a = 543.102064 \times 10^{-12} \text{ m}$) was obtained through NIST.³⁷

Table 8: For Si640c, the three brightest Debye-Scherrer cones correspond to the first three lattice spacings d . The lattice spacing is determined by dividing the lattice parameter a by the RSS of the Miller indices; H , K , and L .³⁷

Cone #	H	K	L	d_i
1	1	1	1	$313.501 \times 10^{-12} \text{ m}$
2	2	2	0	$191.979 \times 10^{-12} \text{ m}$
3	3	1	1	$163.720 \times 10^{-12} \text{ m}$

To contain the Si640c powder during irradiation, a 3 mm thick PMMA slab was used to hold the sample. A 45° conic hole, shown in Figure 53, was milled into one end of the sample holder to provide containment for the powder sample (labeled A). Scotch® brand tape was applied to both sides of the sample holder to immobilize the powder. An identical hole (labeled B) was milled into the opposite end of the sample holder.

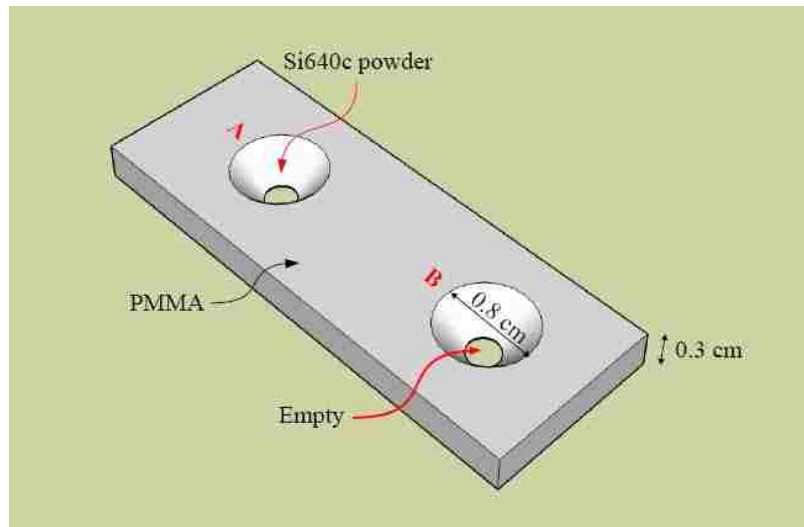


Figure 53: Diagram of the Si640c powder sample. The sample holder was constructed from PMMA. The Si640c powder (A) was contained by Scotch® tape on both sides. The empty hole (B) was used to obtain correct vertical alignment of the sample holder.

Support for the sample holder was provided by an adjustable stage (Figure 54). The sample holder was aligned such that the small cone entrance faced upstream relative to the X-ray beam. Tungsten blocks were used to collimate the beam to a $2\text{ mm} \times 2\text{ mm}$ cross-sectional area. To ensure that Si640c conic powder sample was coaxial with respect to the collimated beam, the empty hole was used along with $5\text{ cm} \times 5\text{ cm}$ sheets of Gafchromic EBT® (International Specialty Products, Wayne, NJ, USA) radiochromic film to obtain the correct vertical alignment. The process entailed taping the Gafchromic film to the large conic entrance of the empty hole in the sample holder and exposing the film. The film was exposed for an unregulated length of time. The vertical deviation of the beam to the empty conic center was measured followed by necessary adjustment of the stage height.

Approximately 10 cm downstream from the powder sample, a single sheet of radiographic EDR2 film was placed (Figure 54). The film was fixed to a 7.90 cm thick Styrofoam block. The Styrofoam block was selected because it provided physical support for the film, minimal backscatter, and was readily available. The film block combination was oriented normal to the beam path for exposure. An additional three films were exposed individually at increasing distances of 7.90 cm increments by adding additional Styrofoam blocks as needed. The film located 10 cm from the powder sample was exposed for approximately 25 minutes. Each film after the first was exposed an additional 5 minutes for increment of 7.90 cm.

The distance from the powder sample to the first film plane was not precisely known. This was primarily due to the finite thickness of the powder sample. The result of the distance uncertainty made measurements of the diffraction angle unreliable. The

diameter of the Debye-Scherrer rings at each film plane increased linearly with the distance from the powder sample (Figure 55). By exposing multiple films at known distances relative to the other films, the precise distance to the sample was unnecessary.

The films were developed using a KODAK X-Omat Processor located at Mary Bird Perkins Cancer Center. The films were digitized using an EPSON Expression 1680 flatbed scanner using EPSON Scan® software. The images were scanned as positive film transparencies using 16 bit grayscale pixel depth with 300 dpi. The images were saved as TIF files.

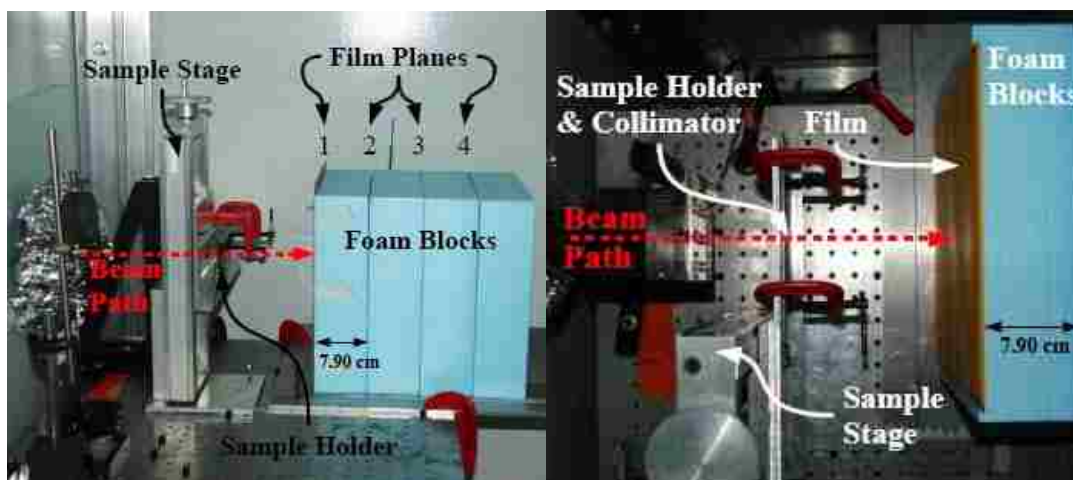


Figure 54: The side view (left) and top view (right) of the X-ray powder diffraction experimental apparatus are shown.

Image analysis was performed using ImageJ (NIH, Bethesda, MD). The images were first processed using a bandpass filter in Fourier space. Structures smaller than three pixels and larger than 40 pixels were removed by this filter. Each ring diameter was determined by first constructing a chord joining the two end points located on the ring and plotting the profile of the chord bisector extended a sufficient distance beyond the ring. A vector containing the distance relative to the bisector's origin and intensity for

each pixel was obtained. The ring diameter was then determined to be the distance between peak values in the ring profile.

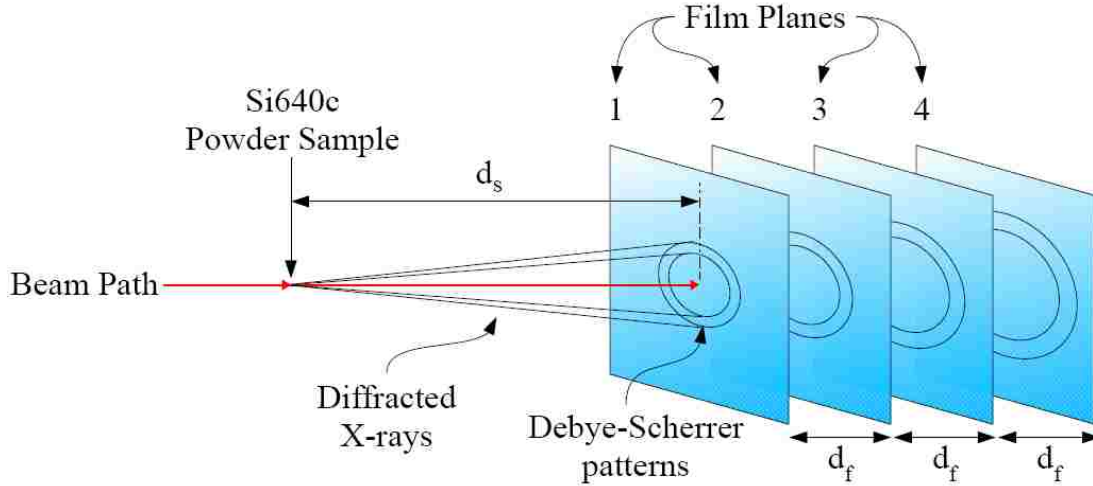


Figure 55: Diagram illustrating the effects of X-ray powder diffraction. The resulting Debye-Scherrer patterns are shown at several film planes.

The ring diameters for each ring were plotted as a function of relative film distance. The slope obtained from a linear fit of the radius for each ring pattern is congruent to the slope (m) of any line which falls on the corresponding Debye-Scherrer cone face. From this slope, the diffraction angle can be obtained from the following equation:

$$m_{fit} = \tan(2\theta) \quad (\text{B-2})$$

Combining the above with the relationship between energy and wavelength ($E = h \frac{c}{\lambda}$), the energy can be found using the following:

$$E = \frac{hc}{2d \sin\left(\frac{1}{2} \tan^{-1}(m_{fit})\right)} \quad (\text{B-3})$$

B.2 X-ray Powder Diffraction Energy Measurements

An example of a film exposed during an X-ray powder diffraction measurement is displayed in Figure 56. The image on the left is an image showing the concentric rings surrounding the collimated beam. The image on the right shows the same image after applying a bandpass filter.

Results from the x-ray powder diffraction measurements are compiled in Table 9 and displayed in Figure 57. The average difference in energy between the X-ray powder diffraction measurements and the monochromator setting was 0.1 keV. The RSS of the difference in energy was 0.44 keV.

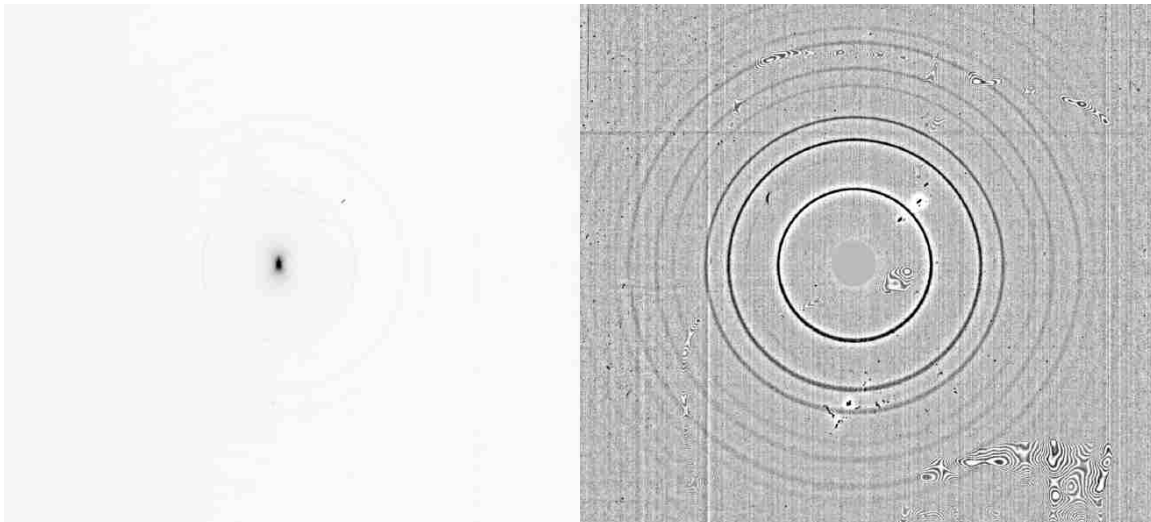


Figure 56: On the left is an example of a film shot from X-ray powder diffraction measurements. The concentric diffraction rings can be seen around the collimated beam. On the right is the same film after being passed through a band pass filter. The collimated beam has been obscured for display.

Table 9: Monochromator setting and results from the X-ray powder diffraction measurements with the measurement error.

Measurement Date	Monochromator Setting [keV]	X-ray Powder Diffraction [keV]	Error [keV]
Sept 20 2008	30	30.081	0.051
Sept 21 2009	35	35.124	0.055
Jan 21 2008	33.8	33.976	0.057
Jan 22 2008	32.5	32.791	0.053
Mar 18 2008	33.5	33.391	0.055
Mar 19 2008	32.5	32.623	0.052
May 08 2008	33.5	33.59	0.055
May 09 2008	32.5	32.59	0.052
May 15 2008	33.5	33.621	0.056
May 16 2008	32.5	32.482	0.052
Average difference in energy [keV] =			0.10

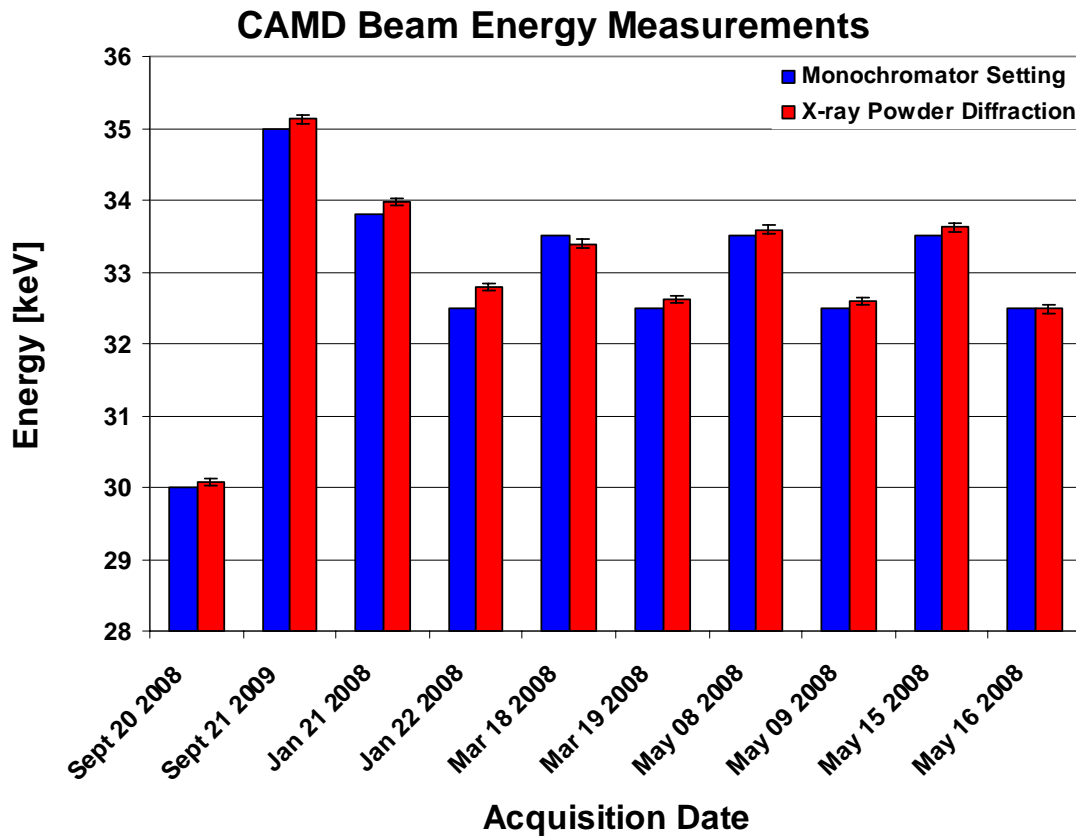


Figure 57: Comparison of CAMD Tomography beamline monochromator settings versus X-ray powder diffraction measurements.

Vita

Christopher was born in Albuquerque, New Mexico, to George and Cynthia Welch. He graduated high school in 1997 from Santa Fe High School. After a four year hiatus, he enrolled in Louisiana State University to pursue a bachelor's degree in physics. After graduating in 2005, he married Christina Fannin and enrolled in graduate school at Louisiana State University to pursue a master's degree in medical physics.